The coupling between mutations effects and environment guides the exploration of phenotypic space as evidenced in artificial selection experiments

Arnaud Desbiez-Piat[1,2], Adrienne Ressayre[1], Elodie Marchadier[1], Alicia Noly[3], Aurélie Bourgais[1], Nathalie Galic[1], Martine Le Guilloux[1], Maud I. Tenaillon[1,†,*] and Christine Dillmann[1,†,*]

[1]Université Paris-Saclay, INRAE, CNRS, AgroParisTech, GQE - Le Moulon, France
[2]Université Montpellier, INRAE, Institut Agro Montpellier, LEPSE, France
[3]Université Paris-Saclay, CNRS, INRAE, Université Evry, Institute of Plant Sciences Paris-Saclay
[†]These authors contributed equally to this work.

*Corresponding authors: Maud.Tenaillon[at]inrae.fr and Christine.Dillmann[at]inrae.fr, Université Paris-Saclay, INRAE, CNRS, AgroParisTech, GQE - Le Moulon, 91190, Gif-sur-Yvette, France

Abstract

Empirical description of phenotypic shifts in selection experiments have nourished quantitative genetics models. These models have shown that long-term selection responses depend both on the initial standing variance as well as the flux of incoming mutations, and that quantifying the proportion of genetic variance due to latter is essential to understanding the seeming absence of selection limits. There are however at least two important things to keep in mind when interpreting selection experiments: first correlative responses to selection on non-focal traits can perturb the selection response on the focal trait and second, generations and selection environments are confounded so that genotype by environment interactions are ignored. Here we used the Saclay Divergent Selection Experiments (DSE) on maize flowering time that display striking selection responses over 22 generations and combined yearly measurements of flowering time (DSEYM), measurements of 11 traits on a subset of 308 DSE genotypes measured for two consecutive years in common gardens (DSECG), as well as genotyping data to track the fate of individual mutations in pedigrees, with four main objectives: (1) to quantify the relative contribution of standing variation and *de novo* mutational variance to the selection response; (2) to approximate the distribution of phenotypic effects of *de novo* mutations; (3) to study the impact of GxE interactions in the observed selection response; (4) to describe how trait correlations modulate the exploration of the phenotypic space. In agreement with theoretical predictions, we experimentally validated two successive phases in the selection response: one governed by the fixation of standing variants whose contribution quickly reached a plateau, and the second governed by the fixation of *de novo* mutations sustaining the selection response. The distribution of selected phenotypic effects confirmed the expected enrichment of fixation of beneficial mutations with an average effect of $+0.278$ and $+0.299$ days to flowering, depending on the genetic background; but also revealed fixation of unfavorable mutations reaching up to 25% of incoming mutations. Accumulation of genetic load may be due to antagonistic pleiotropy whereby mutations that were fixed in the selection environment (DSEYM) turn to be unfavorable in evaluation environment (DSECG). Finally, we found that global patterns of correlations between-traits are conserved across genetic backgrounds but exhibit a temporal pattern. Traits that are weakly or uncorrelated with flowering time allow stochastic exploration of the phenotypic space, owing to the microenvironment-specific fixation of standing variants and a pleiotropic mutational input.

Keywords: Experimental evolution, Distribution of mutational effects, Environmental effect, Phenotypic space, Adaptive dynamics

Empirical description of phenotypic shifts have nourished quantitative genetics models aiming at deciphering the underlying evolutionary processes (Hill and Caballero 1992; Walsh and Lynch 2018). The persistence through time of heritable variation (Odhiambo and Compton 1987; Moose *et al.* 2004; Weber and Diggins 1990; Caballero *et al.* 1991; Mackay 2010; Lillie *et al.* 2019; Wisser *et al.* 2019) fit well with Fisher's infinitesimal model (Fisher Ronald Aylmer 1930) and the derivatives of the breeder equation (Lush 1943; Lande 1979; Lande and Arnold 1983). These models indeed predict a continuous and linear response with no finite limits, especially under truncation selection known to be the most effective form of directional selection (Crow and Kimura 1979). However, under the alternative assumption of finite genetic architecture the long-term selection response is expected to plateau, reached all the sooner as selection-induced linkage disequilibrium diminishes the standing genetic diversity, the so-called Bulmer Effect (Bulmer 1971; Hospital and Chevalet 1996). The plateau value, that is the expected maximum shift, depends on both, the initial standing variance and the effective population size (Robertson 1960; Roberts 1966; Falconer 1971). The latter determines the flux of incoming *de novo* mutations. Interestingly, when this flux is large enough, the long-term response to selection can be infinite even with finite genetic architectures (Hill 1982a,b; Lynch and Hill 1986; Weber and Diggins 1990; Wei *et al.* 1996; Walsh and Lynch 2018). Hence quantifying the proportion of genetic variance due to the

input of new mutations (V_m), the so-called mutational variance, is central to understand the seeming absence of selection limits (Turelli 1984).

Mutational variance is determined by the mutation rate per locus as well as the architecture of the trait — *i.e.* the size of the mutational target and the distribution of fitness effects (DFE) of incoming mutations (Bürger 1993; Bürger and Lande 1994). One popular strategy to approach the incoming mutational variance is to rely on divergent selection experiments (DSEs) to estimate the mutational heritability. Hence, starting from a genetically-homogeneous material such as inbred strains, the mutational heritability can be estimated from DSEs, as the slope of the selection response across generations. The mutational heritability denotes the ratio of the mutational variance over the residual variance, $\frac{V_m}{V_E}$ (Hill 1982b; Houle *et al.* 1996; Keightley 2010). Previously estimated values fell within the range 4.10^{-4} to 3.10^{-2} (Houle *et al.* 1996; Keightley 2010). However, because DSEs offer control over the pedigree of individuals, a classical animal model (Kruuk 2004) can also be applied to decompose phenotypic variance and directly estimate mutational variance considered as a random effect. An interesting aspect of the animal model is to account for the effects of newly occurring mutations as they increase similarity among individuals and therefore modify the additive genetic variance-covariance matrix (Wray 1990) (used to compute the Best Linear Unbiased Predictor of Mutational effects, subsequently called BLUPM). This is particularly true in populations characterized by a small effective population size, where the effect of increased similarity is magnified.

There are however limits to the use of selection experiments. The first limitation is that time-series (generations of selection) introduce confounding effects between generational environments and genetic changes because of ubiquitous genotype-by-environment (GxE) interactions (Li *et al.* 2017), *i.e.* the genetic variability in plastic responses. Replicated common garden experiments can however provide effective settings to disentangle these two effects. They have been successfully employed to test for local adaptation for life-history traits, phenology and allometric relationships (reviewed in de Villemereuil *et al.* (2016)). The second limitation is that the trait under selection does not evolve independently from other traits, and correlative responses to selection at other traits may perturb selection responses. Such correlative responses may result from linkage disequilibrium between quantitative trait loci (QTL) evolving under drift/selection. They may also result from correlated physiological functions where a first trait governs a second one, e.g., flowering time in maize is partly determined by floral transition time. Finally, genetic correlations may result from true pleiotropy when a single QTL affects several traits (Chen and Lübberstedt 2010; Reinert 2022).

The evolution of a population in the multivariate phenotypic space is governed, in the short-term, by the extension of the breeder's equation $\boldsymbol{\Delta\bar{z}} = \boldsymbol{GP^{-1}s}$ (Lande 1979; Lande and Arnold 1983) linking the vector of mean response $\boldsymbol{\Delta\bar{z}}$ to the $\boldsymbol{G}$-matrix. The $\boldsymbol{G}$-matrix describes the standing additive genetic variances and covariances for a suite of traits, $\boldsymbol{s}$ being the vector of selection differentials and $\boldsymbol{P}$ being the observe phenotypic matrix of measured traits. However, in the long-term, the effects of new mutations on genetic variances and covariances –represented through the $\boldsymbol{M}$-matrix–, define the evolvability of the population (*e.g.* see Houle *et al.* (2017)). In the context of an adaptive walk towards a fitness optimum, Fisher's geometric model (Tenaillon 2014) predicts that the size of adaptive mutations tends to decrease with the number of influenced traits. Consequently the expected DFE is exponential in the case of an infinite number of correlated traits influencing fitness, and follows a beta distribution when the number of correlated traits is small to moderate (Martin and Lenormand 2008). Correlative response to stabilizing selection arises because of an interplay of pleiotropic effects of mutations and correlational selection, favoring certain combinations of trait values. This interplay is however modulated by the intensity of genetic drift: in infinite populations, genetic correlations are unaffected by the strength of selection while in small populations the strength of selection does affect genetic correlations (Chantepie and Chevin 2020; Doroszuk *et al.* 2008).

Here we used the Saclay DSEs on maize flowering time that display striking selection responses over 22 generations - despite a dearth of initially standing variation and a high drift-high selection regime (Durand *et al.* 2010, 2012, 2015; Desbiez-Piat *et al.* 2021) - with four main objectives: (1) to quantify the relative contribution of standing variation and *de novo* mutational variance to the selection response using the BLUPM model (Wray 1990); (2) to approximate the DFE of *de novo* mutations; 3) to study the impact of GxE interactions in the observed selection response; (4) to describe correlations between traits and how they modulate the exploration of the phenotypic space. To fulfill these objectives, we combined yearly measurements of flowering time, common garden experiments on a subset of 308 genotypes measured during two consecutive years for eleven traits, as well as genotyping data to follow the fate of individuals throughout pedigrees.

Materials and methods

Saclay DSEs

Two independent Divergent Selection Experiments (DSEs) for flowering time, have been conducted on Saclay's plateau since 1993 (corresponding to 22 generations in 2018), from two independent genetic backgrounds: an early-flowering American Dent, F252 registered in 1979 by the company Agri-Obtention, and a late Iodent dent, MBS847 (thereafter called MBS), registered by the company Mike Brayton Seeds in 1982. The selection scheme has previously been described in Durand *et al.* (2010, 2015); Desbiez-Piat *et al.* (2021). Briefly, within each DSE, the ten earliest (resp. ten latest) flowering individuals were selfed at each generation, producing each 100 offspring used for the next generation of selection within the Early (resp. Late) populations (Fig. S1). Within each population, we evaluated 100 offspring of a given genotype in four rows of 25 plants randomly distributed in a four-block design, so that each block contained 10 rows. We applied a truncation selection of 10/1000=1%. Following Durand *et al.* (2015); Desbiez-Piat *et al.* (2021), we designated as *progenitor*, a selected plant represented by its progenies produced by selfing and evaluated in the experimental design at the next generation. We conditioned selection on the maintenance of two families, *i.e.* two sub-pedigrees derived from two separate G_0 ancestors. Thus, each family was composed of three to seven progenitor at each generation with the additional condition that at least two different G_{n-1} progenitors were represented. Furthermore we applied more specifically a two-steps selection procedure, so that among the 100 offspring per progenitor, we recorded the flowering time of the 12 most extreme (most early/late) individuals per (early/late) family, *i.e.* $12 \times 5 = 60$ individuals per family or 120 per population. Records constituted the Saclay DSEs Yearly Measurements (thereafter DSEYM). To ensure the maintenance

through time of minimal fitness, we selected based on an index among the 12×5 earliest (resp. latest) individuals, the 5 earliest (resp. latest) individuals with the highest kernel weight per family. Seeds from selected genotypes at all generations were stored in cold chambers.

F252 and MBS genealogies can be traced back from generation 22 to the start of the divergent selection experiments, G0 (Fig. S2 and Fig. S3). The initial MBS pedigrees encompassed four families: ME1, ME2 composing the MBS Early (ME) population, and ML1, ML2 composing the MBS Late (ML) population. F252 Early (FE) population is composed of FE1 and FE2 families. F252 Late populations genealogies are more complex: FVL families (F252 Very Late in Durand *et al.* (2015)) ended at generation 14 with the fixation of a strong effect allele at the *eIF-4A* gene (Durand *et al.* 2015). To maintain two families in F252 Late population, two families FL2.1 and FL2.2 were further derived from the initial FL2. These two families genealogies are rooted in FL2 from a G3 individual.

Common garden evaluation in 2018 and 2019 - DSECG

A common garden experiment was conducted in 2018 and 2019 on Saclay's Plateau (thereafter DSECG). We followed a sampling strategy that allowed for the best estimation of progenitors breeding values (David *et al.* 2022). Sampled progenitors, encompassing 155 MBS (Fig. S2) and 153 F252 (Fig. S3), were evaluated in 2018 and 2019 except for FVL which was not re-evaluated fully in 2019, because the latest generation flowered much later than other progenitors.

All seeds were produced in a nursery in 2016 from 25 S1 progenies for each selected progenitor of the genealogy. S2 seeds, obtained by selfing S1 individuals harvested in bulk, constituted the seed lots used in the evaluation trials. The evaluation trials encompassed four randomized-blocks, two for F252 S2 seeds and two MBS S2 seeds. Early (resp. Late) flowering progenitors were randomly distributed in 13 (resp. 12) plots of 14 rows of 25 plants. Within blocks, plots of Early and Late progenitors were grouped by three to four in sub-blocks. Overall, each progenitor was replicated at least twice in two rows of 25 plants randomly distributed among sub-blocks. Note, that some progenitors were replicated more often (up to four times). One row of 25 plants from each of the two initial inbred lines F252 or MBS (G_0) were used as control in each plot.

A total of 10 traits were recorded during both evaluation years. "Flowering time" (FT) was expressed in Days To Flowering equivalent to a growth at 20°C (DTF therefater) following Parent *et al.* (2010). We defined flowering time of progenitor Y_i, represented by a row of 25 plants, as the average flowering date. We recorded flowering time (t_i) as the number of plant (Z_i) for which silks were visible and pollen covered two third of the tassel. Hence, we actually observed the number of plants that effectively flowered between t_{i-1} and t_i. We therefore estimated $\widehat{Y}_i$ as:

$$\widehat{Y}_i = \frac{\sum_{i=1}^{n}(t_i + t_{i-1})/2 \times Z_i}{\sum_{i=1}^{n} Z_i} \tag{1}$$

Note that in DSEYM, flowering times were recorded for the 12 most extreme plants only, while in DSECG flowering time of a progenitor was defined as the mean flowering time per row. Hence we did not measure exactly the same trait in the two experiments. However, Durand *et al.* (2015) showed that there was an extremely high correlation between the two measures (r = 0.83 for F252 and r = 0.88 for MBS, p-values $< 2.2 \times 10^{-16}$, in both cases). We therefore used DSEYM to analyze the response to selection over the 22 generations, and compared it to that observed in DSECG.

Moreover, we recorded for 10 plants per row: the plant height (HT) (measured as the distance in cm between ground level and tassel basis), the rank of the upper ear (UE) and of the lower ear (LE), the length in cm of the leaf (LL) blade for the leaf located just below the upper ear, the rank of the upper node with brace roots (BR), the total number of visible leaves (#L). We considered for the subsequent analyses the average over these 10 plants as the phenotypic value. In addition, we recorded the number of visible leafs for these 10 plants every 5 days during the linear part of the vegetative growth. We then computed the phyllochron (PHY) - the time period (in DTF Eq. 20°C) between the sequential emergence of leaves - as the regression slope of the number of leaves over the thermal time during the linear developmental time response. Finally, the thousand kernel fresh weight (TKW in g) and the weight of the upper ear (EW in g) were recorded and averaged across 7 plants per row at complete maturity. Data from F252 and MBS were analysed separately.

Phenotypic data analyses of Yearly Measurements and Common Garden Evaluation

Saclay DSEs yearly measurement (DSEYM) analysis: Following Durand *et al.* (2010, 2015), we corrected the flowering time raw data from DSEYM for experimental design effects (blocks), and used F252 and MBS controls to correct for year effects. We used these estimated genetic values to further decompose the selection responses into two components, one due to initial standing variation and the second due to the incoming mutational variance (Durand *et al.* 2010; Desbiez-Piat *et al.* 2021).

To this end, we used Wray (1990) mixed model approach allowing for both estimation of the initial additive genetic variance σ_0^2 and additive mutational variance σ_m^2. The model can be written:

$$\boldsymbol{y} = \boldsymbol{1_n}\mu + \boldsymbol{Z}(\boldsymbol{u_0} + \boldsymbol{u_m}) + \boldsymbol{\epsilon} \tag{2}$$

Where,$\boldsymbol{y}$ is the vector of estimated genetic values after year and block effect correction, $\boldsymbol{1_n}$ is the vector 1 of size n, $\boldsymbol{u_0} \sim \mathcal{N}_N(\boldsymbol{0}, \sigma_0^2\boldsymbol{A_0})$, $\boldsymbol{u_m} \sim \mathcal{N}_N(\boldsymbol{0}, \sigma_m^2\boldsymbol{A_m})$, the residuals are i.i.d and $\boldsymbol{\epsilon} \sim \mathcal{N}_n(\boldsymbol{0}, \sigma^2\boldsymbol{I_n})$ and $\boldsymbol{Z}$ is an incidence matrix.

The kinship matrix $\boldsymbol{A_0}$, or additive genetic relationship matrix (neglecting dominance terms), is computed from pedigree information so that each individual element $a_{ij} = 2\Phi_A^{ij}$. Φ_A^{ij} is the kinship coefficient, the probability that an allele randomly drawn in individual i is identical by descent to a randomly drawn allele from individual j. If $i = j$, we can draw twice the same allele (probability 1/2) or the two alleles of i (probability 1/2) that are identical by descent in probability f_i, the inbreeding coefficient of i. Hence, we have: $\Phi_A^{ii} = 1/2 + 1/2 f_i$ or $a_{ii} = 1 + f_i$. Recalling that the inbreeding coefficient of an individual is equal to the kinship of its parents, and that under complete selfing, the inbreeding coefficient $f(g)$ is identical between all individual at generation g, we have for all progenitors:

$$f(g) = \frac{1}{2}(1 + f(g-1)) \tag{3}$$

with $f(0) = 0$ or $a_{ii}(0) = 1$, which can be rewritten:

$$f(g) = \frac{1}{2}(1 + f(g-1)) = \sum_{l=1}^{g} \frac{1}{2^l} = 1 - \frac{1}{2^g} \tag{4}$$

Hence,

$$a_{ii} = 2 - \frac{1}{2^g} \tag{5}$$

In the same way, for all pairs (i, j), we can easily compute the kinship coefficient from the genealogy: We made the assumptions that:

- if i and j don't have any common ancestor, $a_{ij} = 0$.
- if i and j are from different families (*e.g.* FE1 and FE2), $a_{ij} = 0$.
- if i and j have at least one common ancestor and k is the most recent, $a_{ij} = a_{kk}$.

In order to account for mutational effects, we made the assumption that mutations occurring at generation g are transmitted to their offspring and induce an additional correlation between breeding values at the subsequent generation (Wray 1990), albeit independent from the breeding values at the previous generation. This additional correlation is computed in the same way as for $\boldsymbol{A_0}$, but considering that all individuals between generations 0 to g are unrelated (because mutations are independent from each other). Let $\boldsymbol{A_g}$ be the kinship matrix between N progenitors at generation g due to mutational effects. We can write:

$$\boldsymbol{A_m} = \sum_{g=1}^{G} \boldsymbol{A_g} \tag{6}$$

Then, we defined $\theta = \frac{\sigma_m^2}{\sigma_0^2}$, the mutational variance in units of the additive genetic variance in the initial population. Mutational heritability was defined as: $h_m^2 = \frac{\sigma_m^2}{\sigma^2}$, *i.e.* the mutational variance in units of residual variance.

This allows us to write the total genetic variance-covariance matrix as:

$$var(\boldsymbol{u}) = \boldsymbol{A_0}\sigma_0^2 + \sigma_m^2 \sum_{g=1}^{G} \boldsymbol{A_g} = \left(\boldsymbol{A_0} + \theta \sum_{g=1}^{G} \boldsymbol{A_g}\right)\sigma_0^2 \tag{7}$$

The kinship matrices, $\boldsymbol{A_0}$ and $\boldsymbol{A_g}$ were computed using **makeA** function from R package **pedigree** (Coster 2013). The model parameters σ_m^2, σ_0^2 and σ were estimated using R package **sommer** (Covarrubias-Pazaran 2016, 2018).

Saclay DSEs common garden experiment analysis: All 10 traits measured in 2018 and 2019 (DSCG) were analysed separately using the same BLUPM decomposition as for DSEYM. However, to account for GxE interactions, the variance-covariance for the random effect due to standing genetic variation $\boldsymbol{Var(G^0)}$ (respectively incoming mutational variation $\boldsymbol{Var(G^m)}$) was modeled as:

$$\boldsymbol{Var(G^0)} = \boldsymbol{\Sigma_0} \otimes \boldsymbol{A_0} \qquad \boldsymbol{Var(G^m)} = \boldsymbol{\Sigma_m} \otimes \boldsymbol{A_m} \tag{8}$$

where $\boldsymbol{A_0}$ (resp. $\boldsymbol{A_m}$) is the kinship matrix defined previously and $\boldsymbol{\Sigma}$ is the covariance structure for progenitors among environments. We supposed an unstructured variance-covariance defined as:

$$\boldsymbol{\Sigma_{US_0}} = \begin{bmatrix} \sigma^2_{0_{2018}} & \sigma_{0_{2018,2019}} \\ \sigma_{0_{2019,2018}} & \sigma^2_{0_{2019}} \end{bmatrix} \quad \boldsymbol{\Sigma_{US_m}} = \begin{bmatrix} \sigma^2_{m_{2018}} & \sigma_{m_{2018,2019}} \\ \sigma_{m_{2019,2018}} & \sigma^2_{m_{2019}} \end{bmatrix} \tag{9}$$

The unstructured model assumes that $G \times E$ exists and that an environment-specific variance exists in addition to the resulting covariances.

Furthermore, spatial variation was modeled by adding field coordinates (plot and column) of each row as a random effect. The model can be written as :

$$\boldsymbol{Y} = \boldsymbol{X\beta} + \boldsymbol{Z_P P} + \boldsymbol{Z_C C} + \boldsymbol{Z_{G^0} G^0} + \boldsymbol{Z_{G^m} G^m} + \boldsymbol{E} \tag{10}$$

where :

- $\boldsymbol{\beta}$ includes μ the general mean, and a fixed year effects.
- $\boldsymbol{P}$ is a random plot effect per evaluation year such that $\boldsymbol{P} \sim \boldsymbol{\mathcal{N}_p(0, \Pi_{CS})}$, where Π_{CS} is a compound symmetry structure, with plot effects nested within sub-block.
- $\boldsymbol{C}$ is a random column effect per evaluation year such that $\boldsymbol{C} \sim \boldsymbol{\mathcal{N}_C(0, X_{DIAG})}$ with:

$$\boldsymbol{X_{DIAG}} = \begin{bmatrix} \sigma^2_{C_{2018}} & 0 \\ 0 & \sigma^2_{C_{2019}} \end{bmatrix}$$

- $\boldsymbol{G^0}$ is a random initial genetic effect per progenitor and evaluation year so that $\boldsymbol{Var(G^0)} = \boldsymbol{\Sigma_{US}} \otimes \boldsymbol{A_0}$
- $\boldsymbol{G^m}$ is a random mutational effect per progenitor and evaluation year so that $\boldsymbol{Var(G^m)} = \boldsymbol{\Sigma_{US}} \otimes \boldsymbol{A_m}$
- $\boldsymbol{X}$,$\boldsymbol{Z_P}$,$\boldsymbol{Z_C}$,$\boldsymbol{Z_{G^0}}$ and $\boldsymbol{Z_{G^m}}$ are the corresponding incidence matrices
- $\boldsymbol{E}$ the residuals so that $\boldsymbol{E} \sim \boldsymbol{\mathcal{N}_p(0, E_{DIAG})}$ with :

$$\boldsymbol{E_{DIAG}} = \begin{bmatrix} \sigma^2_{2018} & 0 \\ 0 & \sigma^2_{2019} \end{bmatrix}$$

The environment specific BLUPs $(G^0_{ik} + G^m_{ik})$ adjusted for covariances were used in the subsequent analysis.

The validity of this model (Eq. 10) was tested first by computing the distributions of residual values which allowed to verify homogeneity of variances and dispersion around 0, and second using a likelihood ratio test to compare it with a model without $G \times E$ where : $\boldsymbol{G^0} \sim \boldsymbol{\mathcal{N}_p(0, \sigma_0^2 A_0)}$, $\boldsymbol{G^m} \sim \boldsymbol{\mathcal{N}_p(0, \sigma_m^2 A_m)}$ and $\boldsymbol{E} \sim \boldsymbol{\mathcal{N}_p(0, \sigma^2)}$

Selection response analysis: We estimated the mean annual genetic gain for each trait as the slope of the linear regression between the predicted environment specific genetic values and generations. Each trait, evaluation condition, and family were analysed independently.

Distribution of mutational effects: To approximate the DFE of incoming mutations, we used the individual-predicted breeding values due to incoming mutations u_m in Eq. 2 and G^m Eq. 10 that we centered around the mean value of each corresponding generation for each family independently. This procedure allowed us to remove the effect of selection response. To approximate the DFE of selected mutations, we computed the distribution of mutational effects from mutational breeding values by conditioning on whether one of the progenies of the focal progenitor were selected or not in the next generation. To increase analysis power, we pooled the distributions across families of the same population (early or late flowering populations) accounting for the direction of selection (negative sign for unfavorable mutational effect and positive sign for advantageous ones). Hence we obtained a distribution based on 20 estimates per generation (individuals) per population.

Genotyping data

In order to produce genotypic information for all individuals along the pedigree at potentially selected site and *de novo* mutations, SNPs were detected between early and late populations from RNAseq data. A subset of individuals genotyped for these SNPs allowed us to subsequently infer all genotype for all individuals using pedigree information.

SNP detection: We used a RNAseq dataset from five Early and Late progenitors of generation G13 of Saclay's DSEs, originally produced to study the genes differentially expressed in the apical meristem during floral transition by Tenaillon *et al.* (2019). The use of an RNAseq dataset conditioned the detection of SNPs in genes expressed in the apical meristem, representing about 55% of all annotated maize genes.

Choice of contrasted genotypes for variant discovery: Briefly, each early/late population was represented by five progenitors (G13) of the G14 generation (2010), corresponding to the last generation of FVL family (Very Late F252) (Tenaillon *et al.* 2019). The five progenitors represented five out of the ten families of the DSEs (Fig. S2 and Fig. S3). Each G13 progenitor was represented by a bulk of S2 seeds collected at G14 from the progenies that have been evaluated but not retained by selection. Seeds from the five chosen progenitors were sown in the field in 2012 and 2013. Each year, plant meristems were dissected on a daily basis for a period of roughly one month. Meristem status were recorded and sampled meristems of the same developmental stage (same visible leaf number) were pooled. RNAs were extracted from 25 pools of meristems (each constituted by 16 to 31 meristems from the same progenitor and developmental stage) collected during the two years. Hence the 25 RNAseq libraries produced corresponded to two or three developmental stage per year and per progenitor.

Variant discovery from RNAseq: The RNAseq libraries were sequenced using 51 bp Illumina single reads. Because, we aimed at detecting SNPs between Early and Late genotypes within each DSE (F252 and MBS), we pooled RNAseq data from all libraries corresponding to the same progenitor, albeit different developmental stages, in a unique fastq file. More specifically, we pooled 6, 7, 4, 5, 3 libraries for each unique G13 individuals in FE1, FL2.1, FVL, ME2 and ML1 families, called FEE, FLL, FVL, MEE, MLL, respectively in Tenaillon *et al.* (2019) (Fig. S2 and Fig. S3). Reads were trimmed and filtered for low quality and rRNAs were filtered out, following the procedure described in Tenaillon *et al.* (2019). Total number of reads per progenitor ranged between 59 399 604 and 96 708 953 (Table S1).

We further performed variant discovery between the Early and Late genotypes chosen at G13 from the RNAseq reads, within each inbred line independently. To do so, we followed the best practices of the Genome Analysis ToolKit (GATK, Auwera *et al.* (2013)) considering each of the five genotypes independently. We first mapped all reads on the B73 maize reference genome V4 (Jiao *et al.* 2017) using STAR (2.6.1) aligner (Dobin *et al.* 2013). We used the two-pass mode, in which a first mapping step detects spliced junctions that are subsequently employed as additional information to map the reads. We used the default parameters, except for the maximum number of duplicated match a read is allowed, that we set equal to one, hence keeping reads that strictly map to one locus. As for the post-mapping step, we used the Picard set of tools (3.8) to (1) index the reference genome, add read group information and sort the reads; (2) retrieve duplicates using MarkDuplicates; process reads incorrectly-mapped to intronic regions with SplitNCigarReads before using ReassignOneMappingQuality; recalibrate the quality scores thanks to baseRecalibrator, using the known variants (Chia *et al.* 2012) (downloaded from Ensembl database (ensembl;version=90;url=http://e90.ensembl.org/Zea_mays.)). We further called SNPs using the GATK's tool HaplotypeCaller with a minimum PHRED score of 30.0. Next, we ran variant filtering steps with the VariantFiltration tool. Following GATK guidelines for RNA-seq data: we discarded clusters of at least 3 SNPs that were within a window of 35 bases by adding -window 35 -cluster 3 to the command; we filtered on Fisher Strand values ($FS > 30.0$) and Quality By Depth values ($QD > 2.0$). SNPs falling into non-assembled remaining scaffolds, chloroplastic or mitochondrial DNAs were eliminated. Because we expected very few heterozygous SNPs after 13 generation of selfing, we discarded them. Finally, we applied stringent filters for raw QUAL scores ($QUAL > 40$) and genotype quality ($GQ > 20$) and required that at least 5 reads covered a given SNP ($DP > 5$). Altogether, the variant discovery pipeline retained 46 SNPs in the MBS line and 7,030 SNPs in the F252 line.

SNPs subsampling for KASPar™ genotyping: All 46 SNPs detected between MEE and MLL were retained and used subsequently to genotype MBS progenitors. Overall, most SNPs detected for MBS were located on chromosome 10 in 5 annotated genes (Table S2 and Table S3).

For F252, we subsampled 480 SNPs among the 7,030 detected SNPs between FVL, FLL and FEE. To do so, we defined several categories to maximize genome coverage of potentially selected site, while trying to identify *de novo* mutations. First, we decided to preferentially retain SNPs that fell within genes possibly involved in the genetic determinism of flowering time. We considered known flowering time genes in maize (**F_Candidate** in Tenaillon *et al.* (2019)), genes detected as differently expressed between Early and Late G13 progenitors in the RNA-Seq experiment (**Sel** genes in Tenaillon *et al.* (2019)) and genes associated to flowering time variation in a panel of 4,471 inbred lines/landraces ((Romero Navarro *et al.* 2017), **GWA_Candidate** in Tenaillon *et al.* (2019), Fig. S4). Because the DSEs are conducted under complete selfing and effective recombination is expected to be low, SNPs tended to form clusters. We defined these clusters without prior information using a k-means approach on the Euclidean distances between SNP positions (Fig. S5 and Fig. S6). Table S4 shows that the distribution of SNPs along the chromosomes was heterogeneous with only 4 SNPs in chromosomes 4 and 7, up to 131 in chromosome 6. Because we were interested in finding *de novo* mutations, we retained all the SNPs found isolated in 20kb regions, thereafter called **ALONE** (Fig. S4). As for clusters of SNPs, we retrieved one SNP every 200bp within candidate genes, and one SNP every 5 SNPs among SNPs separated by at least 200bp in cluster without candidate genes. Selected SNPs retained for F252 fell within 364 genes, 318 of them being represented by a single SNP, and 46 being represented by two to four SNPs. 48 SNPs were located in genes not annotated in B73 AGPv4 (Jiao *et al.* 2017) but present in the RNAseq data.

Inferring genotypes from partial KASPar™ genotyping data and pedigree relationships:

In addition to the 308 progenitors measured in common garden experiments, all progenitors along the ancestral path of generation 13 (generation at which SNPs were detected) were genotyped so that overall, 187 F252 (+3 duplicated genotypes from different seed lots, *i.e.* genotyping replicates) and 190 MBS

independent progenitors were effectively genotyped (Fig. S2 and Fig. S3).

DNAs were extracted from bulk of 15 plants (one standardized fresh leaf disk per plant, to ensure equimolar bulk). Extractions were performed from 30 mg of lyophilized adult leaf material following recommendations of DNeasy 96 Plant Kit manufacturer (QIAGEN, Valencia, CA, USA). We verified through simulations of our multiplication scheme, that the probability of not detecting one of the two alleles of an initial heterozygous progenitor was below 5% for a bulk of 15 S1, S2 or S3 plants.

The genotyping of 190 MBS progenitors for 46 SNPs and 190 F252 progenitors for 480 SNPs was conducting using KASPar™ technology (KBioscience's competitive allele-specific PCR amplification of target sequences and endpoint fluorescence genotyping) on the GENTYANE technical center from INRAE (http://gentyane.clermont.inra.fr/contenu/presentation) The genotyping process was conducted using IFC Dynamic Arrays 96*96 / IFC Controller HX / Juno / Biomark™ HD Reader. The genotype attribution was conducted semi-manually, following a blind protocol, using Biomark software from the Fluidigm® company. Then each data point was validated manually by two independent operators using pedigree information to check for non-Mendelian segregation.

We produced a sparse genotyping matrix using KASPar™ genotyping, so that genotypic information was available only for a subset of all progenitors. From this subset we aimed at inferring all genotypes of the genealogy until generation 18th. In order to do so, we developed a likelihood model (Appendix 1, Supplementary material), and used a parsimony algorithm developed by Durand *et al.* (2015) to infer missing data in the matrix of genotypes with the highest likelihood at every given SNP. In sum, for MBS (resp. F252), we produced an inferred genotyping matrix composed of 342 individuals and 41 SNPs (resp. 351 individuals and 456 SNPs). SNPs were oriented so that we followed in the subsequent analyses the fate of the minor allele.

Association genetics

Following Durand *et al.* (2015), we computed the additive (a) effects associated with each SNP, and for each trait independently, through linear regression:

$$G_{gp} = \mu_g + a.x_{gp} + \epsilon_{gp} \tag{11}$$

where G_{gp} is the environment specific (DSEYM or DSECG 2018 or DSECG 2019) predicted breeding value of progenitor p at generation g. μ_g is the average trait value calculated over all progenitors at generation g, and x_{gp} is an indicator variable equal to -1 for homozygous progenitor aa, 0 for heterozygous progenitor an 1 for homozygous progenitor AA. Allelic status A corresponded to the less frequent allele in the starting population at G_1. When $G1$ allele frequency was equal to 0.5, we arbitrarily chose A to be the reference allele of B73 AGPv4 reference genome (Jiao *et al.* 2017).

We tested the significance of the association between trait variation and the segregation of alleles by simulating a null distribution for the additive estimated effect a using gene dropping simulations and the same model as Eq. 11. For standing variation, genotypes were simulated by dropping the two possible alleles throughout the pedigrees considering heterozygous ancestors at generation G0. At each generation, the genotype of each progenitor was randomly drawn from the alleles produced by its ancestor assuming Mendelian inheritance (Durand *et al.* 2015). For *de novo* mutations, we proceeded similarly except that simulations started at the genealogical position of the mutated individual. Note that for both standing and *de novo* variants, the initial detection of SNPs from RNASeq data generated at generation 13 introduced an ascertainment bias, *e.g.* their detection was conditioned on their differential fixation between early and late populations at G13. Therefore, we only used the subset of simulations that presented the same genotypes in the 2 (resp. 3) individuals used for SNP detection in MBS (resp. F252). Interestingly, because of the small population sizes in our design (Desbiez-Piat *et al.* 2021), we expected standing alleles to be fixed at G_{18} within each family through drift (even without selection). This leads for each inbred line to different possible genealogical structures leading to a wide multi-modal distribution of possible additive values obtained through simulations (Fig. S7, Fig. S8 and Fig. S9). Hence, by conditioning on the observation of the genotype at generation G_{18}, we were able to accurately control for genetic structure and deconvolute this mixture of distributions. Overall, probabilities of observed a additive values among 5,000 simulations per case were determined (p-values) through a symmetrical test. In addition, we controlled for multiple tests by setting a 5% False Discovery Rate (FDR).

Furthermore, the set of simulated allele trajectories through gene dropping was also used as the null hypothesis of fixation time against which observed trajectories were tested.

Results

Two successive adaptive phases drive the selection response in Saclay's DSEs

For F252, the mean initial flowering time at G_0 was equal to 66.4 DTF, emphasizing an earlier flowering genetic background than MBS which initially flowered around 79.5 DTF (Fig. 1). A simple linear regression on total predicted breeding values (Eq. 2) over generations summarizes the raw responses to selection. Within the two genetic backgrounds, the strongest selection response was observed in late populations with 0.346 DTF per generation in ML2 and 0.332 in FL2 (Table 1). The response for FVL family was so strong (1.016), that G14 plants were not able to produce enough viable offspring for the next generation (Durand *et al.* 2012), and that FL2 family had to be split into two (FL2.1 and FL2.2) families to recover a second biological replicates. Interestingly, the selection response was asymmetrical, so that early families responded less than late families with genetic gains comprised between -0.138 and -0.243 DTF per generation in accordance with (Durand *et al.* 2015). In addition, the response to selection appeared also less variable across early than across late families in F252 and MBS (Table 1 and Fig. 1).

To investigate how much of the phenotypic response of Saclay DSEs observed from yearly flowering time measurements could be explained by initial standing variation *versus* incoming mutational variance, we used Wray (1990) BLUPM model. We estimated an initial standing variance of 3.15 (resp. 3.72) in MBS (resp. in F252), and mutational variance estimate of 0.357 (resp. 0.203) (Table 2). These translated into mutational heritabilities of 0.116 (resp. 0.152) in MBS (resp. in F252) (Table 2). Interestingly, the relative importance of mutational variance in the response to selection was higher in MBS with an estimate of θ of 0.113 than in F252 ($\theta = 0.05$, Table 2).

More detailed observations of the evolution of standing and mutational variance through generations of selection confirmed these trends (Fig. 1). In MBS, after 18 generations of selection the average total genetic value predicted by the model reached 8.6

Table 1 Selection response computed from total breeding values

Family	Mean genetic gain (in DTF eq. 20^oC)	Std. Error for genetic gain	R^2	G18 Cumulative Response
FE1	-0.138	0.008	0.220	-4.10
FE2	-0.180	0.008	0.391	-7.34
FVL	1.016	0.030	0.610	12.13
FL2	0.332	0.045	0.179	3.16
FL2.1	0.064	0.017	0.024	4.57
FL2.2	0.079	0.017	0.062	4.26
ME1	-0.243	0.006	0.601	-5.96
ME2	-0.197	0.007	0.443	-4.95
ML1	0.170	0.012	0.211	8.63
ML2	0.346	0.016	0.364	15.53

Table 2 Variance decomposition of the selection response for flowering time from yearly measurments. Variance components (Standard Error)[Zratio] are given for both genetic backgrounds.

	MBS	F252
σ_0^2	3.15 (1.34)[2.35]	3.72 (0.189)[19.7]
σ_m^2	0.357 (2.72E-02)[13.1]	0.203 (1.89E-02)[10.7]
σ^2	3.06 (6.62E-02)[46.3]	1.34 (5.85E-02)[22.9]
$\theta = \frac{\sigma_m^2}{\sigma_0^2}$	0.113 (4.97E-02)[2.28]	5.47E-02 (5.93E-03)[9.23]
$h_m^2 = \frac{\sigma_m^2}{\sigma^2}$	0.116 (9.28E-03)[12.5]	0.152 (1.57E-02)[9.67]

for ML1 but 15.5 DTF for ML2 (Fig. 1, right panel). In F252, the very late family FVL quickly responded to selection which led to a drastic shift around 12 DTF and the two derived late families FL2.1 and FL2.2 from FL2, were only shifted by 4 DTF (Fig. 1). The asymmetrical response to selection for early families was observed within each component of the selection, so that for example, ME1 (resp. ME2) total gain of -6.0 (resp. -5.0) could be decomposed into a standing variation effects of -1.2 (resp. -1.9) and a mutational effect of -4.8 (resp. -3.1), these cumulative effect being smaller in absolute values than their late counterparts. For F252, a shift around -1.3 (resp. -0.7) DTF was also reached due to standing variation in FE1 (resp. FE2), but mutations accounted only for -2.8 (resp. -3.7) DTF, so that they plateaued to a maximum shift around -4 DTF after 10 generations of selection. Finally, the decomposition of the selection response into a shift of 2.9 (resp. 3.7) DTF (left panel) for ML1 (resp. ML2) due to standing variation and a shift of 5.7 and 11.9 DTF respectively due to incoming mutational implied that mutations accounted for 67% and 77% for ML1 (resp. ML2) of the total genetic gain. On the other hand for FL2.1 and FL2.2 mutations accounted for 54% and 52% of the total genetic gain respectively (Fig. 1), which confirmed the prominent role of mutational input to the selection response in MBS.

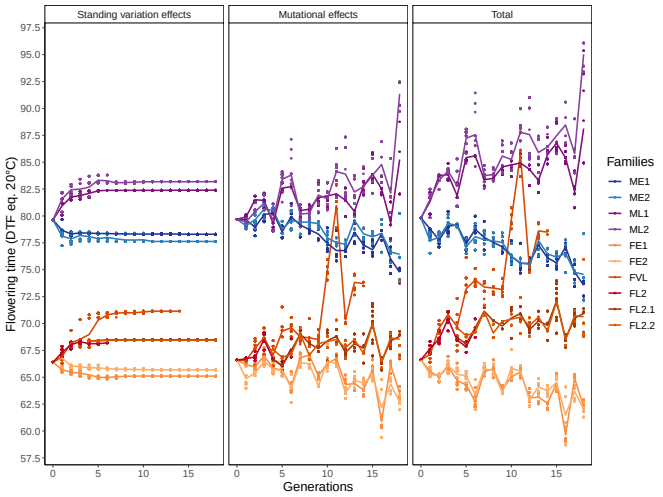

Figure 1 Decomposition of the breeding values (right panel) into an initial standing variation component (left panel) and a mutational effect component (middle panel), and their evolution through generations The right panels indicate the sum of the two predicted values in A) F252 and B) MBS. Colors indicate the different families and lines indicate the evolution of the mean value per generation and family through time. Each dot corresponds to a progenitor.

We approximated the distribution of the mutational effects of incoming mutations and that of the selected mutations. Compared with non selected incoming mutational effects that displayed an average effect of -0.439 DTF for MBS and -0.352 DTF for F252, we observed among the selected mutations, a strong enrichment in favorable mutations with an average mutational effect of $+0.299$ DTF and $+0.278$ DTF for MBS and F252, respectively (Table 3 and Fig. 2). The top 5% selected mutational effects were greater than $+2.09$ DTF and $+1.36$ for MBS and F252 respectively, while the 95 percentile of unselected mutational effects equaled $+1.1$ and $+0.683$ for MBS and F252. However, we selected up to 25% of unfavorable mutations in MBS (resp. 18% in F252) (*i.e.* with sign opposite to the selection direction) so that for example 5% of the selected mutations had effects below -1.01 in MBS and -0.739 in F252 (Table 3 and Fig. 2).

In order to get some experimental hints on the validity of our results, we followed the fate of a subset of standing variants and *de novo* mutations. We produced genotypic information at 41 (resp. 456) SNP for MBS (resp. F252) using KASPar genotyping technology. We inferred the genotypes of all individuals along the pedigrees. SNPs were detected from RNAseq data conditioning on their differential fixation between early and late populations at generation 13 (Tenaillon *et al.* 2019). Because of the high drift-high selection regime, differential fixation between populations can arise by either selection or drift. To enrich for potentially selected variants in our KASPar assays, we therefore devised a number of filters by targeting flowering time genes as well as flowering time genome wide association (GWA) hits.

Table 3 Mutational effect percentiles (Q) according to evaluation environments for selected and unselected mutations (in DTF eq. 20^oC)

Inbred	Selected	Env.	Q5	Q50	Mean	Q95
MBS	No	DSEYM	-1.94	-0.412	-0.439	1.1
MBS	No	2018	-1.42	0	-0.12	0.693
MBS	No	2019	-1.58	0	-0.128	0.826
MBS	Yes	DSEYM	-1.01	0.173	0.299	2.09
MBS	Yes	2018	-0.982	-0.00239	0.0818	1.47
MBS	Yes	2019	-1.07	0	0.0875	1.64
F252	No	DSEYM	-1.66	-0.335	-0.352	0.683
F252	No	2018	-0.882	-0.000976	-0.106	0.507
F252	No	2019	-1.17	0	-0.14	0.721
F252	Yes	DSEYM	-0.739	0.28	0.278	1.36
F252	Yes	2018	-0.857	0.0292	0.0837	1.02
F252	Yes	2019	-1.07	0.0175	0.11	1.3

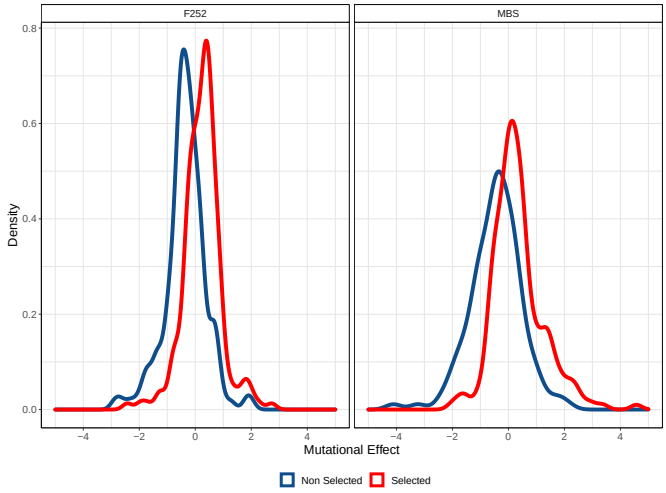

Figure 2 Distribution of non selected (blue distribution) and selected (red distribution) mutational effects in MBS and F252. Positive values correspond to mutational effects of the same sign as the direction of selection.

We detected two *de novo* mutations per inbred line (Fig. S10). Both mutations detected in MBS appeared in the late flowering ML1 family. The first one appeared at generation 3, on chromosome 2 at position 6,294,005. This mutation was the unique one within a 20kb-window. It appeared in the gene Zm00001d002125, also known as RPD2 which encodes the nuclear RNA polymerase D2/E2, the RNA polymerase IV second largest subunit. RNA polymerase IV plays a role in siRNA-directed DNA methylation (RdDM) and silencing of genes and endogenous repetitive elements; and it has also been shown to regulate flowering-time genes (Pikaard *et al.* 2008). It fixed in 3 generations. The second appeared at generation 10, on chromosome 6 at position 148,046,062. This mutation also appeared to be isolated (i.e. the single one within 20 kb-window). It fell within the Zm00001d038104 gene encoding for a mannosylglycoprotein endo-beta-mannosidase. Interestingly, this gene has been shown to be differentially expressed between the early and the late F252 genotypes at generation 13 (Tenaillon *et al.* 2019). It fixed in 4 generations. The two mutations detected in F252 appeared respectively in early flowering FE1 family and late family FL2.1 (note that FL2, FL2.1 and FL2.2 are represented together Fig. S10). The first one appeared at generation 4, on chromosome 3 at position 141,724,144 and was the unique detected SNP within a 20kb window, but did not lie within any annotated gene. It fixed in 6 generations. The second mutation appeared around generation 5 on chromosome 6 at position 130,321,359 and was the single one detected SNP within a 20kb window. It occurred in gene Zm00001d037579, coding for a serine/threonine-protein phosphatase 4 regulatory subunit 3. It fixed in 1 generation in FL2.1 (in the only FL2.1 progenitor of generation).

We devised a null model for fixation time that explicitly accounted for the generation of occurrence of the mutations (ancestor for standing SNPs and later generations for de novo) and their segregation along pedigrees. We performed gene dropping simulations to ask whether their fixation times were consistent with drift (H0). Comparison between observed and simulated allele trajectories for the 4 *de novo* mutations revealed that polymorphic SNPs fixed quicker (*i.e.* $T_{fix}^{Obs} \leq T_{fix}^{Sim}$) than expected by drift (Fig.3, Fig. S11). The observed fixation times (in 4,5,7 and 1 generation) were shorter than the mean fixation times under H0 (5.25,5.07, 7.2 and 3.3 generations, respectively, Fig.3) with correspondingly significant p-values (<0.05) for 3 out of 4 mutations (P-value=0.11 and <0.001 in all other cases, respectively). Deviations from H0 suggested that selection drove the observed patterns for 3 *de novo* mutations (MBS mutation 2 and the two F252 mutations, Fig.3). As for minor standing alleles, we observed no significant difference between the observed mean fixation time and the expected mean fixation time under H0 in MBS. In contrast, in F252 we observed a mean fixation time of 6.04 (SE:0.09) greater than the expected mean fixation time of 3.64 (SE:0.01) (Fig. S12).

Furthermore, the average number of generations for the minor standing alleles to be lost was smaller for observed SNPs with 6.55 (SE:0.19) generations compared with 8 (SE:0.02) for simulations under H0 in MBS. In F252, we measured an average number of generations for mutation loss of 5.71 (SE:0.11), also smaller than the 6.28 (SE:0.01) generations simulated under H0. Interestingly, in F252, 16% of the standing variants were lost quicker than 95% of the corresponding gene-dropping simulations, but 0.6% had a time-to-loss greater than 95% of the simulations. In MBS, the respective percentages were equal to 11% and 0% (Fig. S12). This suggests that selection might better eliminate minor unfavorable standing alleles, while being less efficient (longer than random fixation time) at fixing minor beneficial alleles.

Common garden experiments imperfectly mirror past intensity of selection response for flowering time

Historically, Saclay DSEs yearly measurements (DSEYM) of flowering time were used to estimate breeding values for each progenitor. However, because the environment varies from year to year, these estimates are intrinsically limited in their ability to disentangle genetic effects from phenotypic plasticity - the capacity of a genotype to produce multiple phenotypes in response to environmental variations - from $G \times E$ - when two different genotypes respond to environmental variation in different ways. Plasticity and $G \times E$ are widely present (de Villemereuil *et al.* 2016) and could explain part of the observed selection response. To test this hypothesis, we conducted two common garden ex-

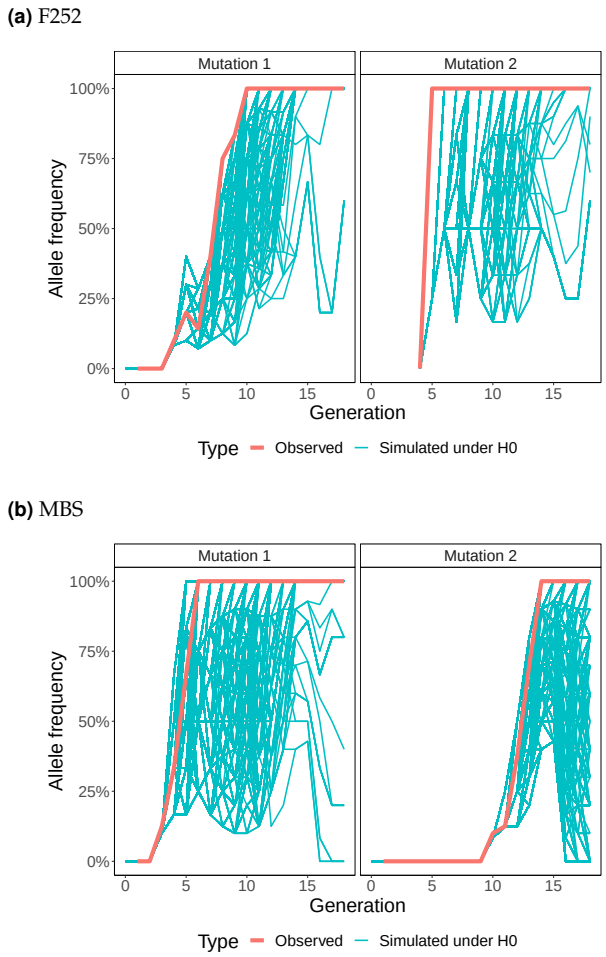

Figure 3 Allele frequency of *de novo* mutations through generations in F252 (a) and MBS (b). Red lines indicate the observed frequency changes while blue lines represent allele trajectories through gene dropping simulations.

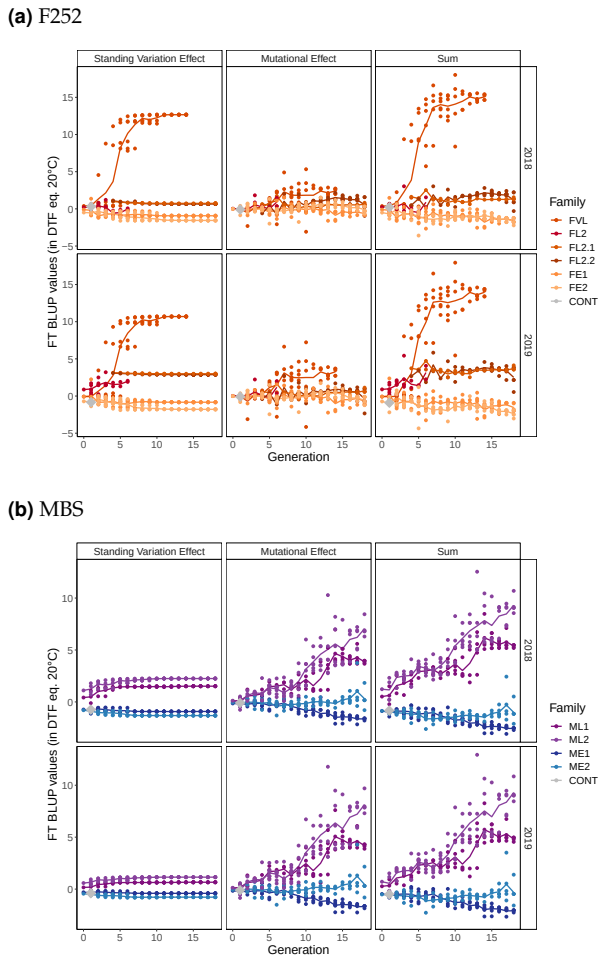

Figure 4 Decomposition of the environment specific breeding values (right panels) into an initial standing variation component (left panels) and a mutational effect component (middle panels), and their evolution through generations in (A) MBS and (B) F252. The right panels indicate the sum of the two predicted values. Colored lines indicate the evolution of the mean value per generation and family through time. Each dot corresponds to a progenitor.

periments in 2018 and 2019 (DSECG) aiming at evaluating the response to selection at 10 traits - including flowering time - across generations.

We used a likelihood ratio test to show that the model including GxE interactions (Eq 10) was significantly better than model without for all measured trait and the two genetic backgrounds ($p < 10^{-3}$). Similarly, we validated that model Eq. 10 with an unstructured variance-covariance performed significantly better than other variance-covariance structures using a likelihood ratio test ($p < 0.05$). We visually validated for flowering time the omnipresence of $G \times E$ interactions by plotting reaction norms using environment specific genetic values per progenitor (Fig. S13). Interestingly, few changes in rank between individuals were observed between 2018 and 2019 but significant changes in scale were observed. To characterize the impact of evaluation environment on the estimation of the selection response in DSECG, we fitted for each family and evaluation year independently, a simple linear regression model on the environment specific genetic values (Table S5). On average, all genotypes of all families flowered around 7.7 DTF eq. 20^oC (resp. 11.7 DTF eq. 20^oC) later in 2019 than in 2018 (Fig. S13) for MBS (resp. F252), exemplifying flowering time plasticity for all genotypes.

Analysis of climatic records revealed that the two evaluation years were rather similar and characterized by an exceptionally hot and dry summer compared to selection years (Fig. S14). Hence, $G \times E$ interactions could be improperly captured in DSECG because of the lack of environmental contrast between the two evaluation years. We therefore compared the DSECG environment specific breeding values to the ones computed from DSEYM that captured variable climatic conditions over the course of selection years/generations as highlighted by the large ranges of values shown in Fig. S14. In contrast with DSECG, we observed frequent rank changes in flowering time across progenitors (Fig. S13). In addition, we pinpointed important differences in the response to selection between DSECG and DSEYM. For late families, the observed selection response was less pronounced in DSECG compared with DSEYM (as shown Fig. S15). More precisely, within MBS, Late flowering ML1 and ML2 presented selection response approximately equal to DSEYM analyses in both evaluation years (around 0.2 and 0.4 DTF eq. 20^oC per

generation respectively, Table S5 and Table 1). For late F252 families compared with DSEYM, the observed selection responses were predicted as greater in 2018 and 2019 for FVL (1.3 in 2018 and 1.3 in 2019 compared to 1.02 DTF eq. 20^oC per generation in DSEYM), smaller for FL2.1 (0.048 DTF eq. 20^oC per generation in 2018, 0.012 in 2019 and 0.064 in DSEYM) and were not significant for FL2.2 (compared to a significant 0.072 DTF eq. 20^oC per generation genetic gain in DSEYM). For FL2 family, the ancestors of both FL2.1 and FL2.2, no significant response was observed in 2018 but a mean gain of 0.31 DTF eq. 20^oC was observed in 2019 and 0.332 DTF in DSEYM. For early families, the observed selection response was much less conserved in 2018 and 2019. Indeed, the mean genetic gain for ME1 around was around -0.1 DTF eq. 20^oC per generation in 2018 and 2019 (-0.24 in DSEYM), it was not significant for ME2 in 2018 and 2019 (-0.20 in DSEYM), and around -0.06 in 2018 and 2019 for FE1 (-0.14 in DSEYM), -0.05 and -0.08 for FE2 (-0.18 in DSEYM). Overall, our results suggest a pattern of selection response consistent across evaluation years (2018, 2019) and, between DSYEM and DSECG, towards lateness, while the pattern towards earliness was less pronounced and more variable between DSYEM and DSECG.

Finally, we asked whether the previous decomposition of the selection response into initial genetic variance and mutational variance was conserved in DSECG (Table 2 *vs* Table S6). Interestingly, the qualitative contribution of initial standing variance and mutational variance to the selection response in DSECG (represented by the predicted genetic values due to mutational input (middle panel) or to initial variance (left panel) Fig. 4) indicates a diversity of behaviours. For example, in ML1 and ML2, the strong observed response is due to the sum of both initial variance and mutational input that increases the time to flowering in 2018 and in 2019. Conversely, the reduced selection response compared to DSEYM of ME2, FE1 and FE2 is due to a reduced contribution of the effect of the mutational input - less expressed - in 2018 and 2019 (Fig. 1 *vs* Fig. 4). This translated with a highly reduced difference between the distribution of selected *vs* unselected mutational effects. The mean selected effects was around 0.08 DTF in 2018 and 2019 compared to 0.3 DTF in DSYEM for MBS and F252, while the average unselected effects were equal to around -0.1 in 2018 and 2019 compared to -0.4 in DSYEM (Table 3 and Fig. S16). On the other hand, the strong response to selection for lateness in FVL was due to a magnified effect of its standing variance contribution (Fig. 4).

Selection for flowering time drives the exploration of the multivariate phenotypic and genotypic space

We asked how selection for flowering time had impacted adaptive trajectories in the phenotypic and underlying genotypic space defined at 9 other non-focal traits measured in DSECG. We applied the same model (Eq. 10) on all measured traits and genetic backgrounds independently. Because all genetic variances of the phyllochron were not significantly different from zero (Table S6) for F252 and for MBS (except $\sigma_{m_{2018,2019}}$ $\sigma^2_{m_{2018}}$) *i.e.*, total leaf number could not be attributed to changes in leaf emission rate, we excluded this trait from subsequent analyses.

For the nine remaining traits including flowering time, we computed pairwise correlations between traits from breeding values (Fig. S17) and validated that trait correlations patterns were overall conserved across genetic backgrounds (F252 *vs* MBS). For example, our results highlighted a positive correlation between flowering time, leaf number and ear ranks in both genetic backgrounds, early and late populations and evaluation years. These correlation intensities were particularly pronounced in late families for which selection response for flowering time was the strongest (Fig. S17). Noticeably, while this group of trait was on average negatively correlated to yield components (TKW and EW) and to leaf length in late MBS and F252 populations, we observed null or positive correlations in early populations. Differences between early and late populations indicated that selection for flowering time in some instances impacted the structure of the genetic correlation matrix. Likewise, the evaluation environment (2018 and 2019) also impacted genetic correlations but in their intensities rather than in their signs (Fig. S17).

We next focused on the temporal patterns of correlative responses that is the exploration of the genotypic space over time. Families displayed distinct trajectories in the genotypic space under High-Drift High-Selection regime, yet repeatable between evaluation years (Fig. 5 and Fig. S18). This indicates that the correlations among traits are overall conserved. Slight differences in their magnitude across evaluation years (DSECG), however, resulted in pattern translation. Two mechanisms govern adaptive trajectories: first, the evolution of traits that are less correlated trigger a stochastic exploration of the genotypic space, and second the observed strong selection response for flowering time drove the evolution of correlated traits, (Fig. 5 and Fig. S18). Genotypic evolution related to flowering time and correlated traits was captured by the first PCA axis that explained 61% of the total variation ((Fig. 5). This axis differentiated early from late flowering populations. In contrast, the second and third axes that captured 22% and 7% of the variation respectively, highlighted a stochastic space exploration of families within early and late population for traits such as leaf length, plant height, thousand kernel weight (TKW), and ear weight, especially in MBS. In MBS early families, a positive correlation was observed between flowering time and plant height (0.56) while a negative one was observed in MBS late families (-0.82) suggesting variation in internode length between populations (Fig. S19 and Table S5). Interestingly, a global trend of decreasing leaf length was observed in all F252 families (Fig. S20), and in early MBS families, such that ME2 leafs length had decreased by almost 7cm by generation 10 (Fig. S19, Table S5).

We asked more specifically what was the role of incoming mutations on the exploration of the genotypic space. All mutational variances and covariances for both genetic backgrounds were significantly different from 0 (Table S6) which suggested that incoming mutational variation sustained the exploration of all other axes of the genotypic space. We centered mutational effect within generation and family to remove selection response effect. Pearson's correlation coefficients for all pair of traits highlights the high degree of pleiotropy of incoming mutations (Fig. 6). In line with results computed from breeding values, the structure of the correlation matrix was conserved between genetic backgrounds, but not between late and early populations within genetic background. For example, plant height tended to be negatively correlated with total leaf number, ear ranks, brace roots in late MBS and F252 but positively correlated in both early MBS and F252 populations. This is also the case of leaf length, an other growth parameter. This suggested that incoming mutations interacted epistatically with the genetic background. Interestingly, while correlation matrices computed from incoming and standing variants were generally consistent (Fig. S21; Fig. 6), we pinpointed to some differences in sign and intensity. For example in late F252, leaf length and

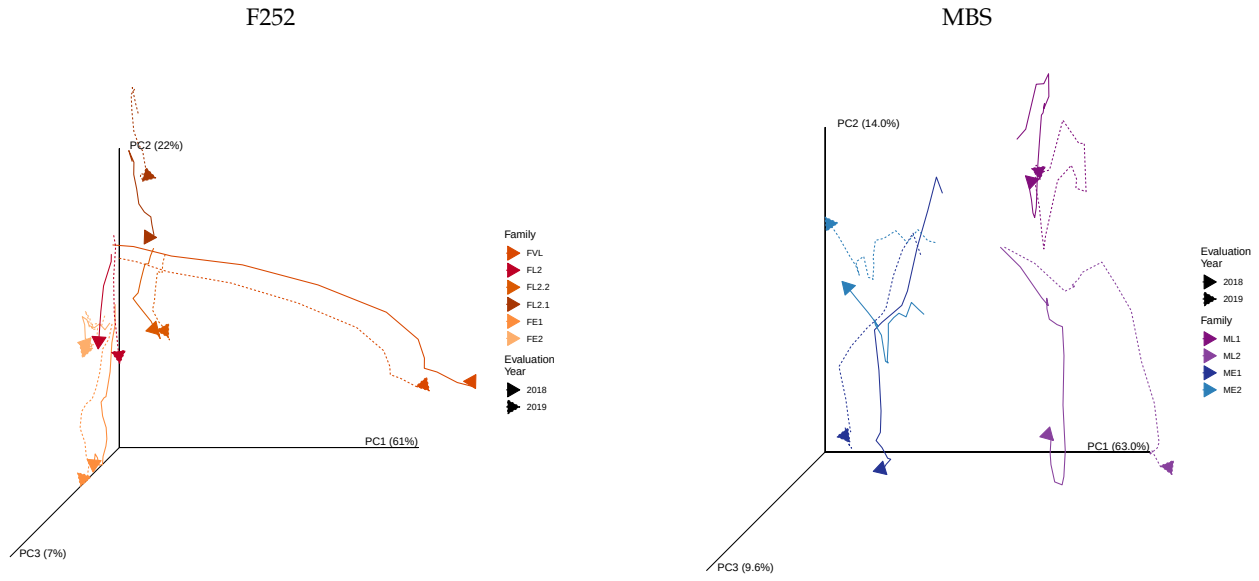

Figure 5 Evolution through generations of the multitrait breeding values across families in 2018 and 2019 for F252 and MBS. The genotypic space characterised through 9 traits was summarized through PCA on total BLUP values. Colored lines indicate the evolution through time of the rolling mean per generation, family and evaluation year on a 3 years window. Colors indicate the different families. Solid lines correspond to 2018 while dotted lines refer to 2019.

leaf number where negatively correlated when considering incoming mutations but positively correlated when considering standing mutations (Fig. S21, Fig. 6); and in late MBS flowering time was negatively correlated to plant height considering *de novo* mutations but positively correlated considering standing variation. This observation may explain abrupt changes in the direction of the exploration of the phenotypic space after 5-6 generations, for example for ML2 or FL2.2 in Fig. 5.

In order to provide an experimental validation of standing variant and *de novo* mutation effects as well as to explore their degree of pleiotropy, we conducted an association study on a restricted set of 456 and 41 SNPs for F252 and MBS respectively. Strikingly, 3 of the 4 detected *de novo* mutations were significantly associated with several traits, reinforcing the hypothesis of high degree of pleiotropy of selected *de novo* mutations. Indeed, in MBS, the 2 detected mutations on chromosome 2 and 6 were significantly associated with at least one of the traits (Table 4, Fig. S22). More specifically, the mutation on chromosome 2 was significantly associated to flowering time measured from DSEYM with an additive effect of 1.43 DTF Eq. 20^oC (Table 4), and to flowering time in 2019 with an effect of 0.73, but not significantly associated in 2018 despite a strong effect of 0.93 DTF Eq. 20^oC. This mutation was also significantly associated to leaf length in 2018 and 2019 with effects of 1.06 and 1.14 cm respectively. The other mutation detected on chromosome 6 in MBS was only associated to plant height in 2019, despite strong estimated effects of 0.90 from Saclay DSEYM, 0.63 in 2018 and 0.52 DTF Eq. 20^oC in 2019. Surprisingly, 37 out of 39 detected standing variants, that clustered together on chromosome 10, were associated to ear weight in 2018 and 2019 (Table S7). For F252, the two detected *de novo* mutations were significantly associated to flowering time in all evaluation environment (Table 4, Fig. S22) and the mutation located con chromosome 3 was significantly associated to 5 out of 8 measured traits in at least one evaluation year, while the mutation located on chromosome 6 was significantly associated to all measured traits in at least one environment. This high degree of pleiotropy contrasted with what we found for standing variants: out of the 454 detected standing variants, 99 were significantly associated to at least one trait, and only 11.3% were associated to more than 2 traits (Table S8). In F252, 80 different genes, located in 27 different cluster of SNPs presented at least one SNPs significantly associated to at least one trait. Only one SNPs (located in Zm00001d035439) presented a significant association with flowering time measured from DSEYM, but 32 others, located in 23 different genes in 8 different cluster (Fig. S22) were significantly associated to flowering time from 2018 and 2019 measurements.

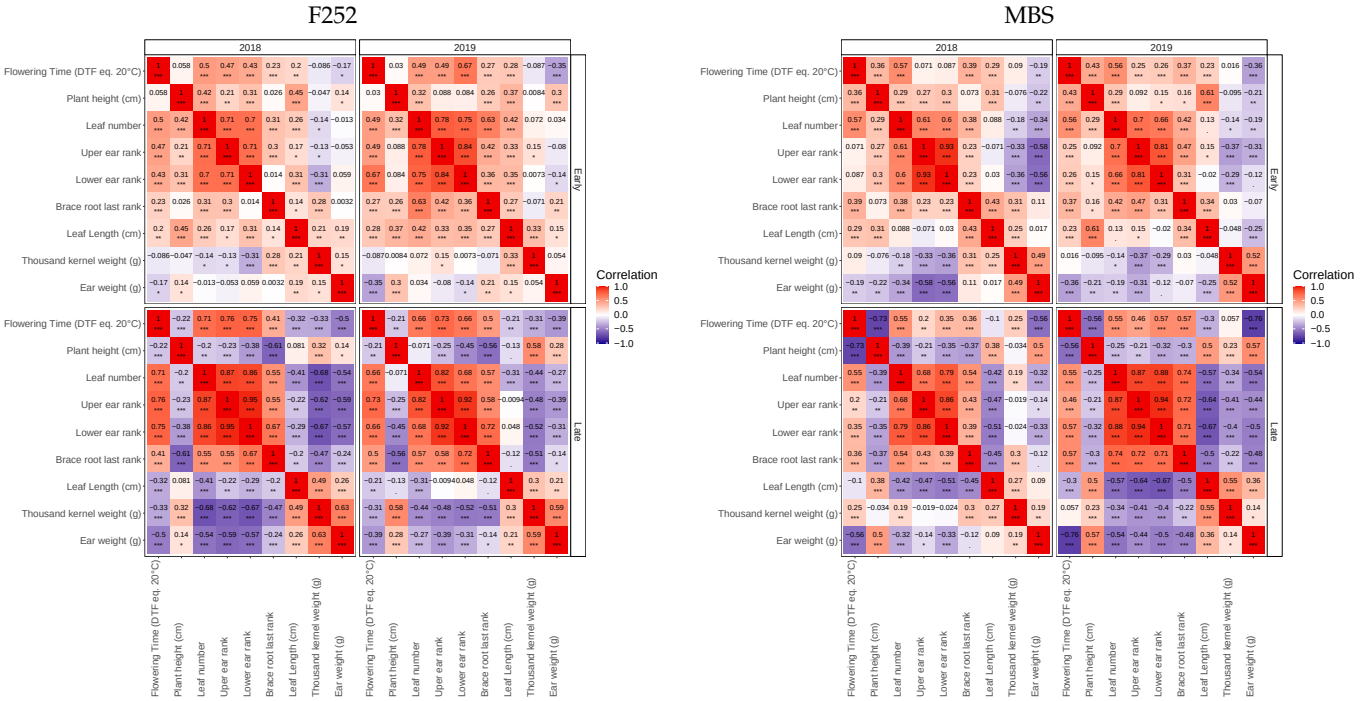

Figure 6 Pairwise correlation matrix between the predicted incoming mutational contribution for all measured traits in Early and Late populations in 2018 and 2019 for F252 and MBS. Pearson's correlation coefficients were computed after centering values per generation to remove past selection effects. Color corresponds the intensity of the correlations. '***', '**','*','.' indicates statistical significance at the 10^{-3}, 10^{-2},5×10^{-2} level, respectively.

Table 4 Significant trait association (allele effect) of four detected *de novo* mutations in 2018 and 2019. The first columns provide information on the chromosome, position, gene id and and known function.

Inbred	CHROM	POS	Gene id	description	2018	2019	DSEYM
MBS	2	6,294,005	Zm00001d002125	nuclear RNA polymerase D2/E2	LL(1.06)	FT(0.73); LL(1.14)	FT(1.43)
MBS	6	148,046,062	Zm00001d038104	Mannosylglycoprotein endo-beta-mannosidase	NA	HT(1.05)	NA
F252	3	141,724,144	NA	NA	FT(-1.18); HT(-3.51); BR(-0.04); LL(-0.47)	FT(-1.27); HT(-2.13); #L(-0.28); BR(-0.07); LL(-0.88)	FT(-1.57)
F252	6	130,321,359	Zm00001d037579	binding	FT(0.05); HT(3.08); #L(-0.02); UE(0.05); BR(-0.08); LL(0.64); TKW(5.66)	FT(0.43); HT(2.34); #L(-0.02); UE(0.05); LE(0.1); BR(0.02); LL(1.02); TKW(8.26); EW(0.55)	FT(0.8)

Discussion

In this work, we exploited a unique material derived from an artificial selection experiment on plants cultivated in agronomic conditions to explore two essential aspects of observed phenotypic shifts: the effects of mutations with respect to their standing versus *de novo* status, and the multitrait response to selection. We derived Saclay DSEs by applying truncation selection for flowering time in two maize inbred lines for 18 generations. From each of the two inbreds, two late and two early families were derived as independent replicates of the same selection scheme. Saclay DSEs display several peculiarities: effective population sizes are small ($Ne < 4$, (Desbiez-Piat *et al.* 2021)); selection intensity is strong (1% of 500 progenitors selected per family); plants are reproduced through selfing. Despite High Drift-High Selection (HDHS), phenotypic evolution is substantial, continuous (Durand *et al.* 2010, 2015) and sustained by a constant flux of *de novo* mutations. Previous simulation work mimicking our experimental procedure predicted an enrichment of fixation of beneficial mutations, and suggested that environmental effects played an important role in the dynamic of fixation of *de novo* mutations (Desbiez-Piat *et al.* 2021). Here, we first validated experimentally these predictions by quantifying the contribution of standing variation and *de novo* mutational variance to the observed selection response and by monitoring the fate of polymorphisms through generations. Second, we used common garden experiments to evaluate simultaneously plants from the 18 generations of selection addressing how $G \times E$ interactions had contributed to the response to selection, how selection on flowering time had impacted the evolution of correlated traits, and finally to which extent pleiotropy had shaped the phenotypic space exploration.

Two successive yet distinct modes of adaptation are at play is Saclay DSEs: We used an extension of the animal model proposed by Wray (1990) that explicitly accounts for the increase relatedness caused by incoming mutational variance (Wray 1990)

to analyse the selection response to selection in Saclay DSEs Yearly Measurement (DSEYM) and Common Garden experiments (DSECG). In line with previous results (Durand *et al.* 2010, 2015; Desbiez-Piat *et al.* 2021), we found that the observed strong selection response in Saclay DSEs can be decomposed in two successive phases with first, short term fixation of standing polymorphisms and second, a response sustained by the constant flux of incoming mutations (Fig. 1, Fig. 4). The relative importance of these two adaptive phases measured as the proportion of *de novo* mutational variance *vs.* standing variance ($\theta = \frac{V_m}{V_a}$) was consistent with a reduced initial standing variation in MBS compared to F252. Consistently, we detected fewer SNPs in MBS (46 SNPs) than in F252 from RNAseq data (7030 SNPs), a result corroborated by previous estimates of initial residual heterozygosity roughly 10-fold higher in proportion in F252 than MBS (Bouchet *et al.* 2013). Furthermore, the flux of incoming mutational variance, estimated through mutational heritabilities for flowering time —$\frac{V_m}{V_E}$ the ratio of mutational variance over residual variance— was unprecedentedly high (Table 2 and Table S6), an order of magnitude higher than the upper bound of previously measured estimates (10^{-2} and 10^{-4} (Keightley 2010)). These results contrasted with the ones that were computed from Saclay DSEs using the seven first generations ($\approx 2 \times 10^{-2}$) and a multi-step statistical model (Durand *et al.* 2010). Such discrepancy was most likely due to the fact that seven generations were not sufficient to fix standing variants, so that both sources of variation (standing *vs de novo*) were confounded in the initial phase of the selection response. On the other hand, mutational heritabilities for other traits were two orders of magnitude lower than for flowering time, hence falling within the range of common observations of h^2_m (Keightley 2010). Note that BLUPM model (Wray 1990) makes the hypothesis of a constant mutational input through generations under Gaussian incremental model (Clayton and Robertson 1955; Kimura 1965; Walsh and Lynch 2018) that might inflate mutational variance estimates (Walsh and Lynch 2018). Nevertheless, such model has been shown to be particularly relevant when effective recombination is limited as in Saclay DSE's (Charlesworth 1993; Walsh and Lynch 2018).

We investigated the allele fixation dynamic, considering both standing and *de novo* variants detected from RNAseq data. During the first phase of the selection response characterised by the fixation of standing variants, fixation times were equal to 3-4 generations in MBS and 5-6 generations in F252 (fig. S11). In accordance to selection limit theory for such small effective population sizes (Robertson 1960), these values matched the time at which a plateau was reached for the breeding values in MBS and F252 backgrounds (Fig. 1). Such fixation times were consistent with the modelling results that were calibrated on MBS data, but longer than expected in F252. Times to fixation in F252 were actually longer than expected under pure genetic drift which suggested that clonal interference impaired selection of beneficial variants in our selfing regime. Clonal interference is indeed known to slow down the fixation of beneficial mutations in bacteria (Gerrish and Lenski 1998; Desai and Fisher 2007; Park and Krug 2007), which is consistent with theoretical work showing that the loss of weaker adaptive alleles during a first selective sweep prevents fixation of multiple other mutations (Hartfield and Glémin 2016). Reduced standing variation in MBS likely explained the absence of clonal interference in this background. In contrast with the first adaptive phase, we expected no clonal interference in the second phase because fixation times are smaller than waiting times for new beneficial mutations to arise in the population (Gerrish and Lenski 1998). In line with those predictions, the four *de novo* mutations fixed in the predicted times (Desbiez-Piat *et al.* 2021).

From DSEYM, we approximated both the distribution of effects of all incoming mutations and the one of selected mutations. We found an enrichment in beneficial mutations in the selected offspring of a progenitor. Consistently, previous simulations showed that high stochasticity promoted the fixation of small effect beneficial mutations in this High Drift-High Selection regime (Desbiez-Piat *et al.* 2021). Simulations also predicted the fixation of unfavorable mutations (6% only), but to a lesser extent than what we observed (25% in MBS and 17% in F252). Several non-exclusive hypotheses can be formulated here. First, our model considered only additive variance terms. But, epistasis might be a key player of the selection response in our DSEs as shown by earlier work (Durand *et al.* 2012) and the multivariate distribution of incoming mutations varying between early and late populations Fig 6. In other words, epistasis can promote the fixation of favorable mutations in their context of appearance, which later appear as unfavorable in a modified genetic context. In the same vein, directional epistasis and allele specificity makes the order of mutations critical as has been shown in *E. coli* where the fixation of the first mutations determines the effect and fixation of the following ones through the modification of their genetic context of appearance (Plucain *et al.* 2014). Furthermore, in the case of negative epistasis —when the mean mutational effect increases as fitness decreases— selection for low trait values can be impaired (Silander *et al.* 2007). In Saclay DSE, a possible explanation for selection response asymmetry could reside in a fitness decrease in early families that in turn, would respond less to selection than the late ones in DSEYM (Durand *et al.* (2015) and Fig. 1). The second explanation for the excess of fixation of unfavorable mutations is the environmental fluctuations through generations of selection (Fig. S14) where a favorable mutation occurring in one environment might appear in the later generations as unfavorable (Chen and Zhang 2020). For example, mutations that are unfavorable on average across environments but that confer a transient beneficial advantage might be more likely to fix than mutations that are always neutral or beneficial (Cvijović *et al.* 2015). Such effects of antagonistic pleiotropy on fitness have been shown to be key players in local adaptation (Savolainen *et al.* 2013; Scarcelli *et al.* 2007; Chen and Zhang 2020).

Evaluation environments do not mirror past selection environments: Previous simulation results pinpointed the importance of micro-environmental effects on the stochastic fixation dynamics of *de novo* mutations under HDHS (Desbiez-Piat *et al.* 2021). However the model did not take into account $G \times E$ interactions, nor did DSYEM allow for the quantification of its impact on phenotypic shifts. Here, the implementation of a two-years common garden experiment (DSECG) revealed the preponderance of GxE interactions, which impacted the selection response for flowering time in several respects. Comparison between DSEYM and DSECG highlighted the fixation of environment-dependent unfavorable mutations during selection response, as differences between selected and non-selected mutations were erased in the evaluation environments (Table 3 and Fig. S16), so that some beneficial mutations in DSEYM were unfavorable in DSECG, which suggests that the same process applies between generations within DSEYM with changes in allelic effects between selection years. Corroborating this results, the detected mutation on chro-

mosome 2 in ML1 family occurred in Zm00001d002125, also known as RPD2, which has been shown to regulate flowering-time genes in an environment-dependent manner (Pikaard *et al.* 2008) through siRNA-directed DNA methylation (RdDM). Interestingly, looking at the selection response decomposition, we observed a certain antagonism between initial standing variation and mutational effect, especially in early flowering populations modulated by GxE interactions, so that either fixed standing variation or *de novo* mutations compensated for the decrease in flowering time through generations in DSECG (Fig. 4) suggesting a certain amount of compensatory epistasis (Rojas Echenique *et al.* 2019) modulated by the evaluation environment. Looking at the total selection response, $G \times E$ interactions while significant in DSECG, were mainly visible through scale effects, which magnified the asymmetry of the selection response against earliness observed in DSYEM. This can be interpreted because the two years of evaluation (2018 and 2019 on the Saclay plateau) were characterized by a hot summer (Fig. S14), so that early flowering populations flowered in a shorter time window that lead to the observed asymmetrical selection response. Further comparison between DSEYM and DSECG environment specific breeding values (Fig. S13) resulted in numerous rank changes. This results echoes with Choquette et al. (unpublished) result's that computed the large impact of adaptive plasticity in the total selection response measured in a complete reciprocal transplant experiments in eight environments of selection.

Our results more broadly question the use of the modern environment to understand past selection events that have shaped the current architectures of traits highly sensitive to environmental conditions. Hence trait expression in the environment of past selection may differ drastically from that of the present-day environment. This is well illustrated in teosintes whose phenotypic characteristics in late glacial-like climatic conditions (low temperature and CO2 levels) differed markedly from that of present-day conditions (Piperno *et al.* 2015). Such plasticity could have drastic effects on association studies particularly for climate-sensitive quantitative traits such as flowering time (Bergelson and Roux 2010). In line with these findings, for the gene Zm00001d047269, encoding the EARLY FLOWERING 4 protein, we found association with flowering date neither in 2019 or nor in DSYEM, despite a significant association in 2018 and strong effects observed on flowering time (3.11 DTF in 2018, 3.46 DTF in 2019, 3.61 DTF at DSYEM). It is remarkable that despite the homogeneity of our genetic backgrounds we found such discrepancy across our GWA studies. A previous study on flowering time in*A. thaliana* has pinpointed to a lack of reproducibility of GWA owing to genetic heterogeneity across populations (Lopez-Arboleda *et al.* 2021). Here we argue that the varying effects of alleles across environment are also key to explain the discordance among GWA studies performed across multiple environments in accordance to (Li *et al.* 2010), and the lack of power to detect significant associations when combined in single-data sets. Our results also raise the question of the application of association mapping in populations submitted to High-Drift High-Selection: on one hand many small-effect mutations follow adaptive trajectories comparable to neutral mutations, on the other hand, large effect mutations fix quickly and are detectable within populations only over restricted time windows. Hence, while the identification of variants underlying phenotypic variation in populations submitted to HDHS constitute a major goal for breeders and evolutionary geneticists, the discovery of alleles "that matter" might remain elusive (Rockman 2012). Note that despite these limitations, we managed to associate the four *de novo* mutations detected to a trait correlated to flowering time suggesting that strong pleiotropic effects may actually facilitate the detection of associations.

Pleiotropic mutational input drives Saclay DSEs correlative selection response: The patterns observed suggest distinct degree of pleiotropy between the standing variants selected during the first phase of adaptation, and the incoming mutations selected during the second phase of adaptation. Among 456 detected standing variants, 99 were significantly associated to at least one trait, but only 11.3% were associated to more than two traits indicating a lower degree of pleiotropy than that observed for four *de novo* mutations which associated with 2, 1, 5, and 8 traits (Table 4). Although we have little power to formally test for this difference, it is interesting to note that this pattern parallels what we observed regarding the pairwise-trait correlations. Correlations between standing variations effects Fig. S21 were indeed overall less conserved between years and genetic backgrounds – with the exception of the FVL family which fixed a standing variant of major effect in the first few generations (Durand *et al.* 2012)– than those computed on the predicted effects of incoming mutations (Fig. 6).

Correlative responses in Saclay DSEs are best explained by developmental constraints. Hence, correlations for traits such as flowering time, leaf length and plant height are predicted by developmental models of maize architecture (Zhu *et al.* 2014; Vidal and Andrieu 2020). These models also predict a correlation between blade length and plant size by the successive dependence of the blade length on sheath length, which impacts internodes length, and in turn plant height. Because developmental constraints may emerge from fixation of pleiotropic alleles (Hughes and Leips 2017), our results are consistent with: a first phase of adaptation with fixation of small to mild effects standing variants characterized by a restricted pleiotropy, allowing for a stochastic exploration of the phenotypic space (Fig. 5 and Fig. S18); and a second phase, where the fixation of strong effect of intermediate- to high-level pleiotropic *de novo* mutations restrict the phenotypic space exploration. In the omnigenic model of adaptation, this second class of mutations corresponds to the ones that are first fixed and display large effects both on the focal trait and other traits (Liu *et al.* 2019; Boyle *et al.* 2017). Corroborating this expectation, Frachon *et al.* (2017) showed that a small number of QTLs with intermediate degrees of pleiotropy drove adaptive evolution in nature. Note that selection itself may also contribute to reinforce genetic correlations during this second phase. Simulations of the evolution of gene regulatory network under directional selection have indeed depicted a trend towards gain of regulatory interactions and a global increase in the genetic correlations among gene expressions (Burban *et al.* 2022). This is because the rewiring of network is easier to achieve by adding connections on existing ones. Our results show a dynamic change in the patterns of correlations associated to a change in the source of polymorphism (standing variation then new mutations).

Data availability

Data will be available upon acceptance.

Acknowledgments

We wish to thank Randall Wisser for the insightful discussions and Hélène Corti for quality control work of the genotyping

data.

Funding

This work was supported by the grant Itemaize overseen by the French National Research Agency (ANR) as part of the "Investissements d'Avenir" Programme (LabEx BASC; ANR-11-LABX-0034) to C.D. GQE-Le Moulon benefits from the support of Saclay Plant Sciences-SPS (ANR-17-EUR-0007) as well as from the Institut Diversité, Ecolgie et Evolution du Vivant (IDEEV). A.D.-P. was financed by a doctoral contract from the French ministry of Research through the Doctoral School "Sciences du Végétal: du gène à l'écosystème" (ED 567), in addition to the French National Research Agency (ANR-16-IDEX-0006) and the France 2030 program.

Conflicts of interest

The authors declare that there is no conflict of interest.

Literature cited

Auwera GA, Carneiro MO, Hartl C, Poplin R, del Angel G, Levy-Moonshine A, Jordan T, Shakir K, Roazen D, Thibault J *et al*. 2013. From FastQ Data to High-Confidence Variant Calls: The Genome Analysis Toolkit Best Practices Pipeline. Current Protocols in Bioinformatics. 43.

Bergelson J, Roux F. 2010. Towards identifying genes underlying ecologically relevant traits in Arabidopsis thaliana. Nature Reviews Genetics. 11:867–879.

Bouchet S, Servin B, Bertin P, Madur D, Combes V, Dumas F, Brunel D, Laborde J, Charcosset A, Nicolas S. 2013. Adaptation of Maize to Temperate Climates: Mid-Density Genome-Wide Association Genetics and Diversity Patterns Reveal Key Genomic Regions, with a Major Contribution of the Vgt2 (ZCN8) Locus. PLOS ONE. 8:e71377.

Boyle EA, Li YI, Pritchard JK. 2017. An Expanded View of Complex Traits: From Polygenic to Omnigenic. Cell. 169:1177–1186.

Bulmer MG. 1971. The Effect of Selection on Genetic Variability. The American Naturalist. 105:201–211.

Burban E, Tenaillon MI, Le Rouzic A. 2022. Gene network simulations provide testable predictions for the molecular domestication syndrome. Genetics. 220:iyab214.

Bürger R. 1993. Predictions of the Dynamics of a Polygenic Character Under Directional Selection. Journal of Theoretical Biology. 162:487–513.

Bürger R, Lande R. 1994. On the distribution of the mean and variance of a quantitative trait under mutation-selection-drift balance. Genetics. 138:901–912.

Caballero A, Toro MA, López-Fanjul C. 1991. The response to artificial selection from new mutations in Drosophila melanogaster. Genetics. 128:89–102.

Chantepie S, Chevin LM. 2020. How does the strength of selection influence genetic correlations? Evolution Letters. 4:468–478.

Charlesworth B. 1993. Directional selection and the evolution of sex and recombination. Genetical Research. 61:205–224.

Chen P, Zhang J. 2020. Antagonistic pleiotropy conceals molecular adaptations in changing environments. Nature ecology & evolution. 4:461–469.

Chen Y, Lübberstedt T. 2010. Molecular basis of trait correlations. Trends in Plant Science. 15:454–461.

Chia JM, Song C, Bradbury PJ, Costich D, de Leon N, Doebley J, Elshire RJ, Gaut B, Geller L, Glaubitz JC *et al*. 2012. Maize HapMap2 identifies extant variation from a genome in flux. Nature Genetics. 44:803–807.

Clayton G, Robertson A. 1955. Mutation and Quantitative Variation. The American Naturalist. 89:151–158.

Coster A. 2013. *pedigree: Pedigree functions*. R package version 1.4.

Covarrubias-Pazaran G. 2016. Genome-Assisted Prediction of Quantitative Traits Using the R Package sommer. PLOS ONE. 11:e0156744.

Covarrubias-Pazaran G. 2018. Software update: Moving the R package *sommer* to multivariate mixed models for genome-assisted prediction. Preprint. Genetics.

Crow JF, Kimura M. 1979. Efficiency of truncation selection. Proceedings of the National Academy of Sciences. 76:396–399.

Cvijović I, Good BH, Jerison ER, Desai MM. 2015. Fate of a mutation in a fluctuating environment. Proceedings of the National Academy of Sciences. 112.

David O, Le Rouzic A, Dillmann C. 2022. Optimization of sampling designs for pedigrees and association studies. Biometrics. 78:1056–1066.

de Villemereuil P, Gaggiotti OE, Mouterde M, Till-Bottraud I. 2016. Common garden experiments in the genomic era: New perspectives and opportunities. Heredity. 116:249–254.

Desai MM, Fisher DS. 2007. Beneficial Mutation–Selection Balance and the Effect of Linkage on Positive Selection. Genetics. 176:1759–1798.

Desbiez-Piat A, Le Rouzic A, Tenaillon MI, Dillmann C. 2021. Interplay between extreme drift and selection intensities favors the fixation of beneficial mutations in selfing maize populations. Genetics. 219:iyab123.

Dobin A, Davis CA, Schlesinger F, Drenkow J, Zaleski C, Jha S, Batut P, Chaisson M, Gingeras TR. 2013. STAR: Ultrafast universal RNA-seq aligner. Bioinformatics. 29:15–21.

Doroszuk A, Wojewodzic MW, Gort G, Kammenga JE. 2008. Rapid Divergence of Genetic Variance-Covariance Matrix within a Natural Population. The American Naturalist. 171:291–304.

Durand E, Bouchet S, Bertin P, Ressayre A, Jamin P, Charcosset A, Dillmann C, Tenaillon MI. 2012. Flowering Time in Maize: Linkage and Epistasis at a Major Effect Locus. Genetics. 190:1547–1562.

Durand E, Tenaillon MI, Raffoux X, Thépot S, Falque M, Jamin P, Bourgais A, Ressayre A, Dillmann C. 2015. Dearth of polymorphism associated with a sustained response to selection for flowering time in maize. BMC Evolutionary Biology. 15:103.

Durand E, Tenaillon MI, Ridel C, Coubriche D, Jamin P, Jouanne S, Ressayre A, Charcosset A, Dillmann C. 2010. Standing variation and new mutations both contribute to a fast response to selection for flowering time in maize inbreds. BMC Evolutionary Biology. 10:2.

Falconer DS. 1971. Improvement of litter size in a strain of mice at a selection limit. Genetical Research. 17:215–235.

Fisher Ronald Aylmer S. 1930. *The Genetical Theory of Natural Selection.*. OxfordClarendon Press.

Frachon L, Libourel C, Villoutreix R, Carrère S, Glorieux C, Huard-Chauveau C, Navascués M, Gay L, Vitalis R, Baron E *et al*. 2017. Intermediate degrees of synergistic pleiotropy drive adaptive evolution in ecological time. Nature Ecology & Evolution. 1:1551–1561.

Gerrish PJ, Lenski RE. 1998. The fate of competing beneficial mutations in an asexual population, In: Woodruff RC, Thompson JN, editors, *Mutation and Evolution*, Springer Netherlands.

Dordrecht. volume 7. pp. 127–144.
Hartfield M, Glémin S. 2016. Limits to Adaptation in Partially Selfing Species. Genetics. 203:959–974.
Hill WG. 1982a. Predictions of response to artificial selection from new mutations. Genetical Research. 40:255–278.
Hill WG. 1982b. Rates of change in quantitative traits from fixation of new mutations. Proceedings of the National Academy of Sciences. 79:142–145.
Hill WG, Caballero A. 1992. Artificial selection experiments. Annual Review of Ecology and Systematics. 23:287–310.
Hospital F, Chevalet C. 1996. Interactions of selection, linkage and drift in the dynamics of polygenic characters. Genetical Research. 67:77–87.
Houle D, Bolstad GH, van der Linde K, Hansen TF. 2017. Mutation predicts 40 million years of fly wing evolution. Nature. 548:447–450.
Houle D, Morikawa B, Lynch M. 1996. Comparing Mutational Variabilities. Genetics. 143:1467–1483.
Hughes KA, Leips J. 2017. Pleiotropy, constraint, and modularity in the evolution of life histories: Insights from genomic analyses. Annals of the New York Academy of Sciences. 1389:76–91.
Jiao Y, Peluso P, Shi J, Liang T, Stitzer MC, Wang B, Campbell MS, Stein JC, Wei X, Chin CS *et al*. 2017. Improved maize reference genome with single-molecule technologies. Nature. 546:524–527.
Keightley PD. 2010. Mutational variation and long-term selection response, In: , John Wiley & Sons, Inc.. Oxford, UK. pp. 227–247.
Kimura M. 1965. A stochastic model concerning the maintenance of genetic variability in quantitative characters. Proceedings of the National Academy of Sciences. 54:731–736.
Kruuk LEB. 2004. Estimating genetic parameters in natural populations using the 'animal model'. Philosophical Transactions of the Royal Society of London. Series B: Biological Sciences. 359:873–890.
Lande R. 1979. Quantitative genetic analysis of multivariate evolution, applied to brain body size allometry. Evolution. 33:402–416.
Lande R, Arnold SJ. 1983. The Measurement of Selection on Correlated Characters. Evolution. 37:1210.
Li Y, Huang Y, Bergelson J, Nordborg M, Borevitz JO. 2010. Association mapping of local climate-sensitive quantitative trait loci in *Arabidopsis thaliana*. Proceedings of the National Academy of Sciences. 107:21199–21204.
Li Y, Suontama M, Burdon RD, Dungey HS. 2017. Genotype by environment interactions in forest tree breeding: Review of methodology and perspectives on research and application. Tree Genetics & Genomes. 13:60.
Lillie M, Honaker CF, Siegel PB, Carlborg Ö. 2019. Bidirectional Selection for Body Weight on Standing Genetic Variation in a Chicken Model. G3 Genes | Genomes | Genetics. 9:1165–1173.
Liu X, Li YI, Pritchard JK. 2019. Trans Effects on Gene Expression Can Drive Omnigenic Inheritance. Cell. 177:1022–1034.e6.
Lopez-Arboleda WA, Reinert S, Nordborg M, Korte A. 2021. Global Genetic Heterogeneity in Adaptive Traits. Molecular Biology and Evolution. 38:4822–4831.
Lush JL. 1943. Animal breeding plans. Animal breeding plans. .
Lynch M, Hill WG. 1986. Phenotypic evolution by neutral mutation. Evolution. 40:915–935.
Mackay TFC. 2010. Mutations and quantitative genetic variation: Lessons from *Drosophila*. Philosophical Transactions of the Royal Society B: Biological Sciences. 365:1229–1239.
Martin G, Lenormand T. 2008. The Distribution of Beneficial and Fixed Mutation Fitness Effects Close to an Optimum. Genetics. 179:907–916.
Moose SP, Dudley JW, Rocheford TR. 2004. Maize selection passes the century mark: A unique resource for 21st century genomics. Trends in Plant Science. 9:358–364.
Odhiambo MO, Compton WA. 1987. Twenty Cycles of Divergent Mass Selection for Seed Size in Corn. Crop Science. 27:1113–1116.
Parent B, Turc O, Gibon Y, Stitt M, Tardieu F. 2010. Modelling temperature-compensated physiological rates, based on the co-ordination of responses to temperature of developmental processes. Journal of Experimental Botany. 61:2057–2069.
Park SC, Krug J. 2007. Clonal interference in large populations. Proceedings of the National Academy of Sciences. 104:18135–18140.
Pikaard CS, Haag JR, Ream T, Wierzbicki AT. 2008. Roles of RNA polymerase IV in gene silencing. Trends in Plant Science. 13:390–397.
Piperno DR, Holst I, Winter K, McMillan O. 2015. Teosinte before domestication: Experimental study of growth and phenotypic variability in Late Pleistocene and early Holocene environments. Quaternary International. 363:65–77.
Plucain J, Hindré T, Le Gac M, Tenaillon O, Cruveiller S, Médigue C, Leiby N, Harcombe WR, Marx CJ, Lenski RE *et al*. 2014. Epistasis and Allele Specificity in the Emergence of a Stable Polymorphism in *Escherichia coli*. Science. 343:1366–1369.
Reinert S. 2022. Quantitative genetics of pleiotropy and its potential for plant sciences. Journal of Plant Physiology. 276:153784.
Roberts RC. 1966. The limits to artificial selection for body weight in the mouse I. The Limits Attained in Earlier Experiments. Genetical Research. 8:347–360.
Robertson A. 1960. A theory of limits in artificial selection. Proceedings of the Royal Society of London. Series B. Biological Sciences. 153:234–249.
Rockman MV. 2012. The qtn program and the alleles that matter for evolution: all that's gold does not glitter. Evolution. 66:1–17.
Rojas Echenique JI, Kryazhimskiy S, Nguyen Ba AN, Desai MM. 2019. Modular epistasis and the compensatory evolution of gene deletion mutants. PLOS Genetics. 15:1–23.
Romero Navarro JA, Willcox M, Burgueño J, Romay C, Swarts K, Trachsel S, Preciado E, Terron A, Delgado HV, Vidal V *et al*. 2017. A study of allelic diversity underlying flowering-time adaptation in maize landraces. Nature Genetics. 49:476–480.
Savolainen O, Lascoux M, Merilä J. 2013. Ecological genomics of local adaptation. Nature Reviews Genetics. 14:807–820.
Scarcelli N, Cheverud JM, Schaal BA, Kover PX. 2007. Antagonistic pleiotropic effects reduce the potential adaptive value of the FRIGIDA locus. Proceedings of the National Academy of Sciences. 104:16986–16991.
Silander OK, Tenaillon O, Chao L. 2007. Understanding the Evolutionary Fate of Finite Populations: The Dynamics of Mutational Effects. PLOS Biology. 5:e94.
Tenaillon M, Seddiki K, Mollion M, Le Guilloux M, Marchadier E, Ressayre A, Dillmann C. 2019. Transcriptomic response to divergent selection for flowering times reveals convergence and key players of the underlying gene regulatory network. Peer Community in Evolutionary Biology. .
Tenaillon O. 2014. The Utility of Fisher's Geometric Model in Evolutionary Genetics. Annual Review of Ecology, Evolution, and Systematics. 45:179–201.

Turelli M. 1984. Heritable genetic variation via mutation-selection balance: Lerch's zeta meets the abdominal bristle. Theoretical Population Biology. 25:138–193.

Vidal T, Andrieu B. 2020. Contrasting phenotypes emerging from stable rules: A model based on self-regulated control loops captures the dynamics of shoot extension in contrasting maize phenotypes. Annals of Botany. 126:615–633.

Walsh B, Lynch M. 2018. *Evolution and Selection of Quantitative Traits*. volume 1. Oxford University Press.

Weber KE, Diggins LT. 1990. Increased selection response in larger populations. II. Selection for ethanol vapor resistance in Drosophila melanogaster at two population sizes. Genetics. 125:585–597.

Wei M, Caballero A, Hill WG. 1996. Selection Response in Finite Populations. Genetics. 144:1961–1974.

Wisser RJ, Fang Z, Holland JB, Teixeira JEC, Dougherty J, Weldekidan T, de Leon N, Flint-Garcia S, Lauter N, Murray SC *et al*. 2019. The Genomic Basis for Short-Term Evolution of Environmental Adaptation in Maize. Genetics. 213:1479–1494.

Wray NR. 1990. Accounting for Mutation Effects in the Additive Genetic Variance-Covariance Matrix and Its Inverse. Biometrics. 46:177.

Zhu J, Andrieu B, Vos J, van der Werf W, Fournier C, Evers JB. 2014. Towards modelling the flexible timing of shoot development: Simulation of maize organogenesis based on coordination within and between phytomers. Annals of Botany. 114:753–762.

Supplementary material

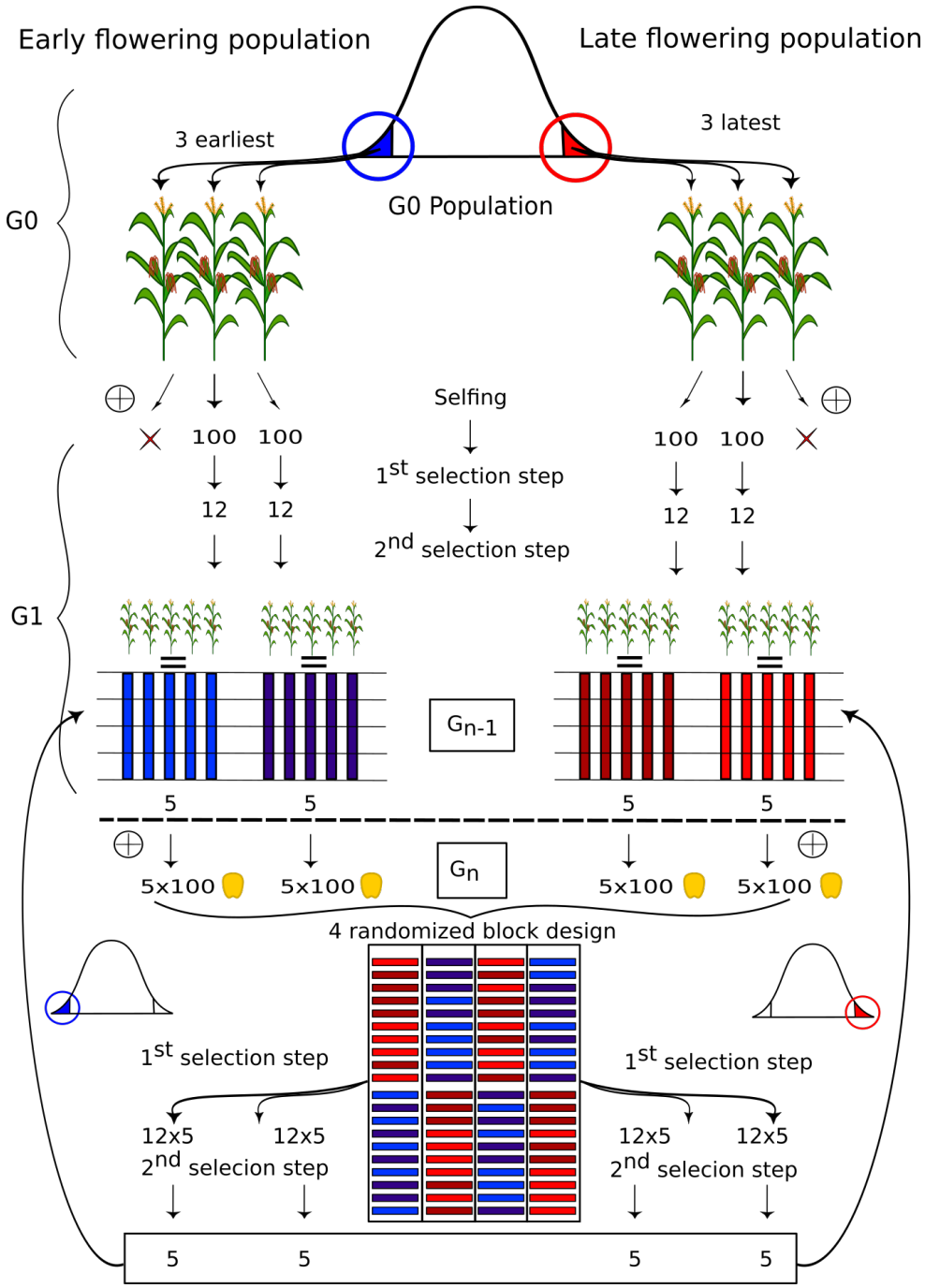

Figure S1 Experimental scheme of Saclay Divergent Selection Experiment for flowering time. For clarity a single scheme is shown but was replicated for the two DSEs. Starting from an inbred G0 population with little standing variation ($< 1\%$ residual heterozygosity (Durand *et al.* 2015)), the three earliest (resp. latest) flowering individuals represented in blue (resp. red) were chosen based on their offspring phenotypic values as the founders of two families forming the early (resp. late) population. For the subsequent generations, 10 (≈ 5 per family) extreme progenitors were selected in a two step selection scheme among 1000 plants. More specifically, 100 seeds per progenitor were evaluated in a four randomized-block design, *i.e.* 25 seeds per block in a single row. In a first selection step, the $3 \times 4 = 12$ earliest (resp. latest) flowering plants among the 100 plants per progenitor were selected in a first step. Then in a second selection step, 10 (≈ 5 per family) individuals were selected within each population based on both flowering time and kernel weight and the additional condition of preserving two progenitors per family from the previous generation.

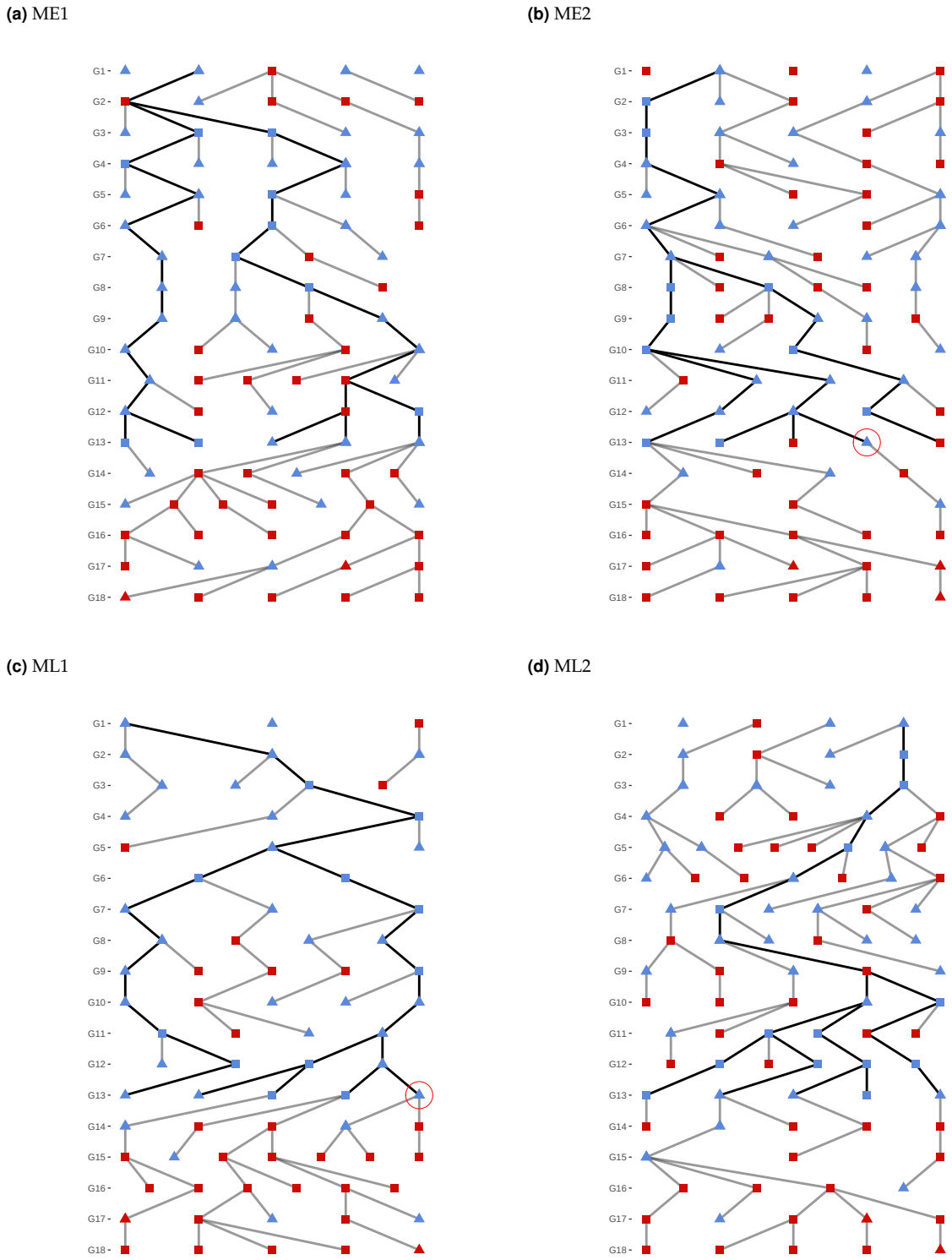

Figure S2 MBS family pedigrees from G1 to G18. The two early families ME1 (a) and ME2 (b), and the two late families ML1 (c) and ML2 (d) are presented. Each node corresponds to a progenitor selected at a given generation. Each edge indicates the relationship between a progenitor and its offspring. Individuals represented by a triangle were phenotyped in 2018 and 2019. Squares represent progenitors not included in the common gardens. Individuals represented in blue were genotyped with KASPar. The two G13 individuals circled in red in ME2 and ML1 were used for SNP detection. Thick black lines indicates the ancestral path of generation 13.

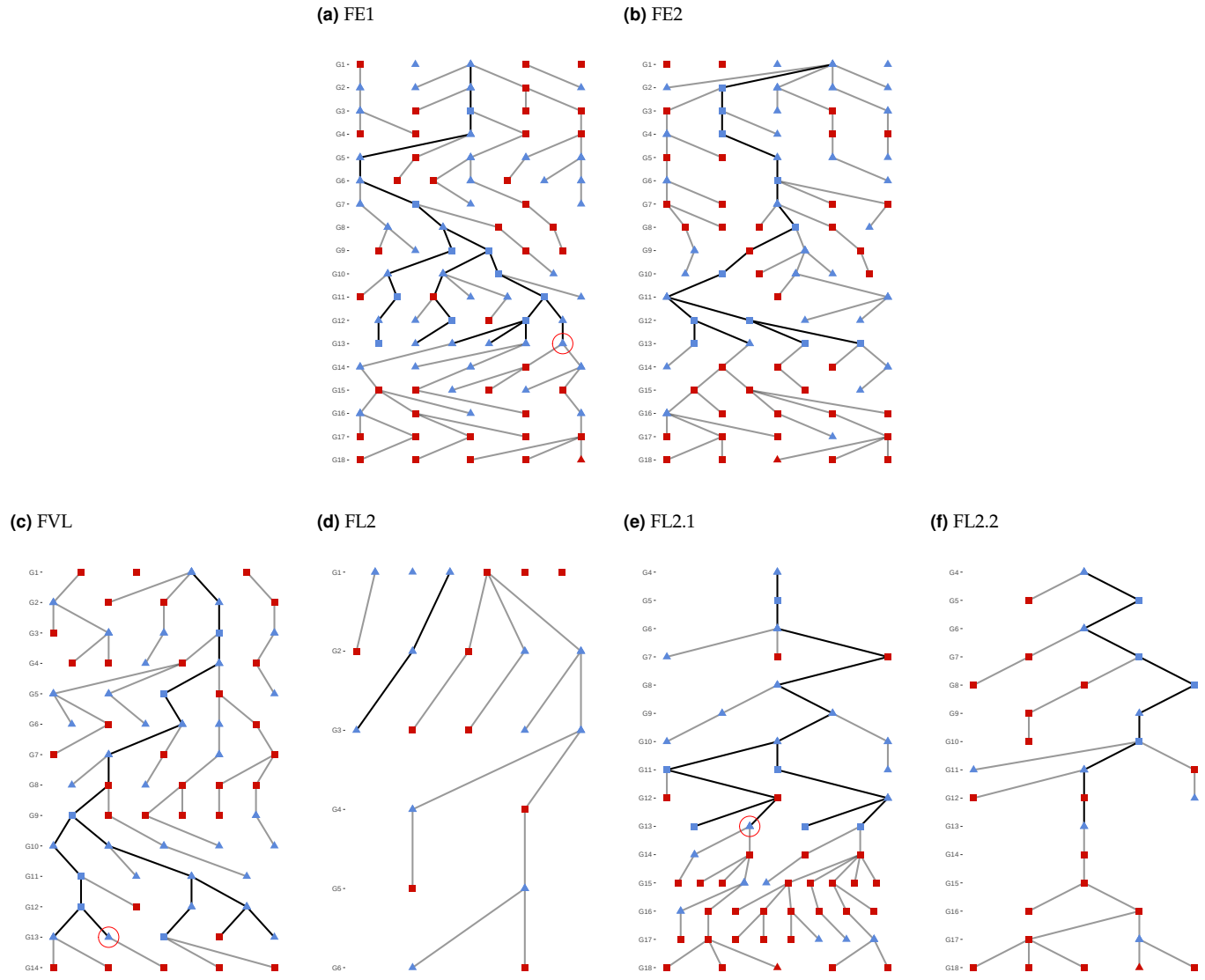

Figure S3 Graphical representation of F252 families pedigree relationship. Two early families FE1 (a), FE2 (b) together with one late family, FVL (c), are represented. FVL (c) could not be maintained after G14 (Durand *et al.* 2012). Both FL2.1 (d) and FL2.2 (e) were derived from a single individual from FL2 (f) at G3, after FVL was discarded. Each node corresponds to a progenitor selected at a given generation. Each edge corresponds to a filial relationship between a progenitor and its offspring. Individuals represented by a triangle were phenotyped in 2018 and 2019. Squares represent progenitors not included in the common gardens. Note that FVL individuals were phenotyped in common garden only in 2018. Individuals represented in blue were genotyped with KASPar. The three G13 individuals circled in red in FE1, FVL and FL2.1 were used for SNP detection. Thick black lines indicates the ancestral path of generation 13.

Table S1 Number of reads per genotype after trimming and filtering for low quality reads and rRNAs removal following the procedure described in Tenaillon *et al.* (2019).

Genotype	Number of libraries	Total number of pooled meristems	Number of filtered reads
MEE	6	150	92 504 789
MLL	5	178	59 399 604
FEE	4	100	93 216 514
FLL	5	146	96 708 953
FVL	3	56	66 890 125

Table S2 Distribution of detected SNPs and clusters of SNPs over the maize chromosomes for MBS (46) and F252 (7030)

Line	Chromosome	1	2	3	4	5	6	7	8	9	10
MBS	#SNPs	0	2	0	0	0	2	0	1	0	41
F252 [a]	#SNPs	895	37	465	61	179	1652	73	998	122	804
	# clusters	11	10	12	11	6	12	13	12	7	5

[a] For F252 clusters of SNPs were defined by k-means algorithm using euclidean distances between SNPs positions.

Table S3 MBS SNP distribution among categories of genes

Chrom	Gene_id	Annotation	M_Candidat	GWA_Candidat	ALONE	Sel	# SNPs
2	Zm00001d002125	nuclear RNA polymerase D2/E2	0	0	1	0	1
2	Zm00001d006409	RanBP2-type zinc finger protein	0	0	1	0	1
6	NA	NA	0	0	1	0	1
6	Zm00001d038104	Mannosyl-glycoprotein endo-beta-mannosidase	0	0	1	1	1
8	NA	NA	0	0	1	0	1
10	Zm00001d026084	IQ-domain 23	0	0	0	1	2
10	Zm00001d026088	Outer cell layer2	0	0	0	1	14
10	Zm00001d026089	Replication factor C subunit 2	0	0	0	0	11
10	Zm00001d026091	E3 ubiquitin-protein ligase	0	0	0	0	9
10	Zm00001d026094	Heat stress transcription factor B-2b	0	0	0	0	5

Table S4 F252 480 sampled SNPs distribution among chromosomes

Chromosome	1	2	3	4	5	6	7	8	9	10
# of SNPs	91	10	55	4	24	131	4	82	12	67

1

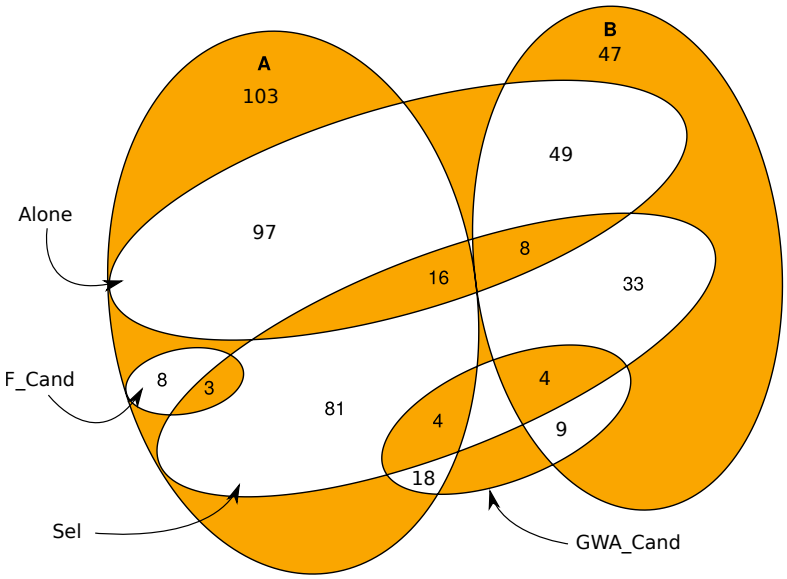

Figure S4 Genotyped SNPs distribution among categories in F252. Categories "F_Candidate", "GWA_Candidate", "Sel" correspond to the one defined in Tenaillon *et al.* (2019) such that: "F_Candidate" corresponds to SNPs in known flowering time genes in maize, "GWA_Candidate" corresponds to SNPs in genes associated to flowering time variation in a panel of 4,471 inbred lines/landraces (Romero Navarro *et al.* 2017), "Sel" corresponds to SNPs in genes detected as differently expressed between Early and Late G13 progenitors in the RNA-Seq. "Alone" were SNPs found isolated in 20kb regions, and Group A corresponds to SNPs differing between FE1 and {FVL and FL2.1} while Group B corresponds to SNPs differing between {FE1 and FVL} and FL2.1.

1

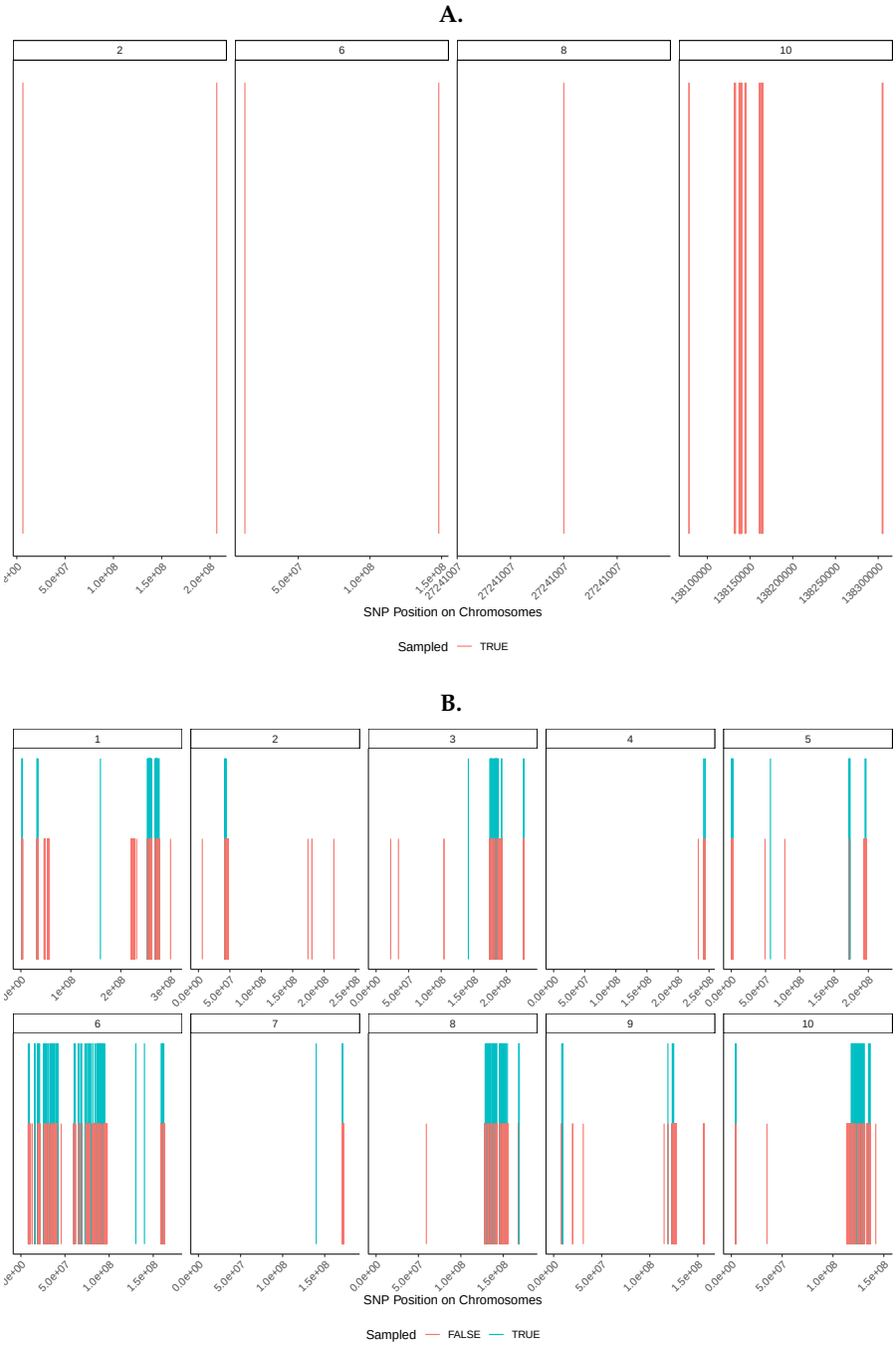

Figure S5 Genomic positions of the detected SNPs A. Each bar represent the position of a SNP. For MBS, all 46 SNPs were sampled for KASPar™ genotyping. **B.** For F252, 480 SNPs (in blue) were sampled among the 7,030 detected.

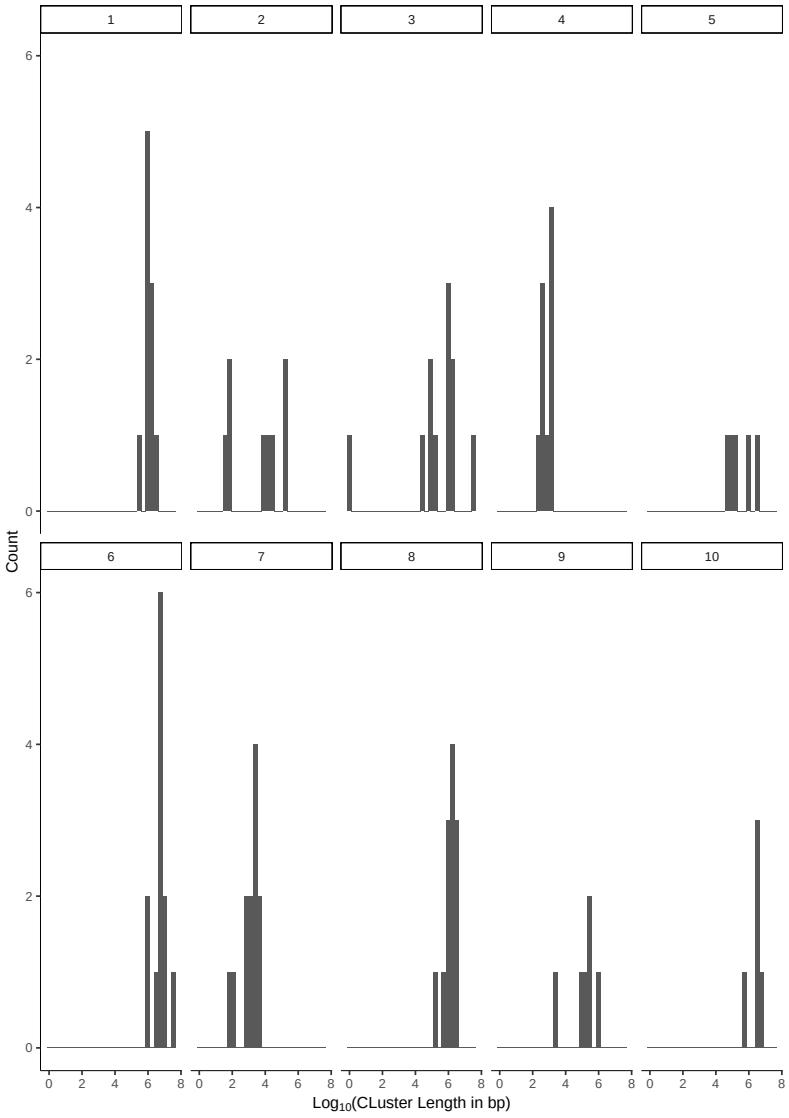

Figure S6 Distribution of the cluster length ($log_{10}(\#bp)$) per Chromosome in F252 after k-means clustering.

Appendix 1. Inferring genotypes from sparse KASPar™ genotyping data and pedigree relationships.

We produced a sparsed genotyping matrix using KASPar™ genotyping, so that genotypic information was available only for a subset of all progenitors. From this subset we aimed at inferring all genotypes of the genealogy until generation 18th.

In order to do so, we developed a likelihood model, and used a parsimony algorithm developped by Durand *et al.* (2015) to infer missing data in the matrix of genotypes with the highest likelihood at every given SNP. Below we describe the likelihood function that calculates for a given locus, the probability of each genotype given the SNP genotypes of other individuals. This function considers (i) the genealogical information, (ii) the generations of selfing, (iii) the experimental error associated with KASPar genotyping.

Heredity

Let $X_{g,i} \in \{0,1,2\}$ be the random variable associated to the true genotype of individual i at generation g at a SNP biallelic locus. $X_{g,i}$ can be associated to a probability law :

$$\vec{\pi}(X_{g,i}) = \Big\{P(X_{g,i}=0), P(X_{g,i}=1), P(X_{g,i}=2)\Big\}'$$

Conditionally to the parent $\mathcal{A}_{g,i}$, we have, for any realization $x_o \in \{0,1,2\}$:

$$P(X_{g,i}=x_o) = \sum_{x_a \in \{0,1,2\}} P\left(X_{g,i}=x_o / X_{g-1,\mathcal{A}_{g,i}}=x_a\right) \cdot P\left(X_{g-1,\mathcal{A}_{g,i}}=x_a\right) \tag{12}$$

Individuals are reproducing through selfing every generation.
We supposed that mutations occured during meiosis at a rate μ per locus, per individual, per generation with equal probability of: $A \to a$ or $a \to A$.
Selection occurred among the adult progenies, and we considered an additive fitness effect for allele a, such that: $w_0 = 1$, $w_1 = 1+s$ and $w_2 = 1+2s$.

Hence, the frequency of selected genotypes x_o among the progenies of parent x_a is:

$$p_{x_o/x_a} = \frac{f(x_o/x_a)w_{x_o}}{\sum_{x_k \in \{0,1,2\}} f(x_k/x_a)w_{x_k}}$$

where $f(x_k/x_a)$ is given by Mendelian inheritance taking into account selfing and mutations. We established the (3×3) matrix T of probabilities of $X_{g,i}$ given $X_{g-1,\mathcal{A}_{g,i}}$ as indicated in the table below:

	Parent		
Offspring	0 (AA)	1 (Aa)	2 (aa)
0 (AA)	$\frac{(1-\mu)^2}{1+2s\mu}$	$\frac{1}{4+4s}$	$\frac{\mu^2}{1+2s(1-\mu)}$
1 (Aa)	$\frac{2\mu(1-\mu)(1+s)}{1+2s\mu}$	$\frac{1}{2}$	$\frac{2\mu(1-\mu)(1+s)}{1+2s(1-\mu)}$
2 (aa)	$\frac{\mu^2(1+2s)}{1+2s\mu}$	$\frac{1+2s}{4+4s}$	$\frac{(1-\mu)^2(1+2s)}{1+2s(1-\mu)}$

so that,

$$P\left(X_{g,i}=x_o / X_{g-1,\mathcal{A}_{g,i}}=x_a\right) = T[x_o, x_a] \tag{13}$$

Using (12) and the T matrix,we have:

$$\vec{\pi}(X_{g,i}) = T \cdot \vec{\pi}(X_{g-1,\mathcal{A}_{g,i}}) \tag{14}$$

Modeling SNP genotype

Let $Y^{Obs}_{g,i} \in \{0,1,2\}$ be the random variable associated to the observed SNP genotype of individual i at generation g. Because of both bulk genotyping and experimental errors, the SNP phenotype does not translate directly into the genotype. Let $Y^{Bulk}_{g,i} \in \{0,1,2\}$ be the random variable associated to the true SNP genotype after bulk sampling, but before KASPar errors.

Bulk genotyping For genotyping, each individual S_0 of the genealogy has been selfed once to produce 25 S_1 individuals, also selfed with seeds (S_2) collected in bulk. We used DNAs from 15 S_2 plants to infer the genotype of the S_0 individual. This procedure may lead to ascertainment bias that occurs with a probability p_b. For instance, 15 S_2 plants generated from a S_0 heterozygote may by chance be homozygotes for the a allele. This may occur with a probability 0.5 at each generation of selfing (0.25 in S_2). Let

$$1 - p_b = P\left(Y^{Bulk}_{g,i} = 1 / X_{g,i} = 1\right) \tag{15}$$

In the bulk of 15 S_2 plants, we have $p_b < 0.02$. Because we performed many independent bulks, we modeled p_b as a random variable following an exponential distribution of parameter $\lambda_b = 1/0.02 = 50$.

We established (3×3) matrix T^{Bulk} of probabilities of $Y^{Bulk}_{g,i}$ given $X_{g,i}$ as indicated in the table below:

	$X_{g,i} =$		
$Y_{g,i}^{Bulk} =$	0 (AA)	1 (Aa)	2 (aa)
0 (AA)	1	$\frac{p_b}{2}$	0
1 (Aa)	0	$1 - p_b$	0
2 (aa)	0	$\frac{pb}{2}$	1

Accounting for experimental errors in KASPar genotyping Experimental biases and misinterpretation of the fluorescence data may occur if:

- homozygous genotypes are widespread on the two-dimensional fluorescence plan. This may occur either because of the differential/variance around the fluorescence signal between the two allele-specific fluorophores,
- or because of the bulk DNAs and variation of allele counts which may translate into a continuum between homozygotes and heterozygotes.

Let e be the probability of misinterpretation of one allele of a biallelic SNP genotype. We can establish (3×3) matrix T^{Kasp} of probabilities of $Y_{g,i}^{Obs}$ given $Y_{g,i}^{Bulk}$ as indicated in the table below:

	$Y_{g,i}^{Bulk} =$		
$Y_{g,i}^{Obs} =$	0 (AA)	1 (Aa)	2 (aa)
0 (AA)	$(1-e)^2$	$e(1-e)$	e^2
1 (Aa)	$2e(1-e)$	$e^2 + (1-e)^2$	$2e(1-e)$
2 (aa)	e^2	$e(1-e)$	$(1-e)^2$

Hence, we have $P\left(Y_{g,i}^{Obs} \neq Y_{g,i}^{Bulk}\right) = \frac{6e(1-e)+e^2}{3} = \frac{6e-4e^2}{3}$.

From SNP phenotypes to SNP genotypes Considering all possible sources of error (bulk genotyping and experimental biases), we have :
$P\left(Y_{g,i}^{Obs}/X_{g,i}\right) = P\left(Y_{g,i}^{Obs}/Y_{g,i}^{Bulk}\right) \times P\left(Y_{g,i}^{Bulk}/X_{g,i}\right)$, whose corresponding transition matrix is given by the product $T^{Kasp} \cdot T^{Bulk}$, which can be written:

	$X_{g,i} =$		
$Y_{g,i}^{Obs} =$	0 (AA)	1 (Aa)	2 (aa)
0 (AA)	$(1-e)^2$	$2e^2p_b - e^2 - 2ep_b + e + 1/2p_b$	e^2
1 (Aa)	$2e(1-e)$	$-4e^2p_b + 2e^2 + 4ep_b - 2e - p_b + 1$	$2e(1-e)$
2 (aa)	e^2	$2e^2p - e^2 - 2ep_b + e + p_b/2$	$(1-e)^2$

Hence, we have :

$$\begin{aligned} P\left(Y_{g,i}^{Obs} \neq X_{g,i}\right) &= 1/3[2e(1-e) + e^2 + \\ &\quad 2e^2p_b - e^2 - 2ep_b + e + 1/2p_b + 2e^2p - e^2 - 2ep_b + e + p_b/2 + \\ &\quad e^2 + 2e(1-e)] \\ &= 1/3[4e^2p_b - 4e^2 - 4ep_b + 6e + p_b] \end{aligned}$$

Likelihood function of genotypes

We have described above how to estimate the probability of a phenotype knowing the genotype of the individual and also how to calculate a vector of probability of the 3 genotypes knowing the genotype of its parent. From there we were able to estimate the likelihood of a genotype of the genealogy knowing its SNP phenotype and its parent.

The parameters of the model are:

- $\theta_{hered} = (\mu, s)$ that relates to heredity.
- $\theta_{exp} = (p_b, e)$ that relates to the experiment.

The known information is $\mathcal{A}_{g,i}$ the parent of each individual of the genealogy. The random variables are $Y_{g,i}^{Obs}$ and $X_{g,i}$. Using conditional probabilities, we have

$$P\left(X_{g,i}/Y_{g,i}^{Obs},\theta_{exp},\theta_{hered},X_{g-1,\mathcal{A}_{g,i}}\right)=\frac{P\left(X_{g,i},Y_{g,i}^{Obs},\theta_{exp},\theta_{hered},X_{g-1,\mathcal{A}_{g,i}}\right)}{P\left(Y_{g,i}^{Obs},\theta_{exp},\theta_{hered},X_{g-1,\mathcal{A}_{g,i}}\right)} \tag{16}$$

Because the SNP phenotype knowing the genotype does not depend on the parental genotype, and because θ_{hered} and $X_{g-1,\mathcal{A}_{g,i}}$ are independent, we have

$$\begin{aligned}
&P\left(X_{g,i},Y_{g,i}^{Obs},\theta_{exp},\theta_{hered},X_{g-1,\mathcal{A}_{g,i}}\right)\\
&=P\left(Y_{g,i}^{Obs},\theta_{exp}/X_{g,i}\right)\cdot P\left(X_{g,i}/\theta_{hered},X_{g-1,\mathcal{A}_{g,i}}\right)\cdot P\left(\theta_{hered}\right)P\left(X_{g-1,\mathcal{A}_{g,i}}\right)\\
&=P\left(Y_{g,i}^{Obs}/\theta_{exp},X_{g,i}\right)\cdot P\left(X_{g,i}/\theta_{hered},X_{g-1,\mathcal{A}_{g,i}}\right)\cdot P\left(\theta_{exp}\right)\cdot P\left(\theta_{hered}\right)\cdot P\left(X_{g-1,\mathcal{A}_{g,i}}\right)
\end{aligned}$$

Similarly, the denominator of (16) can be written:

$$\begin{aligned}
&P\left(Y_{g,i}^{Obs},\theta_{exp},\theta_{hered},X_{g-1,\mathcal{A}_{g,i}}\right)\\
&=P\left(Y_{g,i}^{Obs}/\theta_{exp},\theta_{hered},X_{g-1,\mathcal{A}_{g,i}}\right)\cdot P\left(\theta_{exp}\right)\cdot P\left(\theta_{hered}\right)\cdot P\left(X_{g-1,\mathcal{A}_{g,i}}\right)\\
&=P\left(\theta_{exp}\right)\cdot P\left(\theta_{hered}\right)\cdot P\left(X_{g-1,\mathcal{A}_{g,i}}\right)\cdot\\
&\qquad\textstyle\sum_{x_o\in\{0,1,2\}}P\left(Y_{g,i}^{Obs}/X_{g,i}=x_o,\theta_{exp}\right)\cdot P\left(X_{g,i}=x_o/\theta_{hered},X_{g-1,\mathcal{A}_{g,i}}\right)
\end{aligned}$$

Therefore, we have,

$$P\left(X_{g,i}/Y_{g,i}^{Obs},\theta_{exp},\theta_{hered},\mathcal{A}_{g,i}\right)=\frac{P\left(Y_{g,i}^{Obs}/X_{g,i},\theta_{exp}\right)\cdot P\left(X_{g,i}/\theta_{hered},X_{g-1,\mathcal{A}_{g,i}}\right)}{\sum_{x_o}P\left(Y_{g,i}^{Obs}/X_{g,i}=x_o,\theta_{exp}\right)\cdot P\left(X_{g,i}=x_o/\theta_{hered},X_{g-1,\mathcal{A}_{g,i}}\right)} \tag{17}$$

Equation (17) can be computed using the models described above. Furthermore, knowing the parent of each individual of the genealogy, conditional probabilities in (17) do not use any extra information and they are independent. Therefore, we extended this equation to all individuals of a given family in order to capture the genealogical information contained in related individuals. The family is characterized by a combination of genotypes whose likelihood is the product of the likelihood of each individual genotype

$$\mathcal{L}=\prod_{g,i}P\left(X_{g,i}/Y_{g,i}^{Obs},\theta,\mathcal{A}_{g,i}\right) \tag{18}$$

Inference algorithm description

To perform the inference of missing genotypes we used the algorithm developed by Durand *et al.* (2015).

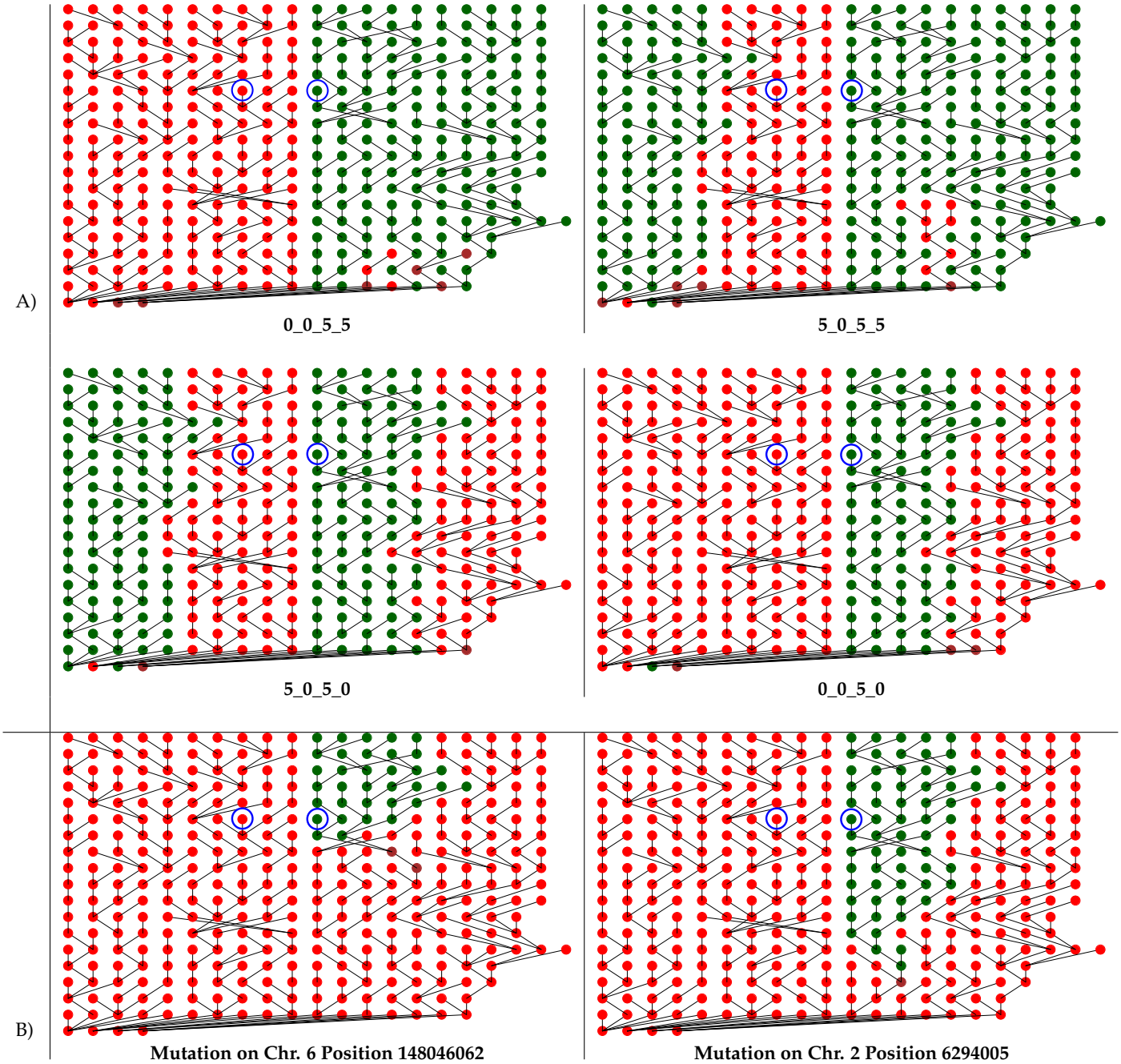

Figure S7 Example of the main genealogical structure cases in MBS for A) Standing variation and B) the two detected *de novo* mutations. In MBS, we expected under pure drift 4 main different cases for standing variants after conditioning on the SNP detection at generation 13. If we count the number of genotype AA in family ME1, N^{AA}_{ME1}, for example, respectively N^{AA}_{ME2}, N^{AA}_{ML1} and N^{AA}_{ML2}, the 4 main cases (neglecting unfixed alleles within family) are:

- $N^{AA}_{ME1} = 0$, $N^{AA}_{ME2} = 0$, $N^{AA}_{ML1} = 5$, $N^{AA}_{ML2} = 5$, subsequently called 0_0_5_5
- $N^{AA}_{ME1} = 5$, $N^{AA}_{ME2} = 0$, $N^{AA}_{ML1} = 5$, $N^{AA}_{ML2} = 5$, subsequently called 5_0_5_5
- $N^{AA}_{ME1} = 5$, $N^{AA}_{ME2} = 0$, $N^{AA}_{ML1} = 5$, $N^{AA}_{ML2} = 0$, subsequently called 5_0_5_0
- $N^{AA}_{ME1} = 0$, $N^{AA}_{ME2} = 0$, $N^{AA}_{ML1} = 5$, $N^{AA}_{ML2} = 0$, subsequently called 0_0_5_0

Example of simulated genealogies corresponding to these 4 cases, plus two simulated genealogies corresponding to *de novo* mutations are presented. Note that in MBS these 4 cases encompassed over 99.9% of the simulations for standing variation and the early occurring mutation 2_6294005 (at G_3). G_{18} is at the top of each genealogy and G_0 at the bottom, each individual is represented by a dot, whose color indicates the genotype (in red *aa*, in green AA and in brown *Aa*). Each line represents a kinship relationship. At G_{18} (top), each group of 5 individual belongs to one family, in order: ME1_ME2_ML1_ML2. Blue circles identify the G_{13} progenitors used for SNPs detection.

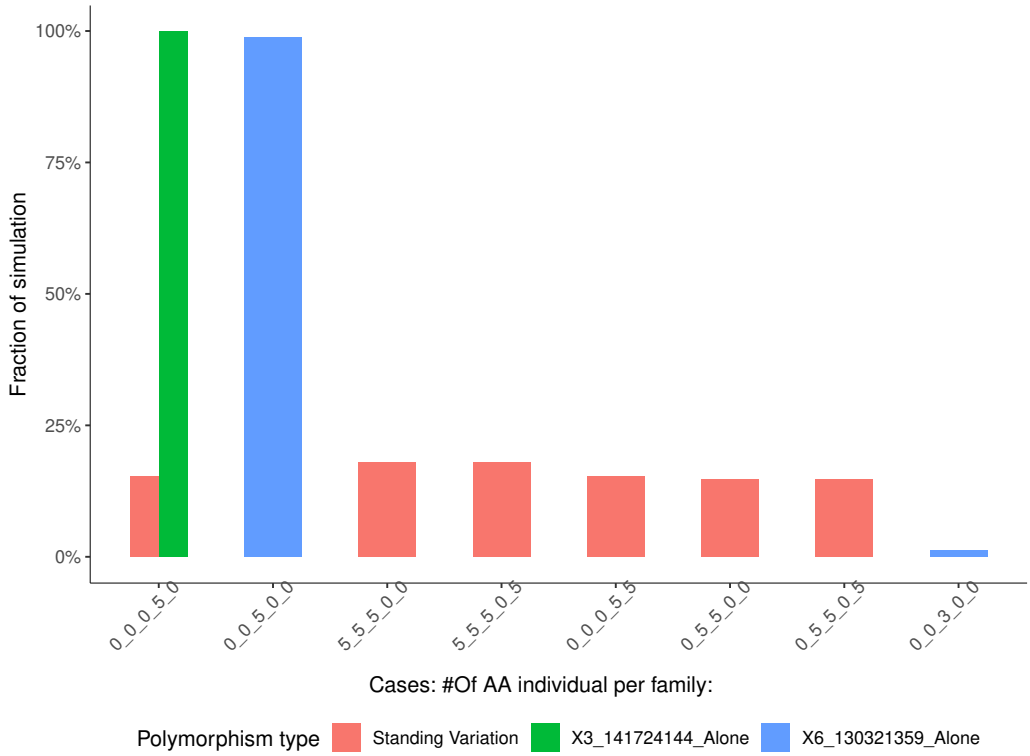

A)

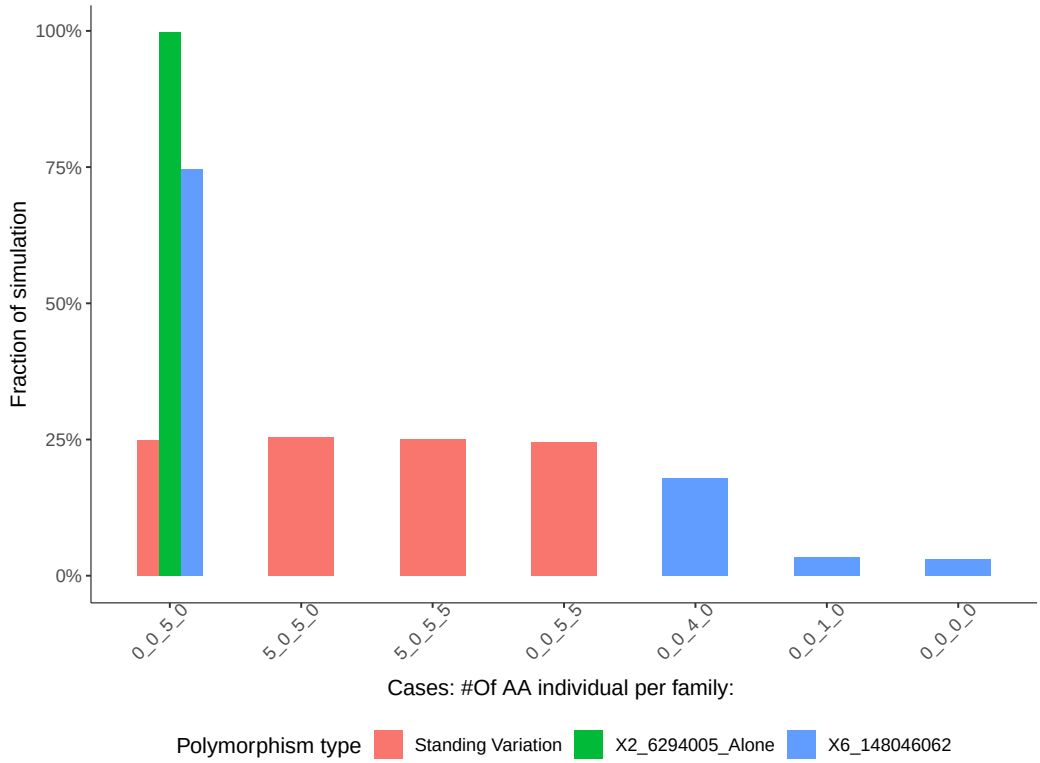

B)

Figure S8 Frequency distribution of simulated genealogical structures of segregating polymorphisms in A) F252, and B) MBS. Cases are summarized by AA counts in FVL_FL2.1_FL2.2_FE1_FE2 for F252 and ME1_ME2_ML1_ML2 in MBS. For F252, the typology of possible cases for standing variants is composed of 6 main cases represented in red— each over 8% of the simulations—representing 97% of the possibilities. In MBS, the typology of possible cases for standing variants is composed of 4 main cases represented in red encompassing 99.9% of the simulations. In both cases, unrepresented cases (3% of the simulations in F252 and 0.01% of the simulations in MBS) corresponded to cases were standing variants were not fixed at generation G_{18}. Green and blue bars corresponds to the two mutations detected in each backgrounds for the corresponding cases.

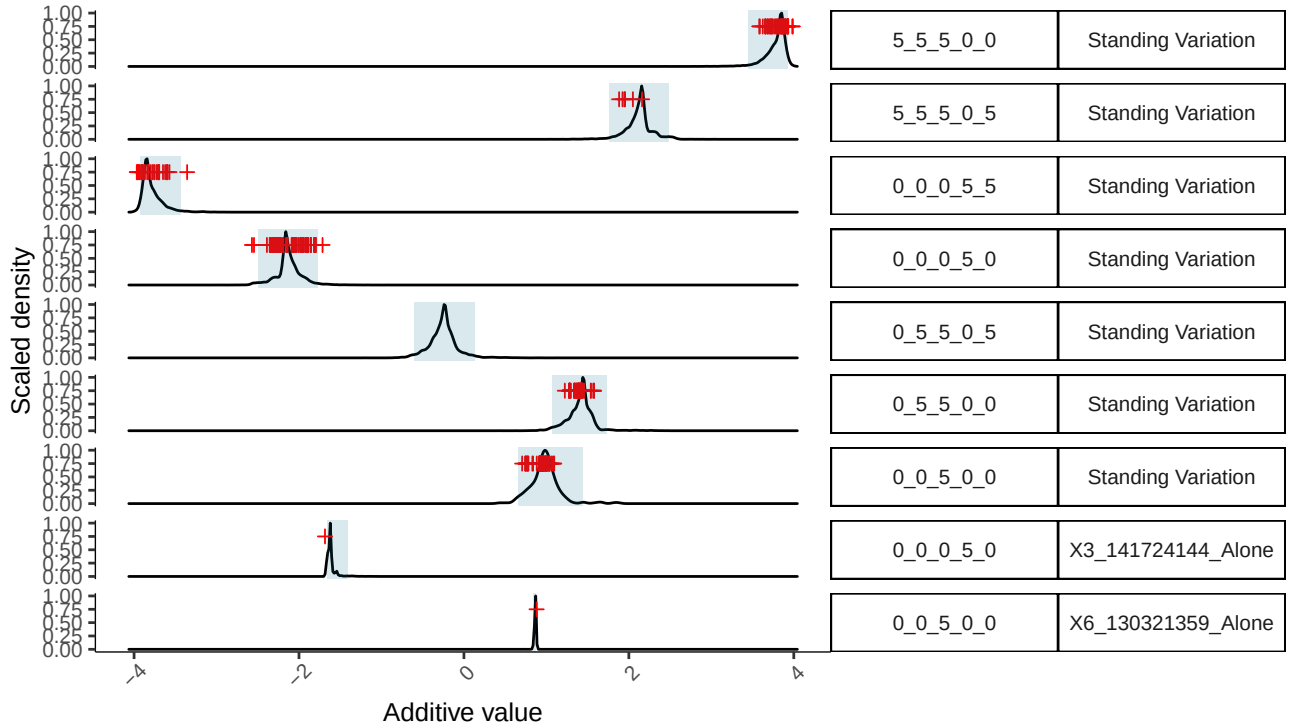

A)

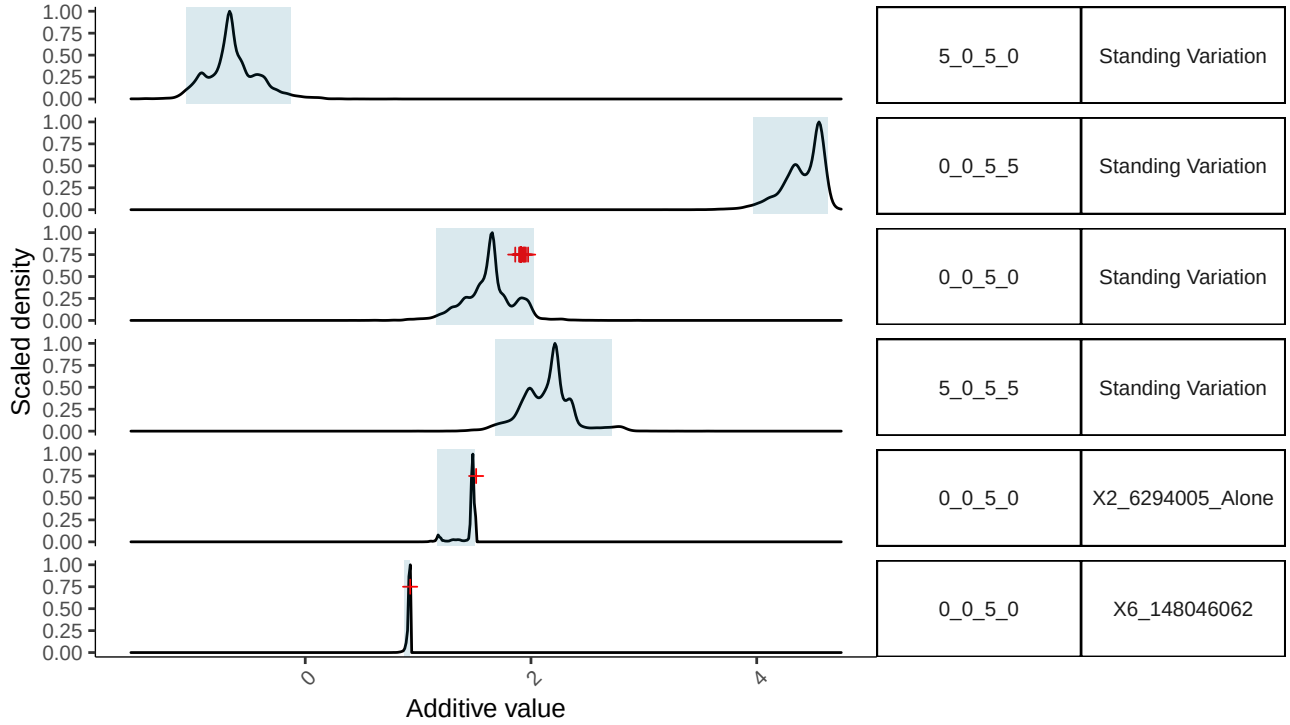

B)

Figure S9 Distribution of simulated and observed (red crosses) a **values for flowering time (DSEYM) according to the main genealogy at** G_{18} **defined Fig. S8** in A) F252, and B) MBS. Shaded areas cover 95% of the corresponding distribution.

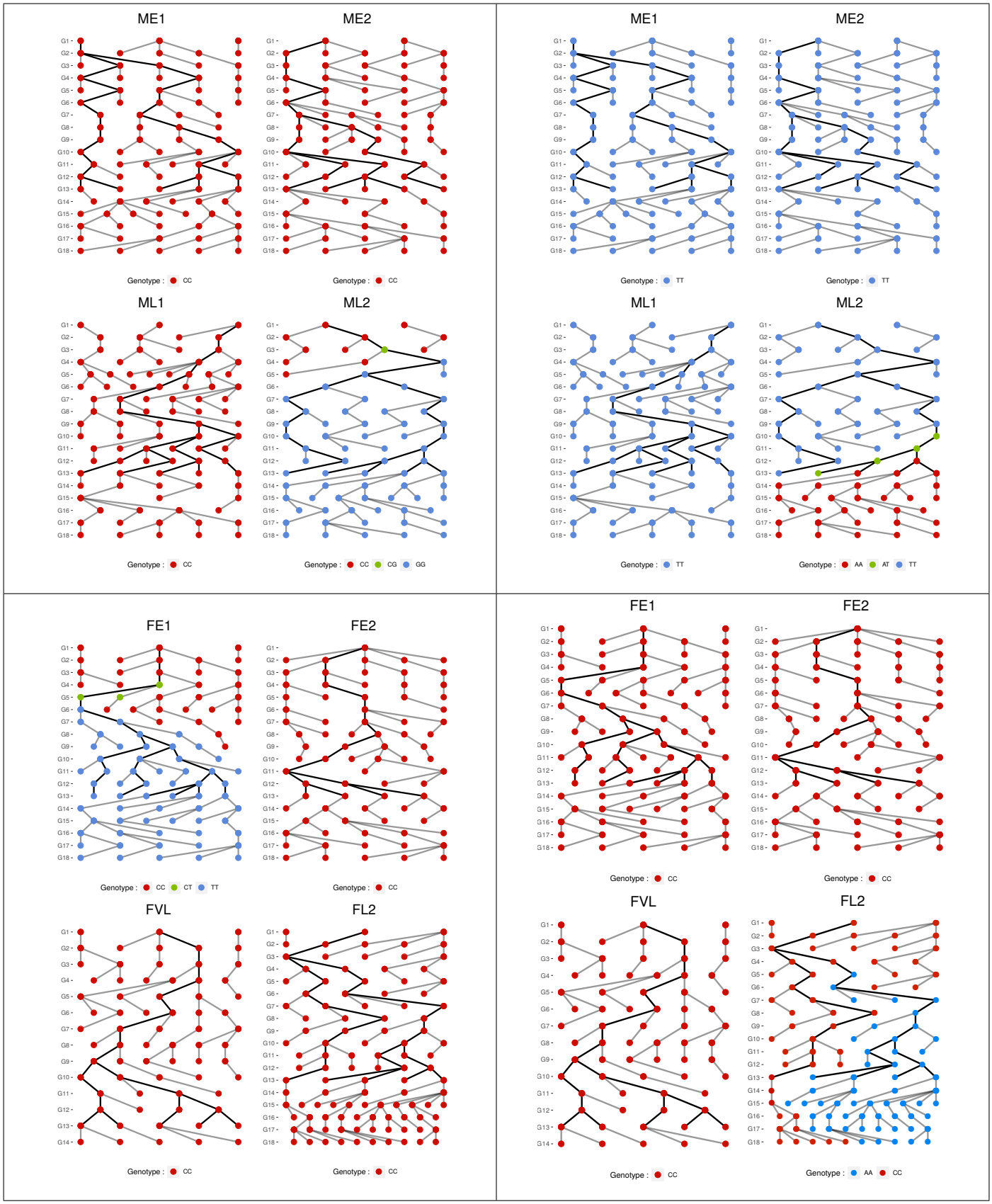

Figure S10 ***De novo*** **mutation dynamics through generations within MBS and F252 families** Colors indicate the genotypes of the 4 detected mutations along the pedigrees. From top-left panels to bottom-right pannels, mutations were located on Ch.2, postion 6294005 and Ch.6 position 148046062 for MBS, and on Ch.3 position 141724144 and Ch.6 position 130321359 for F252.

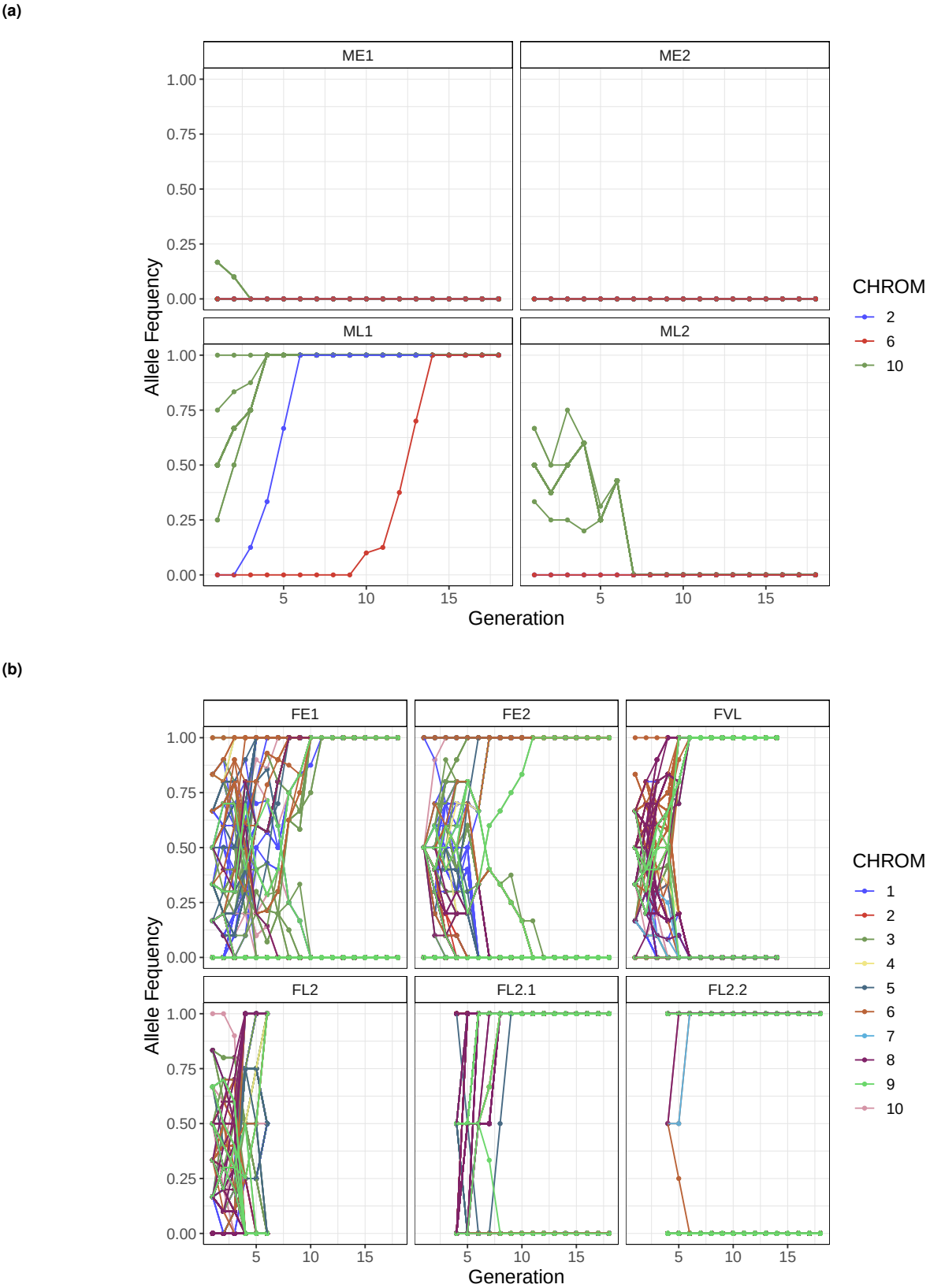

Figure S11 Within-family allele frequency dynamics through generations in MBS (a) and F252 (b). Evolution of minor allele frequency is presented. SNPs are colored according to chromosomes. Observed noise around allele frequency of 0 or 1 is caused by imperfect inferences of the algorithm. Note that three SNPs in FE2, FL2.1 and FL2.2 respectively, displayed intermediate frequencies. The original KASPar fluorescence data of these particular SNPs were difficult to interpret.

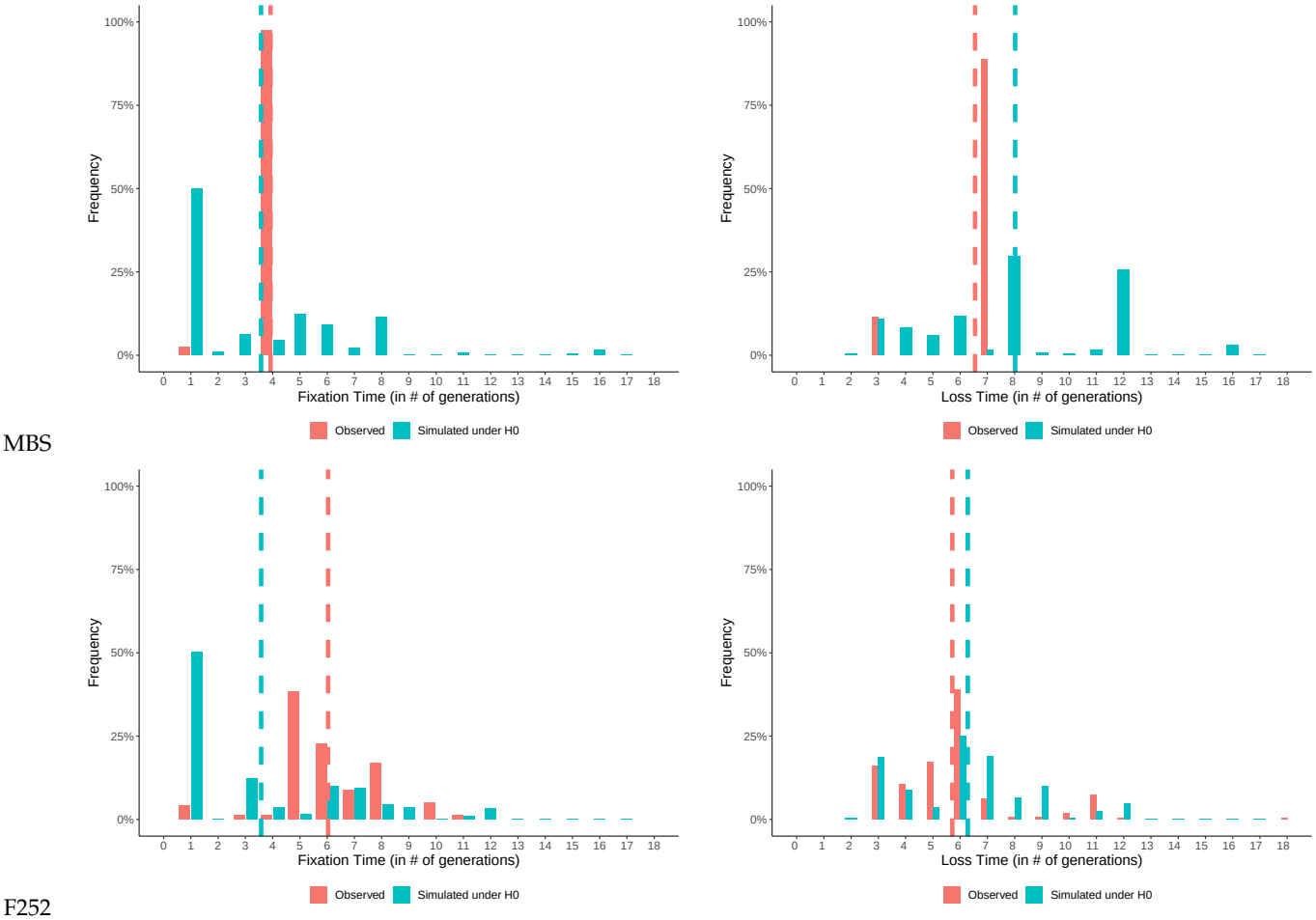

Figure S12 Distribution of standing variants fixation times (left panels) and time-to-loss (right panels) in MBS and F252 from observed (red) and simulated allele trajectories (blue). Dashed vertical lines highlight average fixation (resp. loss) times.

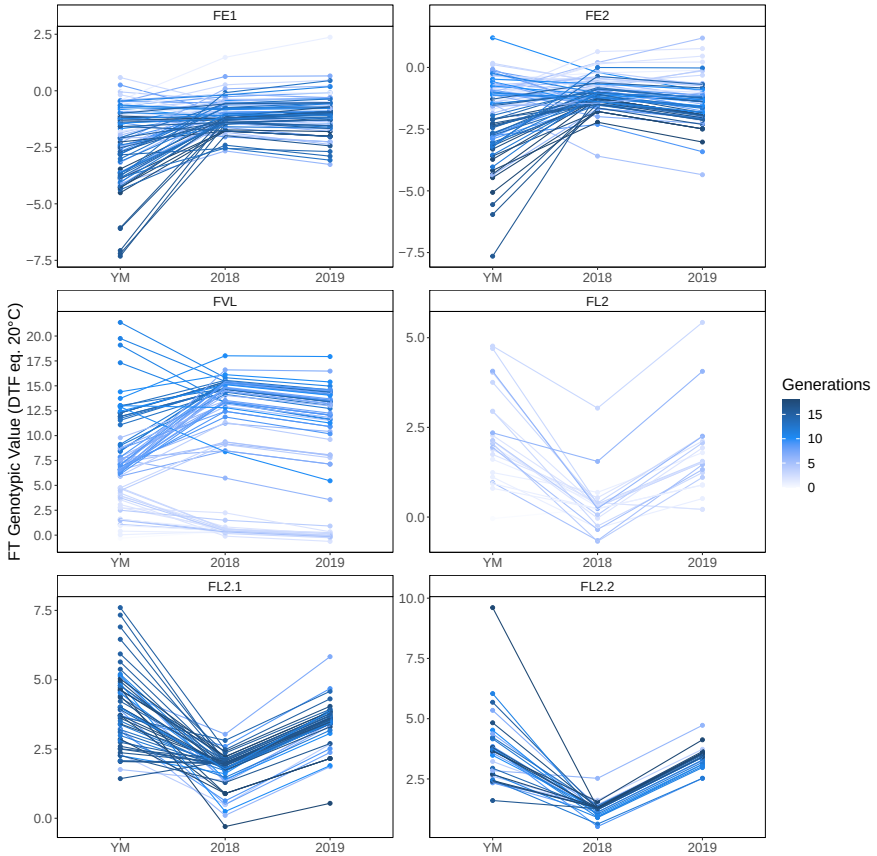

A)

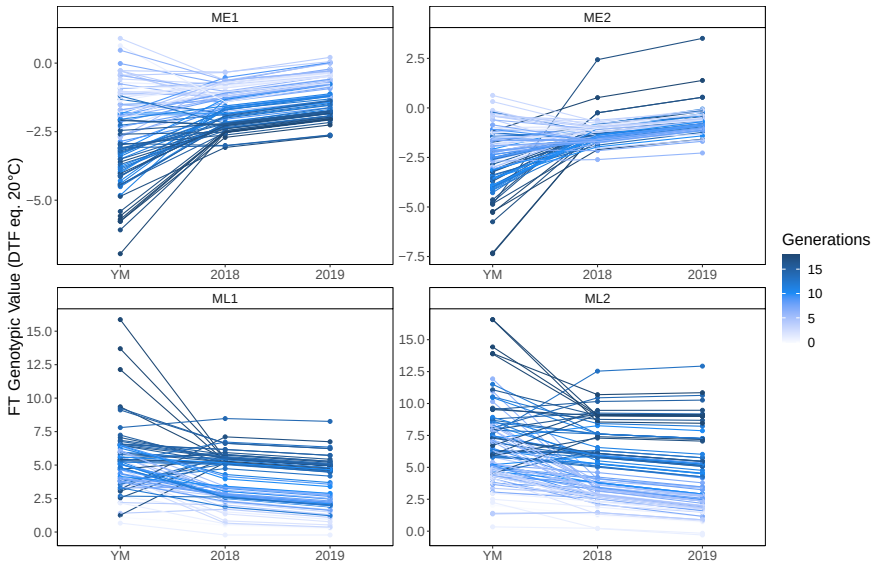

B)

Figure S13 Flowering time reaction norms per family from predicted genetic values in each environment type in A) F252 and B) MBS. Each dot per evaluation year represents a progenitor predicted genotypic value. Straight lines link progenitor values from yearly measurement, 2018 and 2019 on a given progenitor.

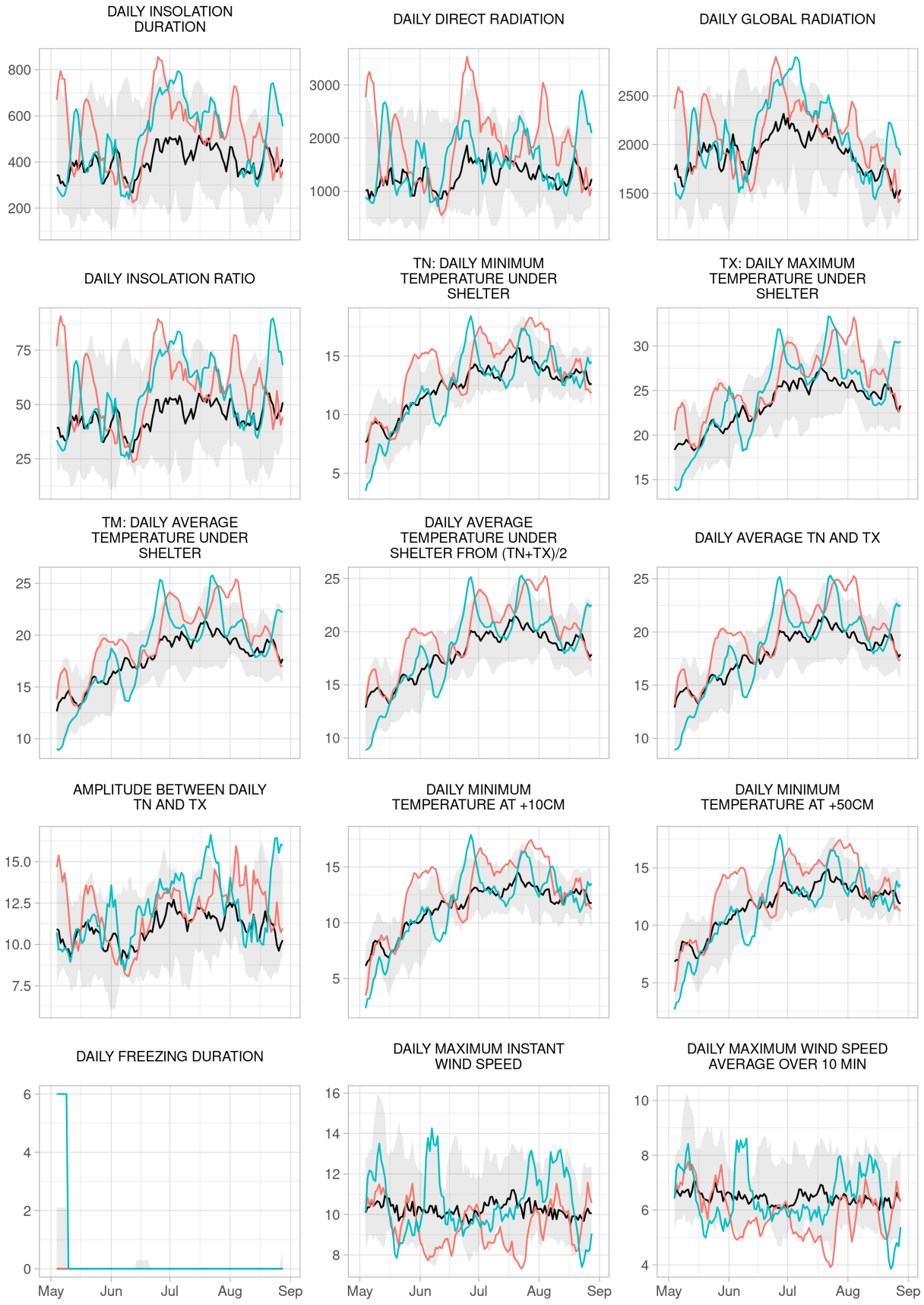

Figure S14 Evolution over the growing season of environmental variables recorded between 2006 and 2019 averaged over a 7-days sliding window. Red (blue) curves correspond to measured values in 2018 (2019). Black curves indicate the evolution along time of the median values over the recorded time period and grey areas include values between 5th and 95th percentiles.

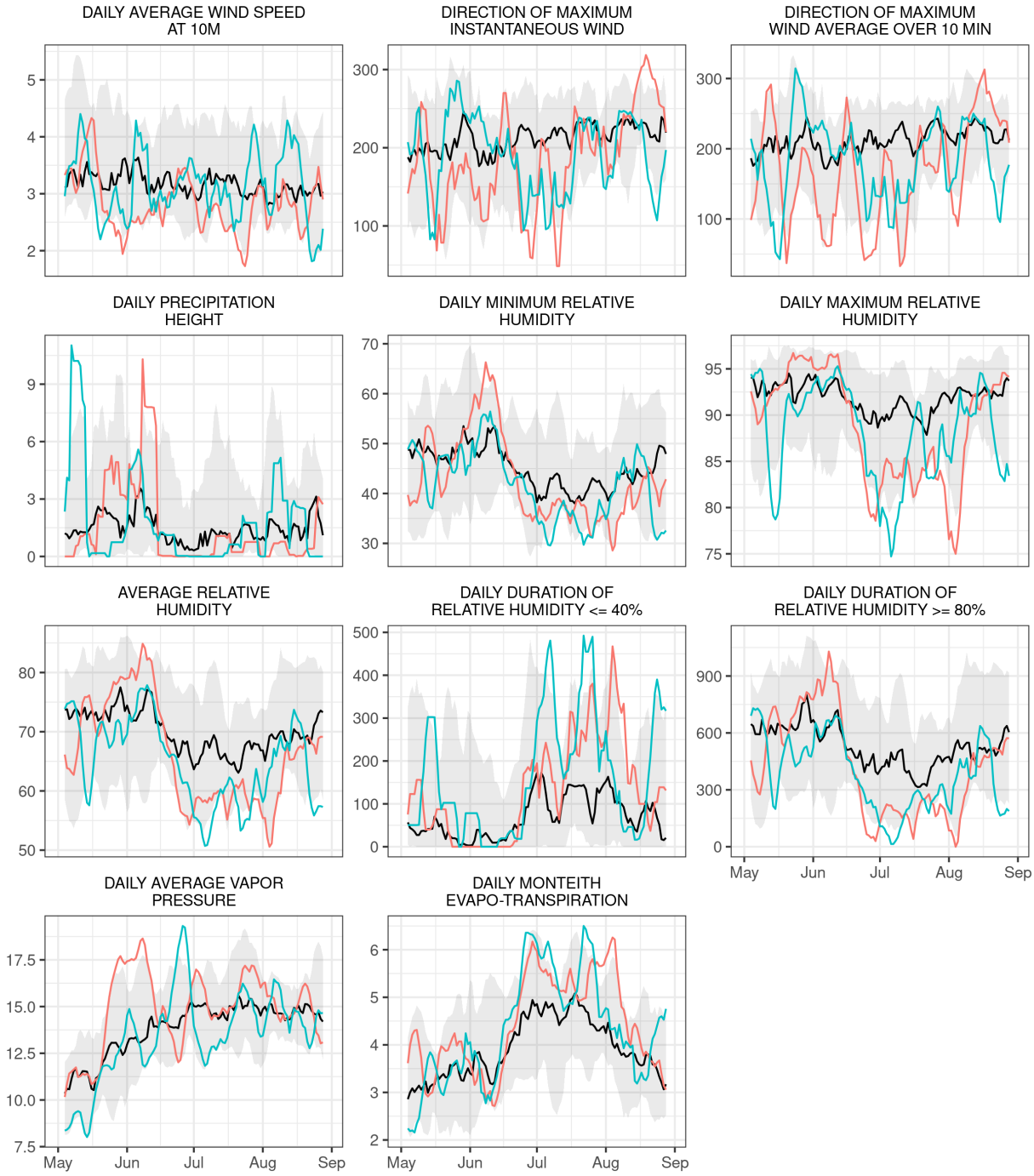

Figure S14 (Continued) Evolution over the growing season of environmental variables recorded between 2006 and 2019 averaged over a 7-days sliding window. Red (blue) curves correspond to measured values in 2018 (2019). Black curves indicate the evolution along time of the median values over the recorded time period and grey areas include values between 5th and 95th percentiles.

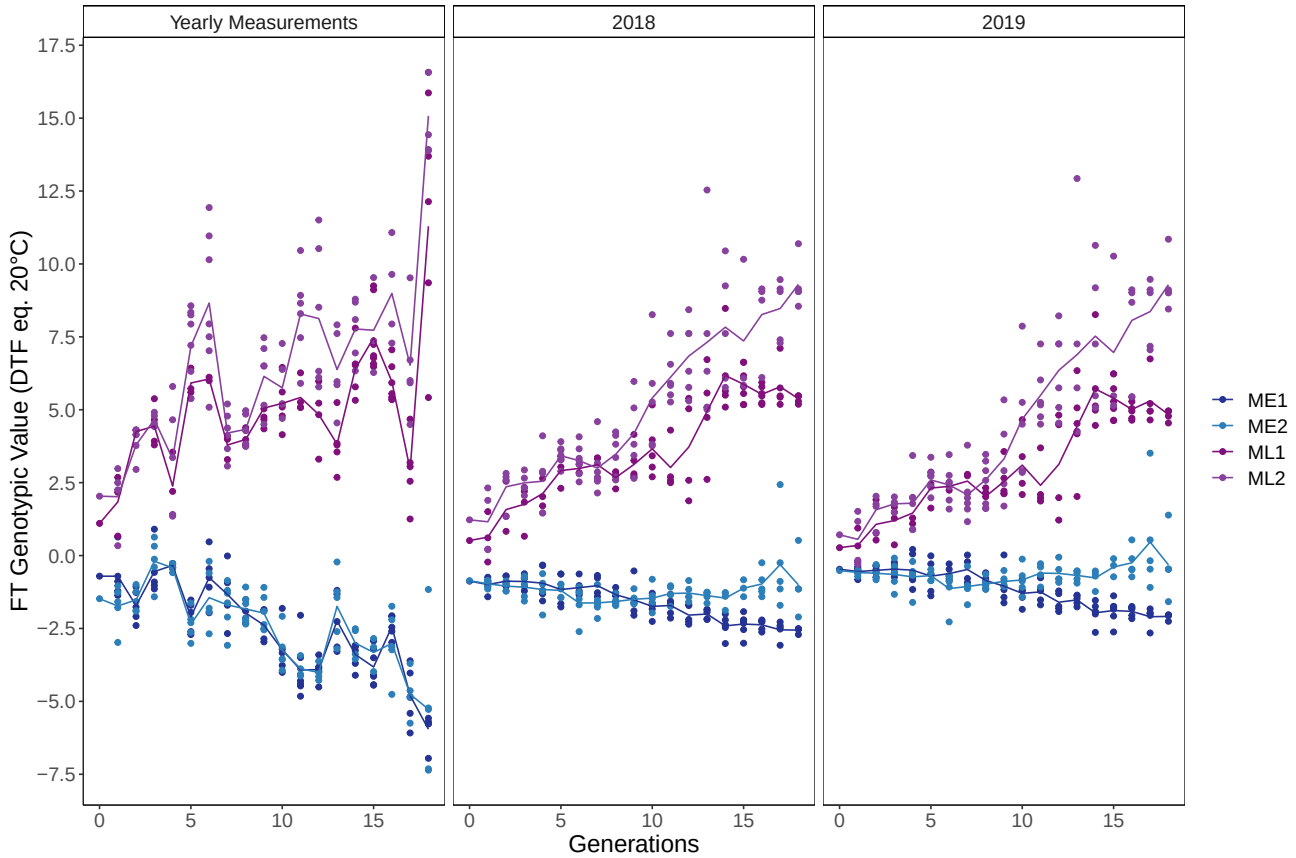

A)

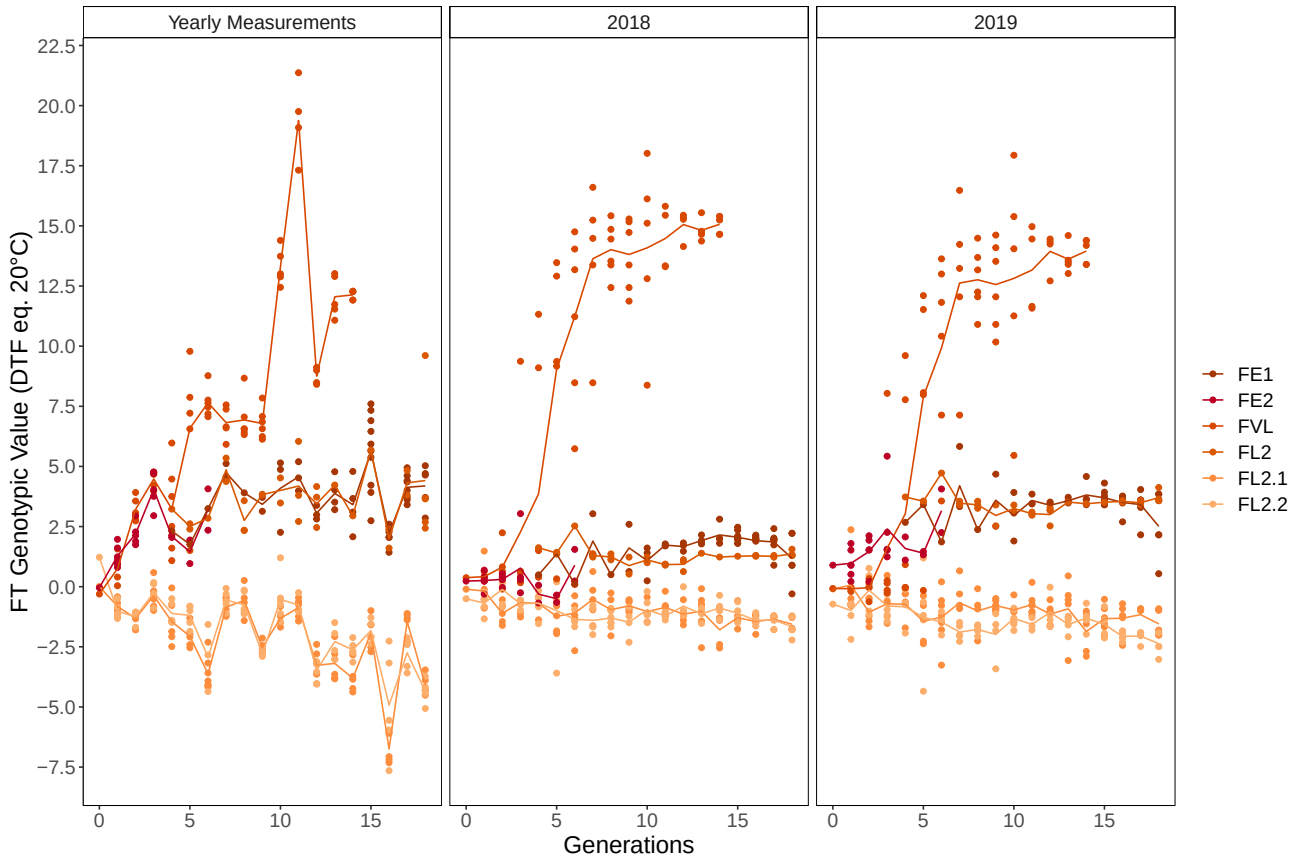

B)

Figure S15 Comparison between selection response for flowering time in each environment of evaluation for A) F252 and B) MBS. Left panels corresponds to total genetic values predicted from yearly measurements while middle and right panels corresponds to predicted breeding values from 2018 and 2019 common garden experiments. Colors indicate the different families. Colored lines indicate the evolution of the mean value per generation and per family through time. Each dot corresponds to a progenitor.

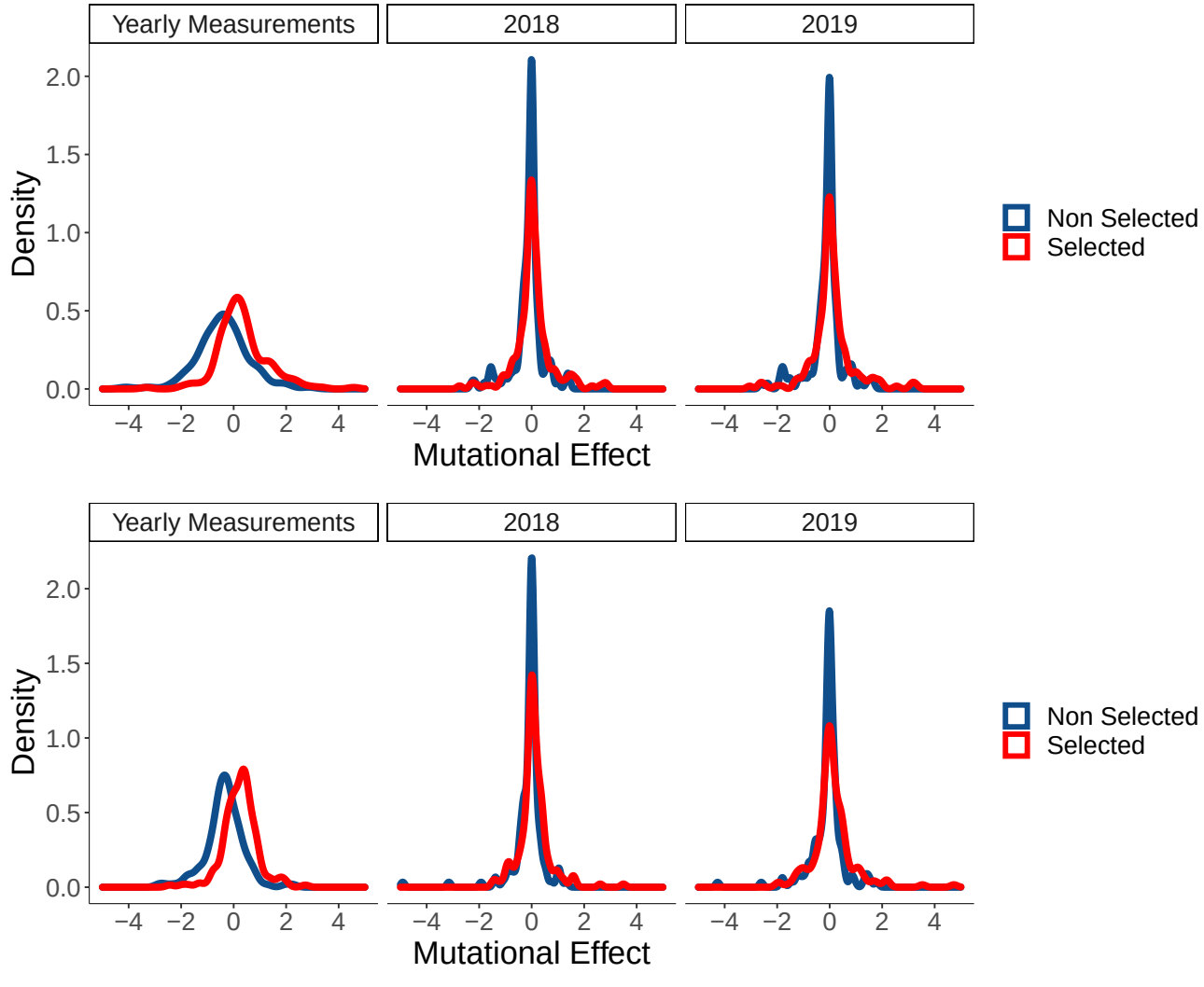

Figure S16 Comparison between estimated distribution of selected (in blue) and non selected (in red) mutational effects in each environment of evaluation for A) F252 and B) MBS. Positive values correspond to mutational effects of the same sign as the selection direction.

Table S5 Average selection response estimated through linear regression of genetic values over generations for DSECG (2018 and 2109) in MBS genetic background (a), and F252 (b). Slope, (R2) and significance of the regression are indicated for all measured traits.

(a) MBS

Family	ME1	ME1	ME2	ME2	ML1	ML1	ML2	ML2
Evaluation Year	2018	2019	2018	2019	2018	2019	2018	2019
fT	-0.098 (0.78) ***	-0.096 (0.75) ***	-0.006 (0.005)	0.0064 (0.0048)	0.24 (0.7) ***	0.24 (0.69) ***	0.41 (0.81) ***	0.46 (0.81) ***
hpl	-0.38 (0.59) ***	-0.39 (0.6) ***	-0.26 (0.75) ***	-0.65 (0.8) ***	-0.22 (0.45) ***	-0.091 (0.11) ***	-0.52 (0.65) ***	-0.13 (0.1) ***
nbl	-0.033 (0.65) ***	-0.035 (0.61) ***	-0.0057 (0.078) **	-0.021 (0.46) ***	-0.0049 (0.061) *	-0.017 (0.25) ***	0.018 (0.37) ***	0.035 (0.52) ***
upear	2.7e-05 (1.9e-06)	-0.00072 (0.0012)	-0.0075 (0.18) ***	-0.028 (0.66) ***	-0.0079 (0.25) ***	-0.016 (0.31) ***	-0.0021 (0.02)	0.036 (0.55) ***
lwear	-0.0042 (0.13) ***	-0.015 (0.51) ***	-0.0059 (0.36) ***	-0.018 (0.64) ***	-0.0035 (0.12) ***	-0.0079 (0.16) ***	0.0095 (0.51) ***	0.043 (0.74) ***
broot	-0.012 (0.46) ***	-0.014 (0.59) ***	-0.024 (0.77) ***	-0.024 (0.83) ***	-0.0081 (0.27) ***	-0.014 (0.47) ***	0.0025 (0.032) .	0.033 (0.72) ***
lbe	-0.062 (0.22) ***	-0.038 (0.053) *	-0.33 (0.7) ***	-0.34 (0.72) ***	0.059 (0.39) ***	0.053 (0.35) ***	0.034 (0.095) ***	-0.057 (0.23) ***
TKW	-0.33 (0.52) ***	-0.23 (0.39) ***	0.23 (0.32) ***	0.42 (0.66) ***	0.21 (0.18) ***	0.59 (0.6) ***	-0.07 (0.021)	0.12 (0.14) ***
Ear Weight	-0.68 (0.75) ***	-0.44 (0.5) ***	0.12 (0.061) **	0.17 (0.14) ***	-0.44 (0.38) ***	-0.52 (0.34) ***	-0.67 (0.69) ***	-0.96 (0.75) ***

'***', '**','*','.' indicates non zero statistical significance at the 10^{-3}, 10^{-2},5×10^{-2} level, respectively.

(b) F252

Family	FE1	FE1	FE2	FE2	FVL	FVL	FL2	FL2	FL2.1	FL2.1	FL2.2	FL2.2
Evaluation Year	2018	2019	2018	2019	2018	2019	2018	2019	2018	2019	2018	2019
fT	-0.056 (0.29) ***	-0.058 (0.19) ***	-0.053 (0.32) ***	-0.082 (0.4) ***	1.3 (0.67) ***	1.2 (0.66) ***	-0.00027 (3.8e-07)	0.31 (0.2) *	0.048 (0.11) **	0.012 (0.0052)	0.0023 (0.0022)	0.016 (0.074) .
hpl	-0.75 (0.7) ***	-0.34 (0.51) ***	0.02 (0.0023)	0.19 (0.12) ***	-1.5 (0.55) ***	-1.3 (0.55) ***	-2.3 (0.6) ***	-1.9 (0.5) ***	-0.49 (0.39) ***	-0.58 (0.4) ***	-0.067 (0.36) ***	-0.052 (0.25) ***
nbl	-0.021 (0.47) ***	-0.024 (0.55) ***	0.0029 (0.028) .	0.0026 (0.011)	0.18 (0.6) ***	0.16 (0.6) ***	-0.094 (0.3) **	-0.079 (0.25) *	-0.012 (0.19) ***	-0.017 (0.38) ***	0.00095 (0.013)	-0.0035 (0.21) ***
upear	-0.021 (0.41) ***	-0.024 (0.45) ***	-0.016 (0.58) ***	-0.014 (0.48) ***	0.18 (0.6) ***	0.18 (0.6) ***	-0.1 (0.27) *	-0.1 (0.28) **	0.001 (0.0012)	-0.0017 (0.0036)	-0.0011 (0.026)	-0.0043 (0.31) ***
lwear	-0.016 (0.37) ***	-0.02 (0.44) ***	-0.035 (0.68) ***	-0.031 (0.73) ***	0.17 (0.59) ***	0.19 (0.59) ***	-0.05 (0.095)	-0.1 (0.21) *	-0.00024 (5.4e-05)	-0.0045 (0.021)	-0.004 (0.29) ***	-0.0036 (0.4) ***
broot	-0.0054 (0.23) ***	-0.0076 (0.57) ***	0.0028 (0.035) .	0.0063 (0.26) ***	0.037 (0.68) ***	0.027 (0.66) ***	0.00018 (5.5e-06)	0.0014 (0.001)	-0.023 (0.34) ***	0.00059 (0.0016)	0.017 (0.85) ***	-0.0044 (0.51) ***
lbe	-0.11 (0.54) ***	-0.17 (0.65) ***	-0.022 (0.13) ***	-0.049 (0.38) ***	-0.14 (0.48) ***	-0.12 (0.49) ***	-0.1 (0.07)	-0.27 (0.21) *	-0.041 (0.3) ***	-0.034 (0.2) ***	-0.12 (0.82) ***	-0.12 (0.82) ***
TKW	-0.39 (0.18) ***	-0.93 (0.48) ***	0.14 (0.052) *	-0.38 (0.21) ***	-4.7 (0.57) ***	-5.7 (0.58) ***	-4.6 (0.63) ***	-9.3 (0.71) ***	0.11 (0.01)	-0.35 (0.059) *	-1 (0.88) ***	-1.4 (0.88) ***
Ear Weight	0.16 (0.077) **	0.11 (0.059) **	-0.55 (0.66) ***	-0.48 (0.68) ***	-3 (0.63) ***	-2 (0.64) ***	0.77 (0.075)	-0.067 (0.0012)	-0.51 (0.49) ***	-0.5 (0.65) ***	-0.28 (0.54) ***	-0.091 (0.25) ***

'***', '**','*','.' indicates non zero statistical significance at the 10^{-3}, 10^{-2},5×10^{-2} level, respectively.

Table S6 **Variance (standard error) decomposition in DSECG for each traits for MBS genetic background (a), and F252 (b).**

(a) MBS

	FT	HT	#L	PHY	UE	LE	BR	LL	TKW	EW
$\sigma^2_{0_{2018}}$	1.03 (0.465) *	0 (0.684)	8.56E-02 (3.65E-02) **	4.93E-04 (4.48E-04)	1.64E-02 (1.00E-02) .	1.24E-02 (7.51E-03) .	5.08E-03 (8.07E-03)	0.192 (0.239)	16.3 (9.61) *	0 (0.672)
$\sigma_{0_{2018,2019}}$	0.543 (0.283) *	2.24 (1.41) .	0.112 (4.63E-02) **	-1.02E-03 (3.59E-04)	3.25E-02 (1.75E-02) *	2.33E-02 (1.14E-02) *	4.76E-03 (5.76E-03)	0.256 (0.249)	6.2 (3.99) .	-0.188 (0.602)
$\sigma^2_{0_{2019}}$	0.206 (0.176)	7.2 (3.44) *	0.147 (6.27E-02) **	2.10E-04 (5.23E-04)	5.56E-02 (3.14E-02) *	3.42E-02 (1.87E-02) *	0 (4.66E-03)	0.187 (0.27)	0 (1.86)	0 (0.782)
$\sigma^2_{m_{2018}}$	0.112 (1.42E-02) ***	0.454 (9.58E-02) ***	2.66E-03 (5.17E-04) ***	6.43E-05 (3.70E-05) *	1.48E-03 (3.69E-04) ***	1.32E-03 (3.61E-04) ***	2.35E-03 (5.98E-04) ***	0.132 (2.07E-02) ***	1.1 (0.384) **	0.87 (9.44E-02) ***
$\sigma_{m_{2018,2019}}$	0.122 (1.36E-02) ***	0.369 (7.00E-02) ***	3.09E-03 (5.60E-04) ***	1.55E-04 (4.44E-05) ***	1.59E-03 (4.03E-04) ***	1.54E-03 (3.69E-04) ***	1.77E-03 (4.13E-04) ***	0.114 (1.67E-02) ***	0.595 (0.225) **	0.898 (7.33E-02) ***
$\sigma^2_{m_{2019}}$	0.14 (1.62E-02) ***	0.499 (9.82E-02) ***	4.70E-03 (9.08E-04) ***	8.34E-05 (7.59E-05)	3.80E-03 (7.90E-04) ***	4.11E-03 (7.00E-04) ***	2.88E-03 (5.40E-04) ***	0.134 (1.98E-02) ***	1.16 (0.27) ***	1.24 (0.113) ***
σ^2_{2018}	0.272 (7.61E-02) ***	8.5 (1.7) ***	4.25E-02 (4.46E-03) ***	1.01E-02 (1.18E-03) ***	5.57E-02 (5.51E-03) ***	3.12E-02 (7.65E-03) ***	3.32E-02 (1.03E-02) ***	1.5 (0.246) ***	53.7 (6.72) ***	0 (3.74)
σ^2_{2019}	0.795 (0.109) ***	6.22 (1.58) ***	8.25E-02 (8.07E-03) ***	5.24E-02 (4.11E-03) ***	8.93E-02 (8.55E-03) ***	6.12E-02 (9.74E-03) ***	0 (7.16E-03)	1.46 (0.237) ***	42.5 (5.59) ***	0 (3.78)
Intercept (2018)	78.2 (0.691) ***	1.41E+02 (1.15) ***	18.3 (0.169) ***	3.25 (3.63E-02) ***	12.7 (8.46E-02) ***	11.6 (9.85E-02) ***	7.7 (7.52E-02) ***	69.9 (0.518) ***	1.98E+02 (2.73) ***	62.3 (1.11) ***
2019 Effect	7.64 (0.494) ***	-25.8 (1.75)	-0.652 (8.86E-02)	-6.72E-02 (5.25E-02)	-0.123 (7.64E-02)	-0.28 (0.102)	1.07 (6.31E-02) ***	-5.65 (0.446)	17.7 (1.88) ***	3.15 (1.3) **
$h^2_{m_{2018}} = \frac{\sigma^2_{m_{2018}}}{\sigma^2_{2018}}$	0.411 (0.133) **	5.34E-02 (1.79E-02) **	6.27E-02 (1.51E-02) ***	6.39E-03 (4.00E-03) .	2.65E-02 (7.80E-03) ***	4.22E-02 (1.79E-02) **	7.08E-02 (3.29E-02) *	8.78E-02 (2.19E-02) ***	2.05E-02 (8.47E-03) **	NA (NA)
$h^2_{m_{2019}} = \frac{\sigma^2_{m_{2019}}}{\sigma^2_{2019}}$	0.176 (3.31E-02) ***	8.02E-02 (2.98E-02) **	5.69E-02 (1.33E-02) ***	1.59E-03 (1.48E-03)	4.26E-02 (1.06E-02) ***	6.71E-02 (1.78E-02) ***	NA (NA)	9.21E-02 (2.23E-02) ***	2.73E-02 (8.21E-03) ***	NA (NA)

'***', '**', '*', '.' indicates non zero statistical significance at the 10^{-3}, 10^{-2},5×10^{-2} level, respectively.

(b) F252

	FT	HT	#L	PHY	UE	LE	BR	LL	TKW	EW
$\sigma^2_{0_{2018}}$	12.9 (3.93) ***	69 (23.4) **	0.345 (0.115) **	8.52E-04 (1.00E-03)	0.376 (0.119) ***	0.293 (9.87E-02) **	1.40E-02 (1.21E-02)	0.723 (0.364) *	2.75E+02 (98.2) **	2.56E+02 (70.5) ***
$\sigma_{0_{2018,2019}}$	11.5 (3.81) **	59.4 (22.6) **	0.311 (0.102) **	1.87E-03 (1.72E-03)	0.375 (0.117) ***	0.349 (0.112) ***	2.62E-03 (5.52E-03)	1.64 (0.637) **	3.56E+02 (1.22E+02) **	1.72E+02 (47.6) ***
$\sigma^2_{0_{2019}}$	11.7 (4.1) **	78.2 (28.6) **	0.283 (9.59E-02) **	4.30E-03 (4.03E-03)	0.377 (0.119) ***	0.421 (0.138) **	1.88E-03 (3.13E-03)	3.19 (1.22) **	4.62E+02 (1.65E+02) **	1.14E+02 (33.3) ***
$\sigma^2_{m_{2018}}$	8.74E-02 (1.62E-02) ***	0.512 (0.146) ***	3.43E-03 (6.72E-04) ***	1.02E-04 (6.36E-05) .	2.87E-03 (6.36E-04) ***	2.96E-03 (7.42E-04) ***	1.13E-03 (5.06E-04) *	8.32E-02 (1.72E-02) ***	3.34 (0.797) ***	0.781 (0.211) ***
$\sigma_{m_{2018,2019}}$	0.118 (1.99E-02) ***	0.453 (0.128) ***	2.46E-03 (5.41E-04) ***	8.93E-05 (7.20E-05)	2.42E-03 (5.10E-04) ***	1.69E-03 (5.79E-04) **	1.07E-03 (2.66E-04) ***	5.83E-02 (1.26E-02) ***	2.65 (0.821) ***	0.385 (0.169) *
$\sigma^2_{m_{2019}}$	0.144 (3.09E-02) ***	0.61 (0.197) ***	2.60E-03 (6.74E-04) ***	1.17E-04 (1.64E-04)	2.48E-03 (6.16E-04) ***	2.35E-03 (8.17E-04) **	6.24E-04 (1.80E-04) ***	6.94E-02 (1.69E-02) ***	5.26 (1.49) ***	0.741 (0.242) **
σ^2_{2018}	0.781 (8.83E-02) ***	14.5 (1.67) ***	4.51E-02 (4.96E-03) ***	1.55E-02 (1.58E-03) ***	5.46E-02 (5.87E-03) ***	7.87E-02 (8.52E-03) ***	0.172 (1.51E-02) ***	1.43 (0.308) ***	80.1 (8.7) ***	19 (2.1) ***
σ^2_{2019}	2.99 (0.303) ***	22.9 (2.45) ***	7.06E-02 (7.24E-03) ***	5.69E-02 (5.42E-03) ***	5.69E-02 (5.90E-03) ***	0.105 (1.09E-02) ***	3.68E-02 (3.70E-03) ***	1.06 (0.285) ***	1.71E+02 (17.6) ***	34 (3.5) ***
Intercept (2018)	63.1 (1.98) ***	1.45E+02 (4.77) ***	16 (0.325) ***	2.98 (3.33E-02) ***	11.5 (0.337) ***	10.7 (0.301) ***	6.65 (0.108) ***	66.1 (0.636) ***	2.33E+02 (9.24) ***	67.6 (8.74) ***
2019 Effect	11.7 (0.84) ***	-46.5 (3.69)	-1.67 (8.99E-02)	0.882 (4.78E-02) ***	-0.749 (7.46E-02)	-1.17 (0.112)	0.327 (0.124) **	-11 (0.703)	16.9 (3.98) ***	-20.7 (3.29)
$h^2_{m_{2018}} = \frac{\sigma^2_{m_{2018}}}{\sigma^2_{2018}}$	0.112 (2.60E-02) ***	3.54E-02 (1.21E-02) **	7.60E-02 (1.85E-02) ***	6.61E-03 (4.45E-03) .	5.26E-02 (1.41E-02) ***	3.76E-02 (1.13E-02) ***	6.58E-03 (3.15E-03) *	5.83E-02 (2.02E-02) **	4.17E-02 (1.21E-02) ***	4.11E-02 (1.31E-02) ***
$h^2_{m_{2019}} = \frac{\sigma^2_{m_{2019}}}{\sigma^2_{2019}}$	4.80E-02 (1.21E-02) ***	2.67E-02 (9.84E-03) **	3.68E-02 (1.10E-02) ***	2.05E-03 (2.97E-03)	4.35E-02 (1.26E-02) ***	2.24E-02 (8.74E-03) **	1.70E-02 (5.55E-03) **	6.52E-02 (2.74E-02) **	3.08E-02 (1.01E-02) **	2.18E-02 (8.07E-03) **

'***', '**', '*', '.' indicates non zero statistical significance at the 10^{-3}, 10^{-2},5×10^{-2} level, respectively.

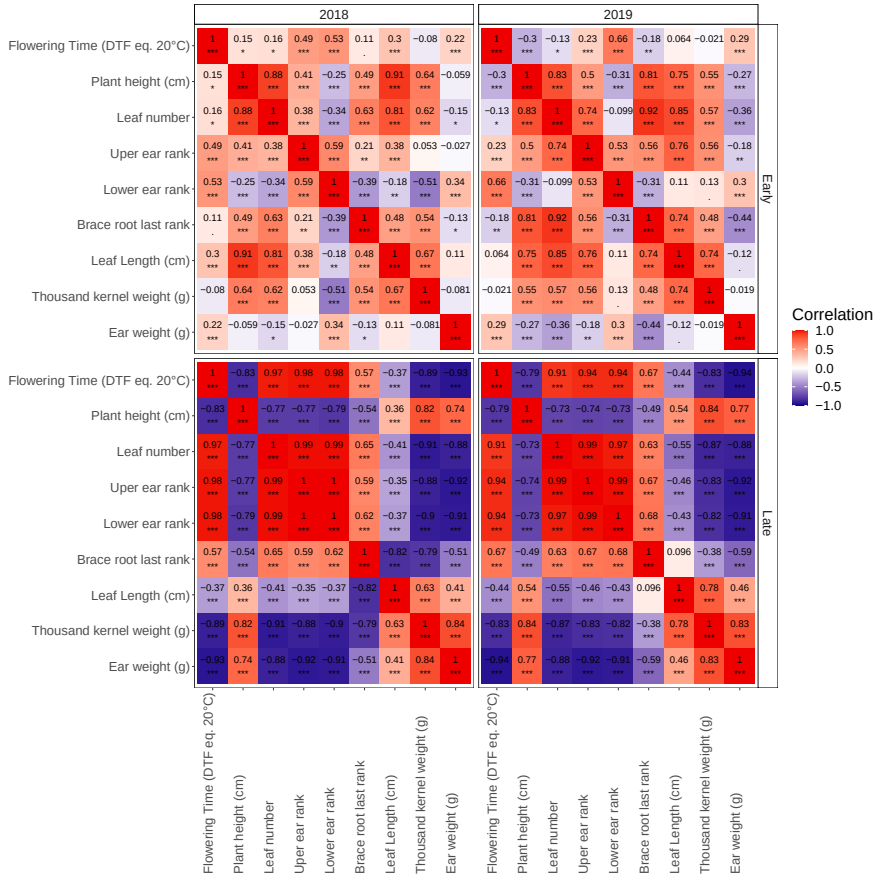

A)

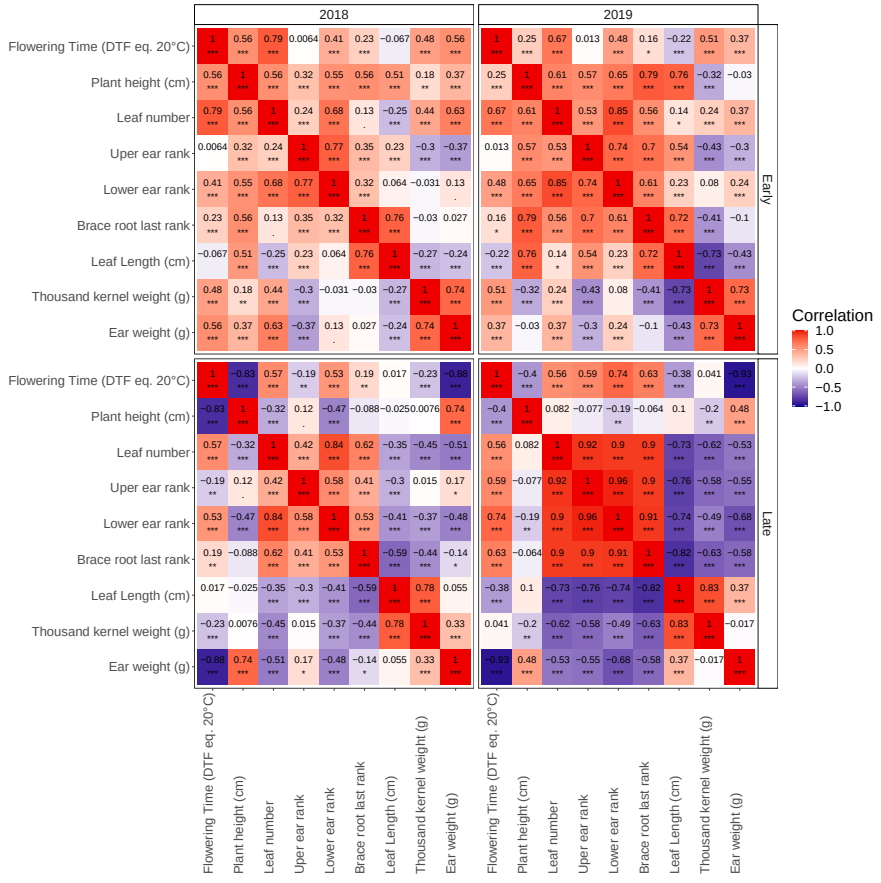

B)

Figure S17 Correlation matrix of the predicted environment specific total breeding values for all measured pairs of traits for A) F252 and B) MBS. Pearson's correlation coefficients were computed by environment and by population. Color corresponds the intensity of the correlations. '***', '**','*','.' indicates statistical significance at the 10^{-3}, 10^{-2},5×10^{-2} level, respectively.

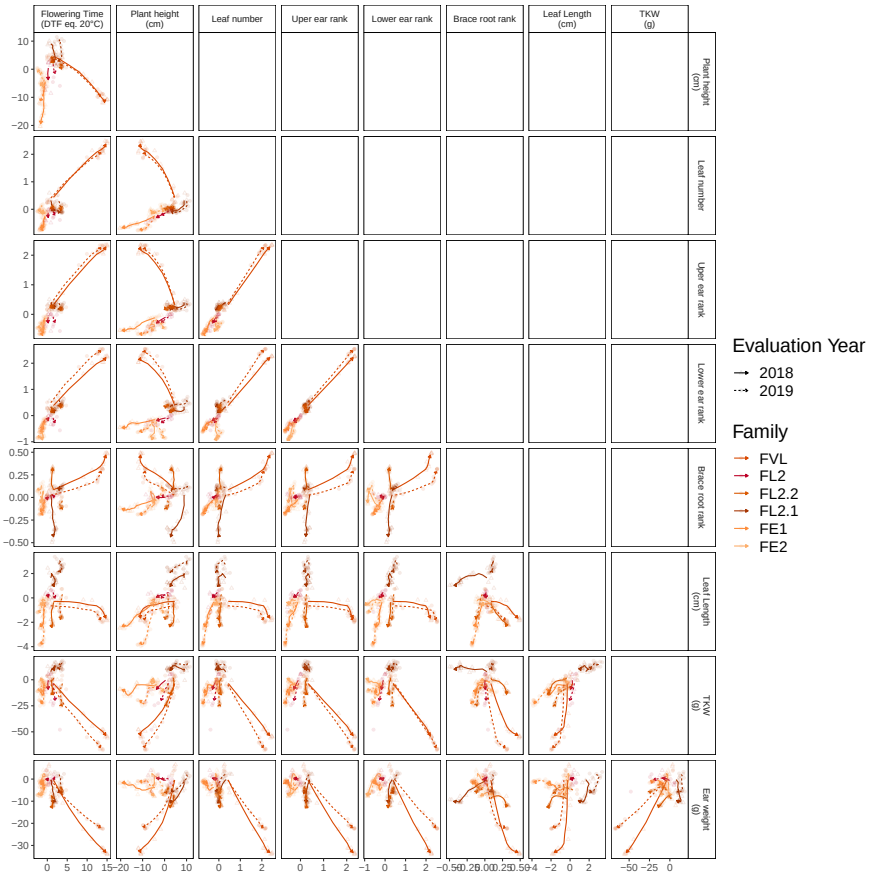

A)

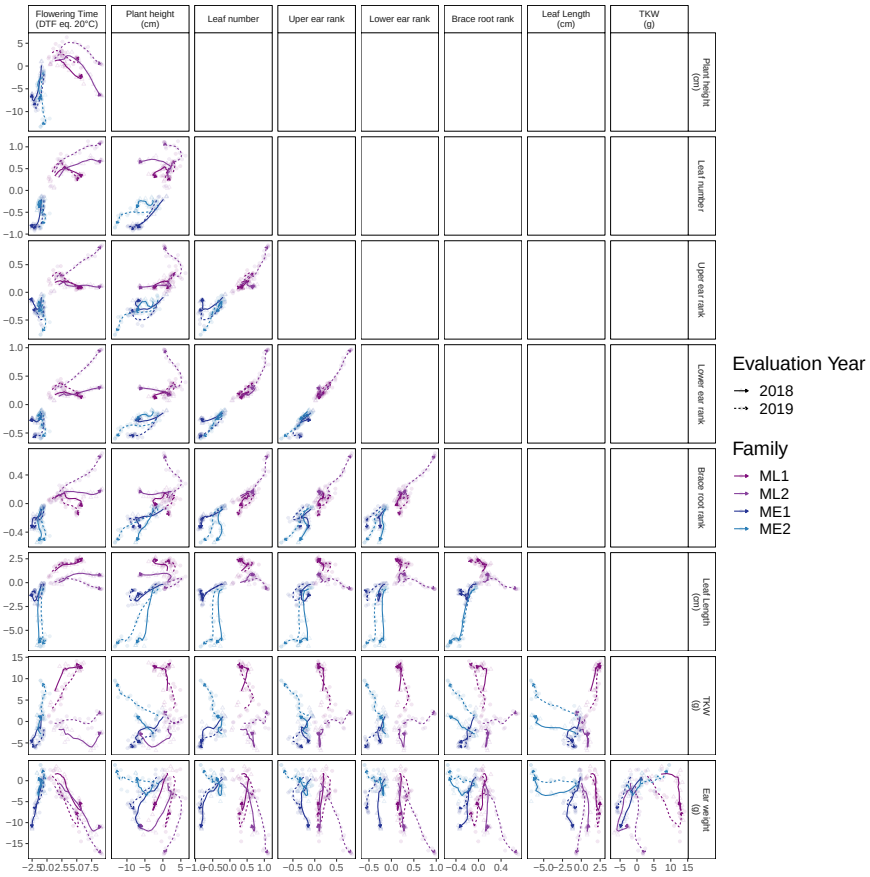

B)

Figure S18 Evolution through generations of the environment specific breeding values for all pair of measured traits. for A) F252 and B) MBS. Colored lines indicate the evolution through time of the rolling mean breeding value per generation, family and evaluation year. Solid lines correspond to 2018 while dotted lines refer to 2019. Each transparent point corresponds to the average breeding value of a generation per family. Dots correspond to 2018 specific breeding values, while triangles correspond to 2019.

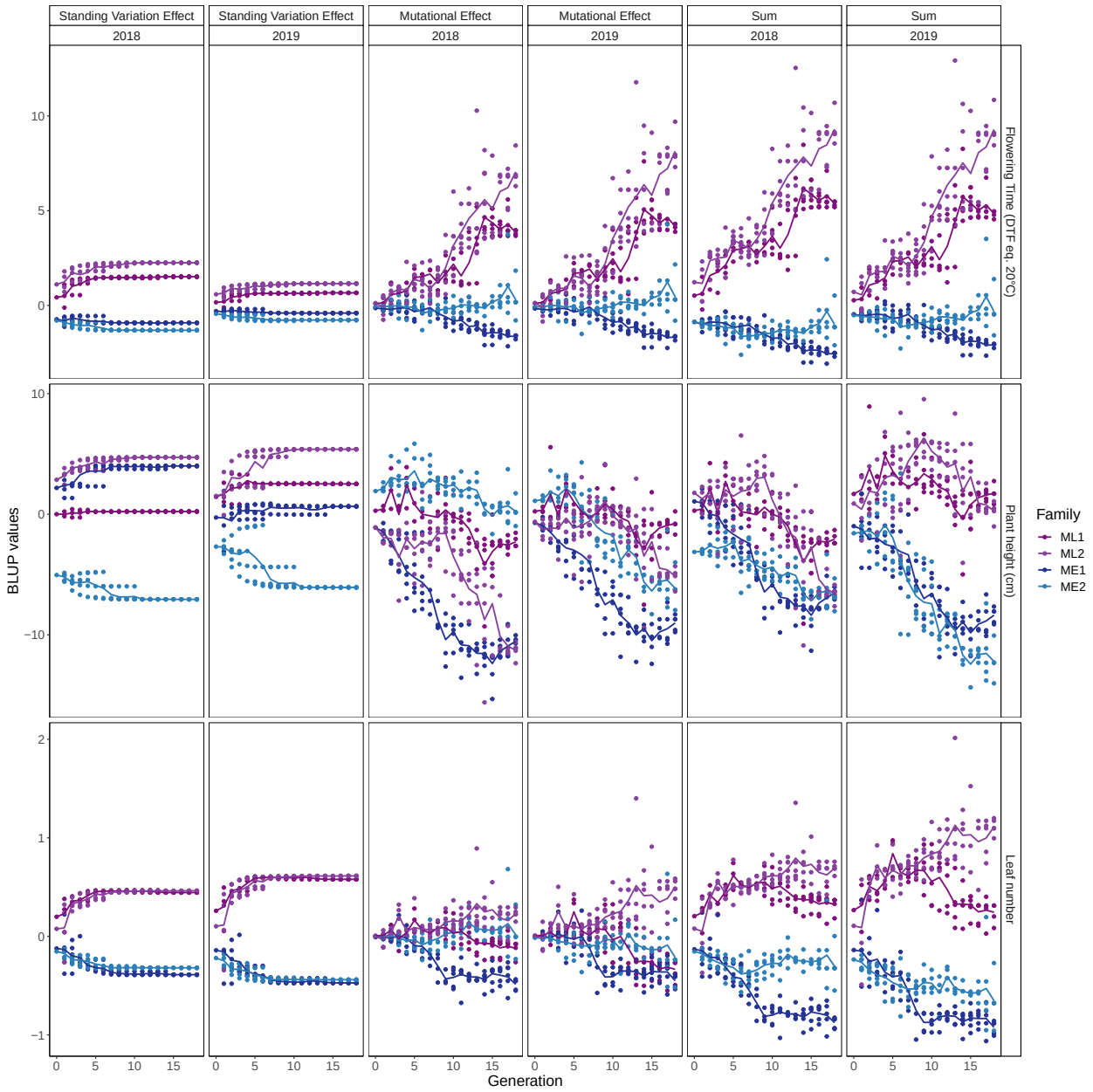

Figure S19 Evolution through generations of the BLUP values for each trait in the two DSECG environments (2018 and 2019) in MBS. Colored lines indicate the evolution of the mean value per generation and family through time. Each dot corresponds to a progenitor.

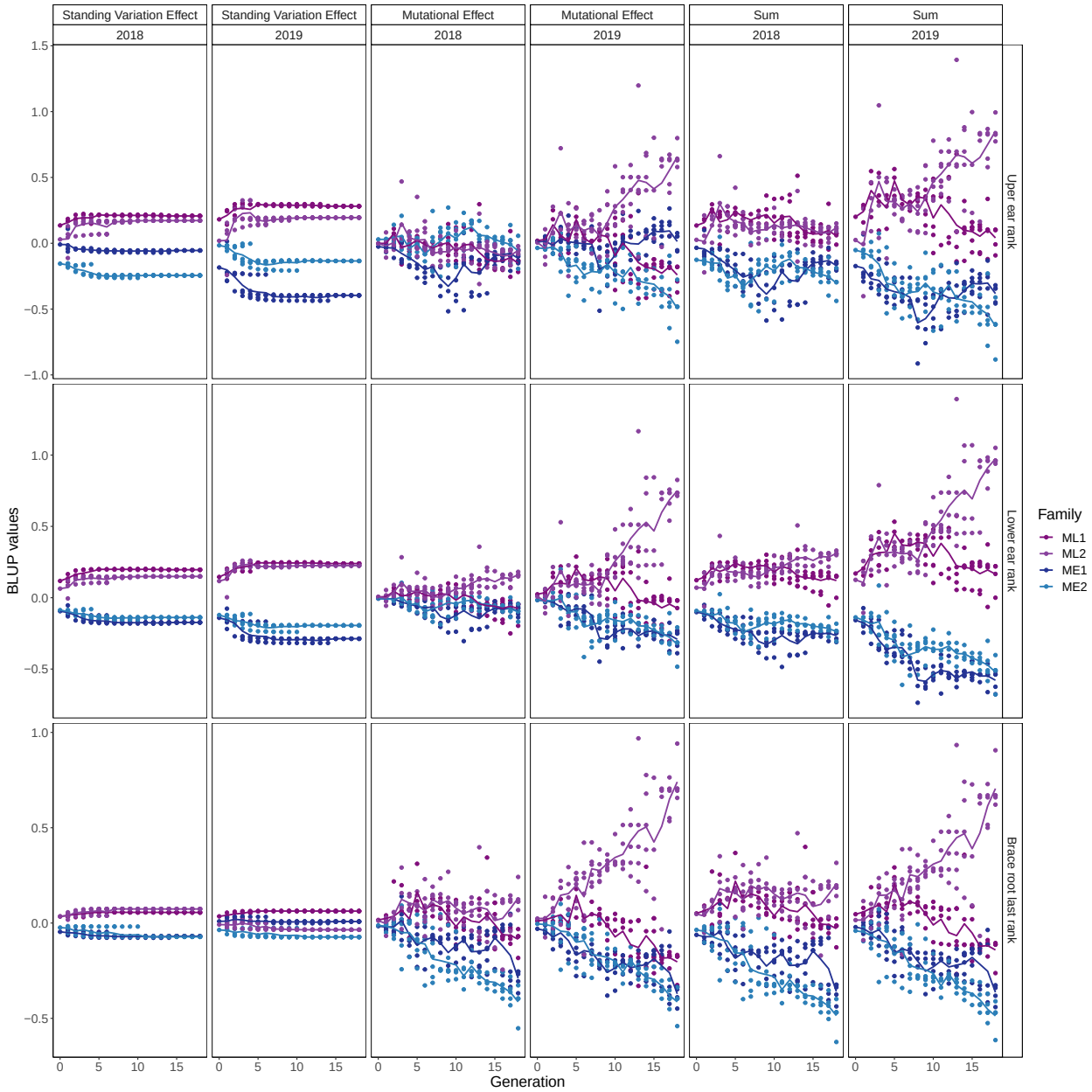

Figure S19 (Continued) Evolution through generations of the BLUP values for each trait in the two DSECG environments (2018 and 2019) in MBS. Colored lines indicate the evolution of the mean value per generation and family through time. Each dot corresponds to a progenitor.

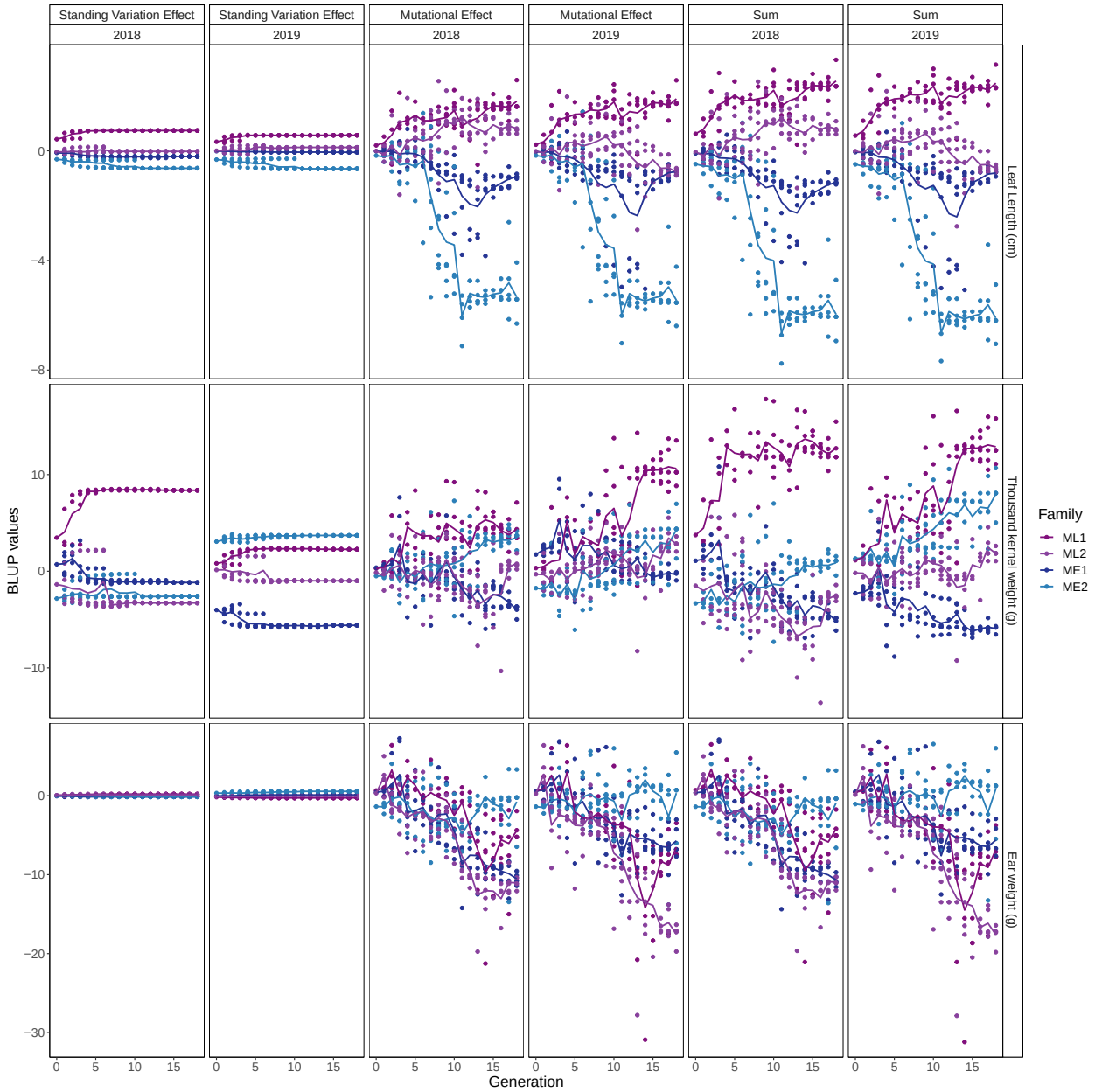

Figure S19 (Continued) Evolution through generations of the BLUP values for each trait in the two DSECG environments (2018 and 2019) in MBS. Colored lines indicate the evolution of the mean value per generation and family through time. Each dot corresponds to a progenitor.

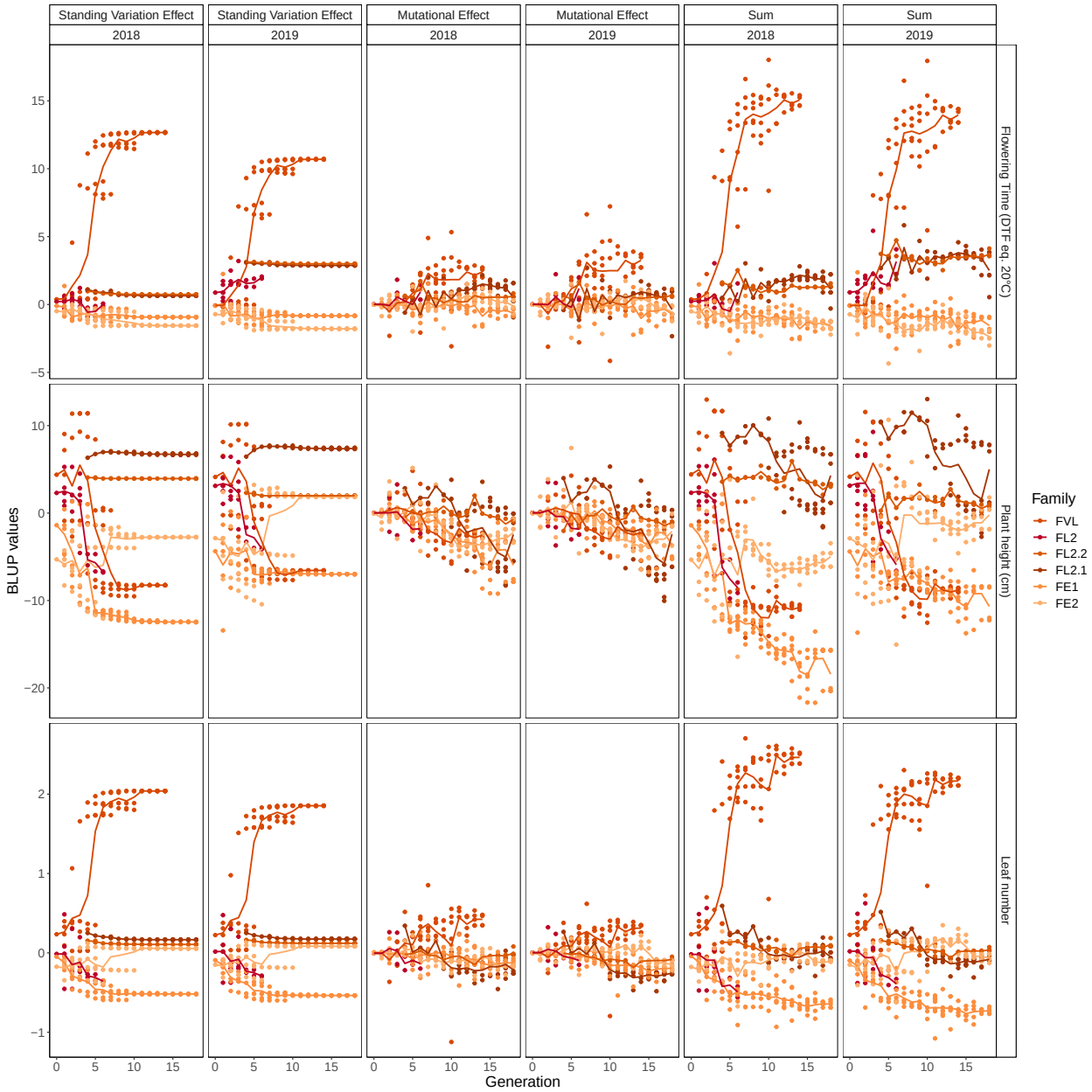

Figure S20 Evolution through generations of the BLUP values for each trait in the two DSECG environments (2018 and 2019) in F252. Colored lines indicate the evolution of the mean value per generation and family through time. Each dot corresponds to a progenitor.

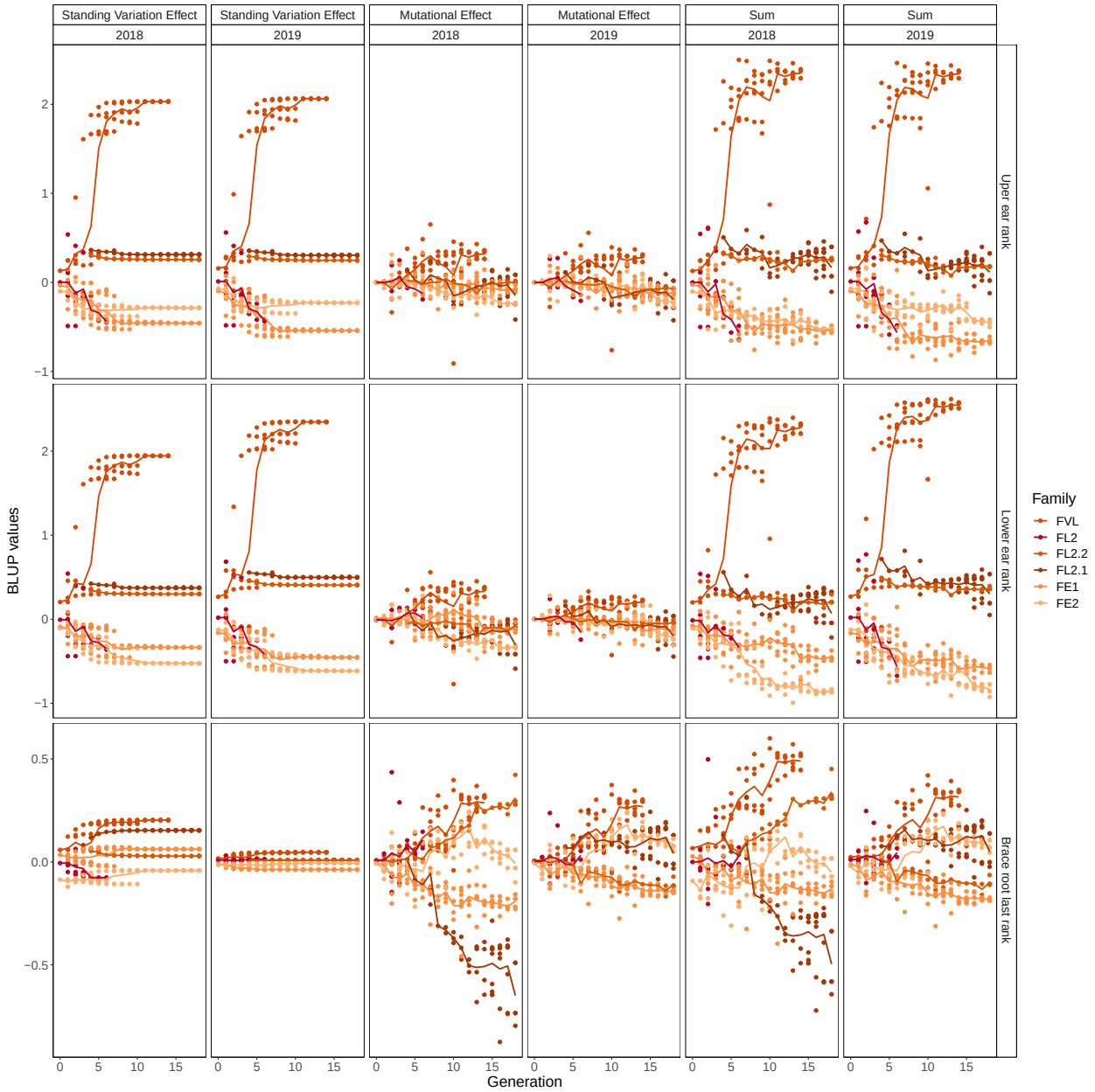

Figure S20 (Continued) Evolution through generations of the BLUP values for each trait in the two DSECG environments (2018 and 2019) in F252. Colored lines indicate the evolution of the mean value per generation and family through time. Each dot corresponds to a progenitor.

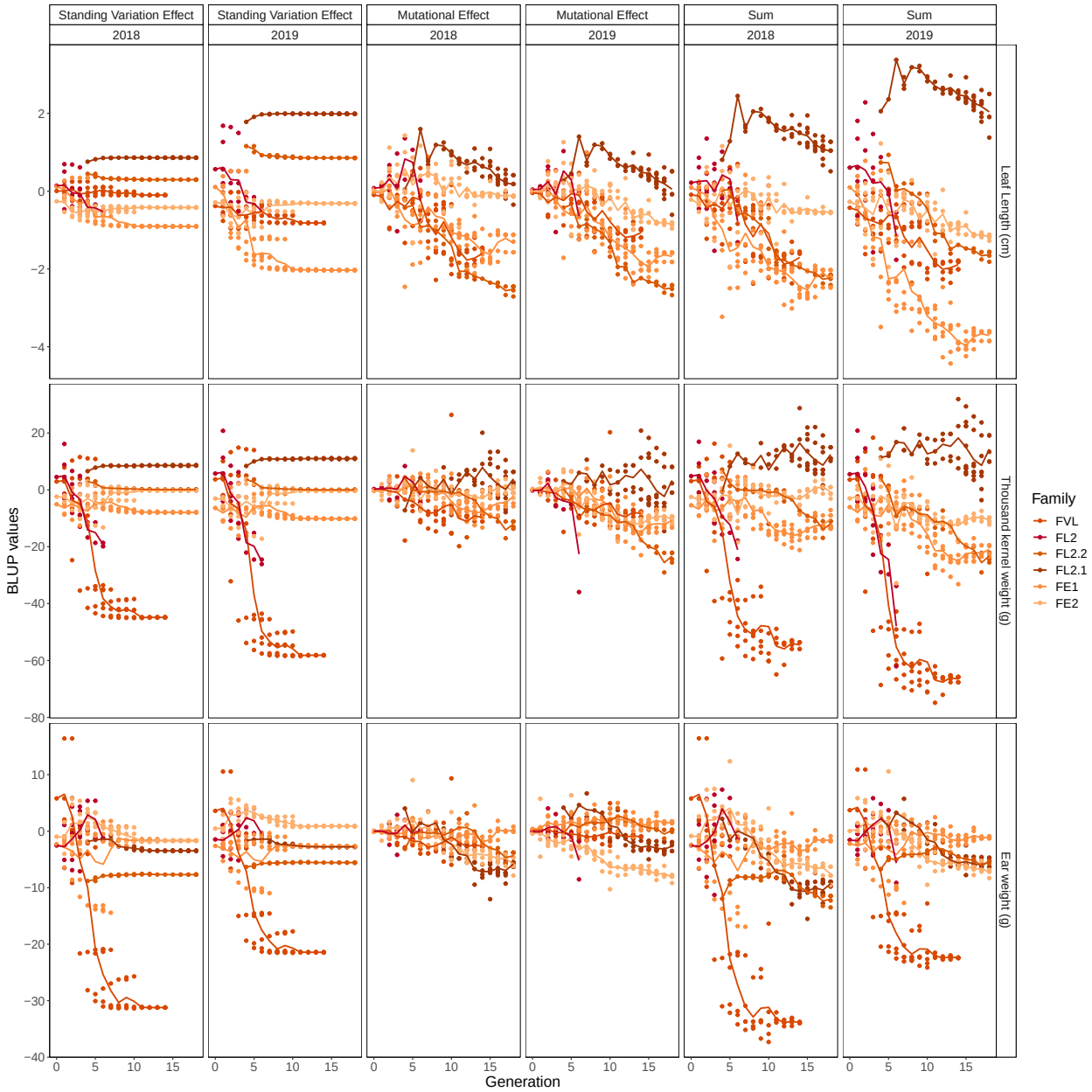

Figure S20 (Continued) Evolution through generations of the BLUP values for each trait in the two DSECG environments (2018 and 2019) in F252. Colored lines indicate the evolution of the mean value per generation and family through time. Each dot corresponds to a progenitor.

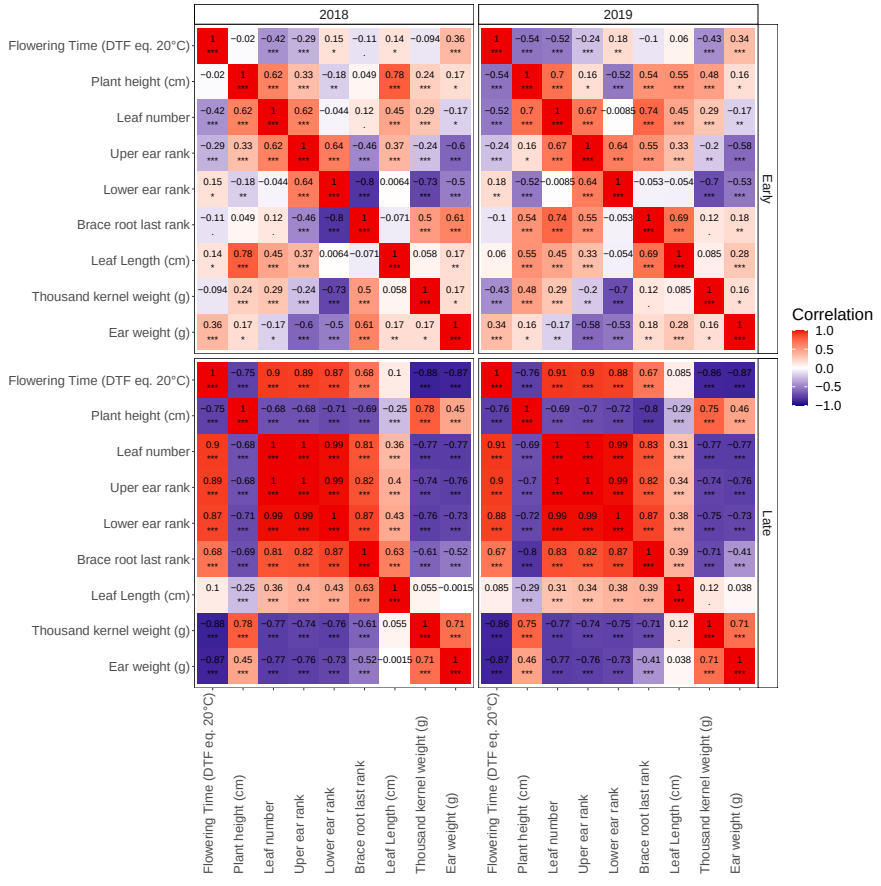

A)

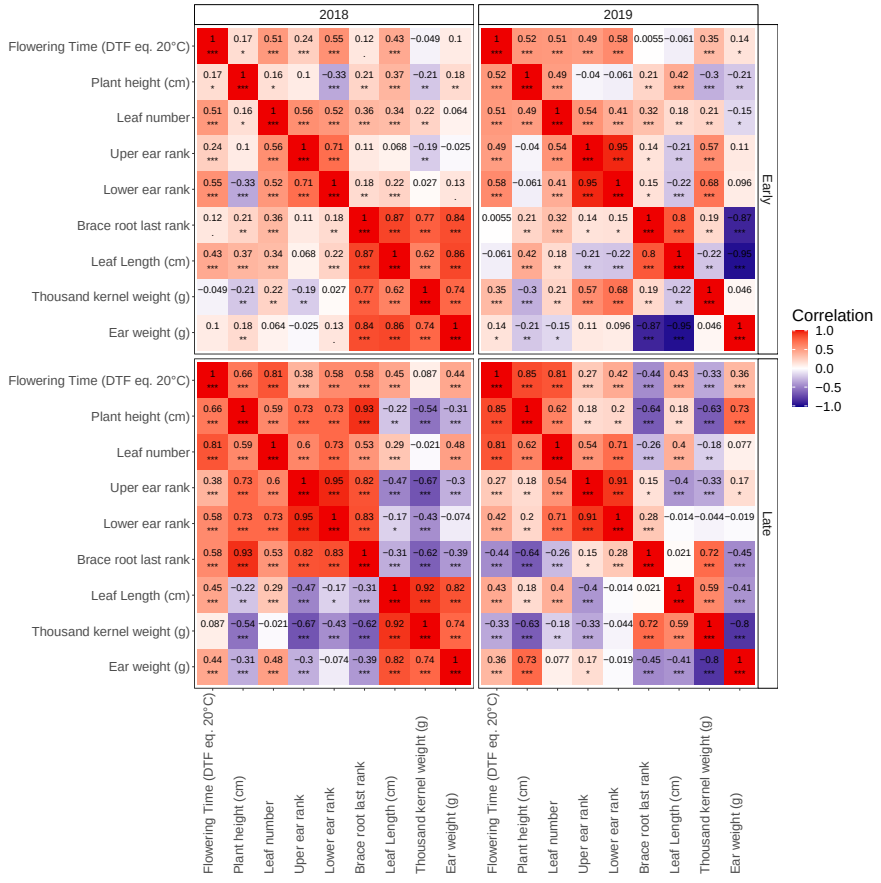

B)

Figure S21 Correlation matrix of the predicted environment specific standing variation contribution for all measured pairs of traits for A) F252 and B) MBS. Pearson's correlation coefficients were computed by environment and by population. Color corresponds the intensity of the correlations. '***', '**', '*', '.' indicates statistical significance at the 10^{-3}, 10^{-2},5×10^{-2} level, respectively.

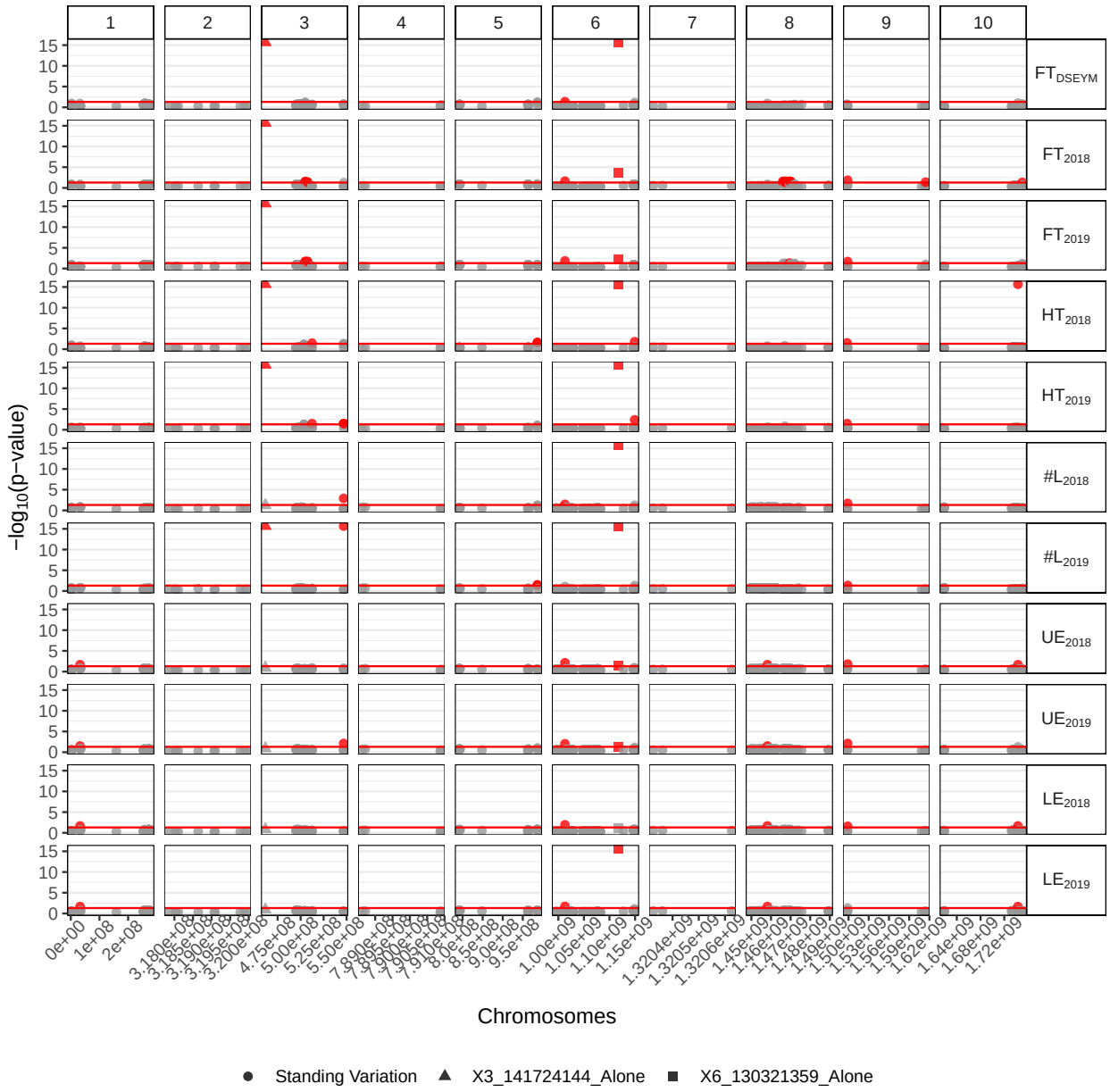

Figure S22 In F252, Manhattan plot for each trait representing the significance of the association of each SNPs ($-log_{10}(p-value)$, $FDR < 5\%$). Each row of panels corresponds to one trait. Each column of panels corresponds to a chromosome. X-axis indicates the position of SNPs along the chromosomes in bp. Red point (resp. gray point) corresponds to significant (resp. non-significant) association to the trait for the corresponding SNP. Standing variation are represented by a dot, while the two detected mutations are represented respectively by a triangle or a square.

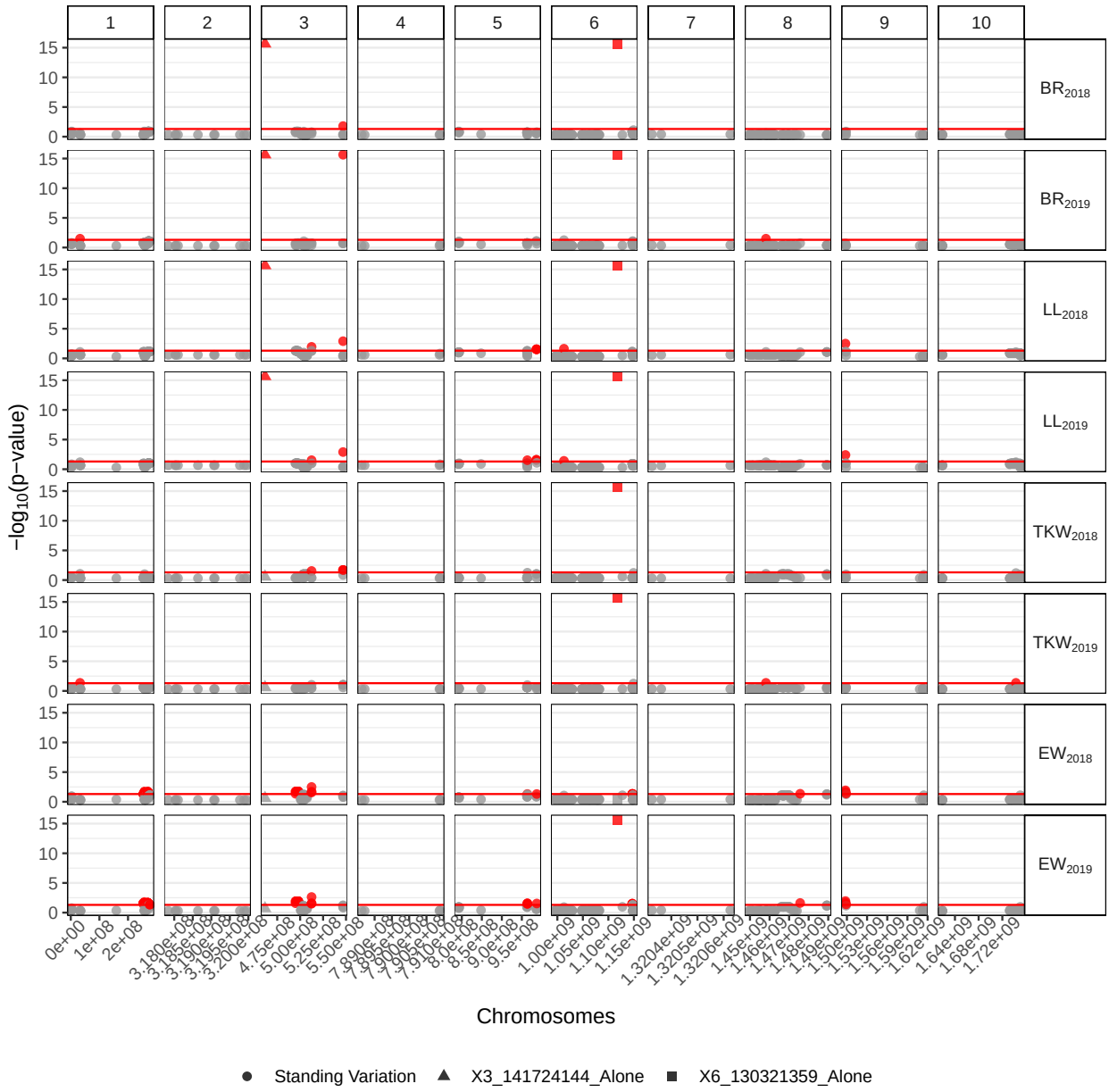

Figure S22 In F252, Manhattan plot for each trait representing the significance of the association of each SNPs ($-log_{10}(p-value)$, $FDR < 5\%$). Each row of panels corresponds to one trait. Each column of panels corresponds to a chromosome. X-axis indicates the position of SNPs along the chromosomes in bp. Red point (resp. gray point) corresponds to significant (resp. non-significant) association to the trait for the corresponding SNP. Standing variation are represented by a dot, while the two detected mutations are represented respectively by a triangle or a square.

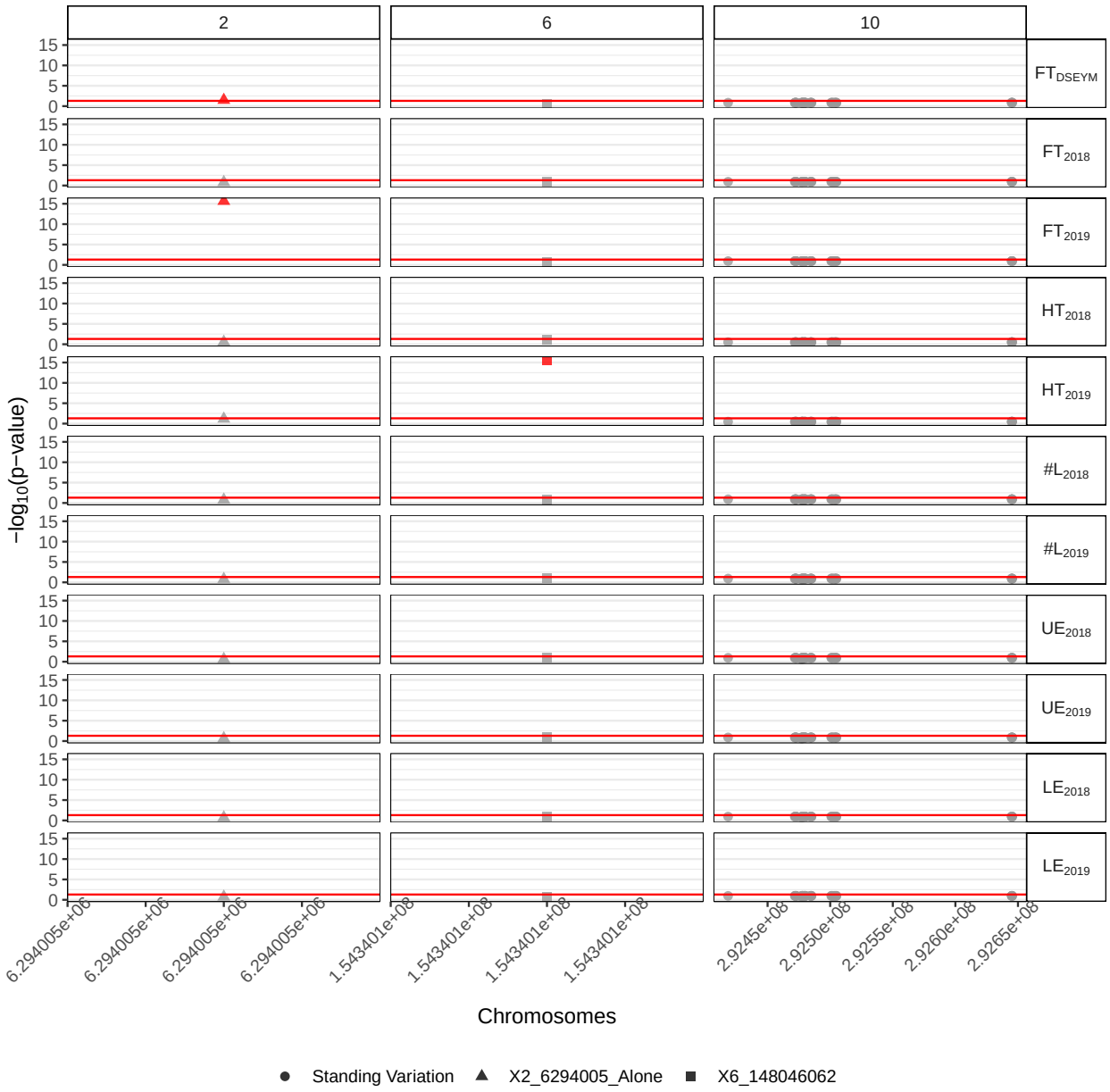

Figure S22 In MBS, Manhattan plot for each trait representing the significance of the association of each SNPs ($-log_{10}(p-value)$, $FDR < 5\%$). Each row of panels corresponds to one trait. Each column of panels corresponds to a chromosome. X-axis indicates the position of SNPs along the chromosomes in bp. Red point (resp. gray point) corresponds to significant (resp. non-significant) association to the trait for the corresponding SNP. Standing variation are represented by a dot, while the two detected mutations are represented respectively by a triangle or a square.

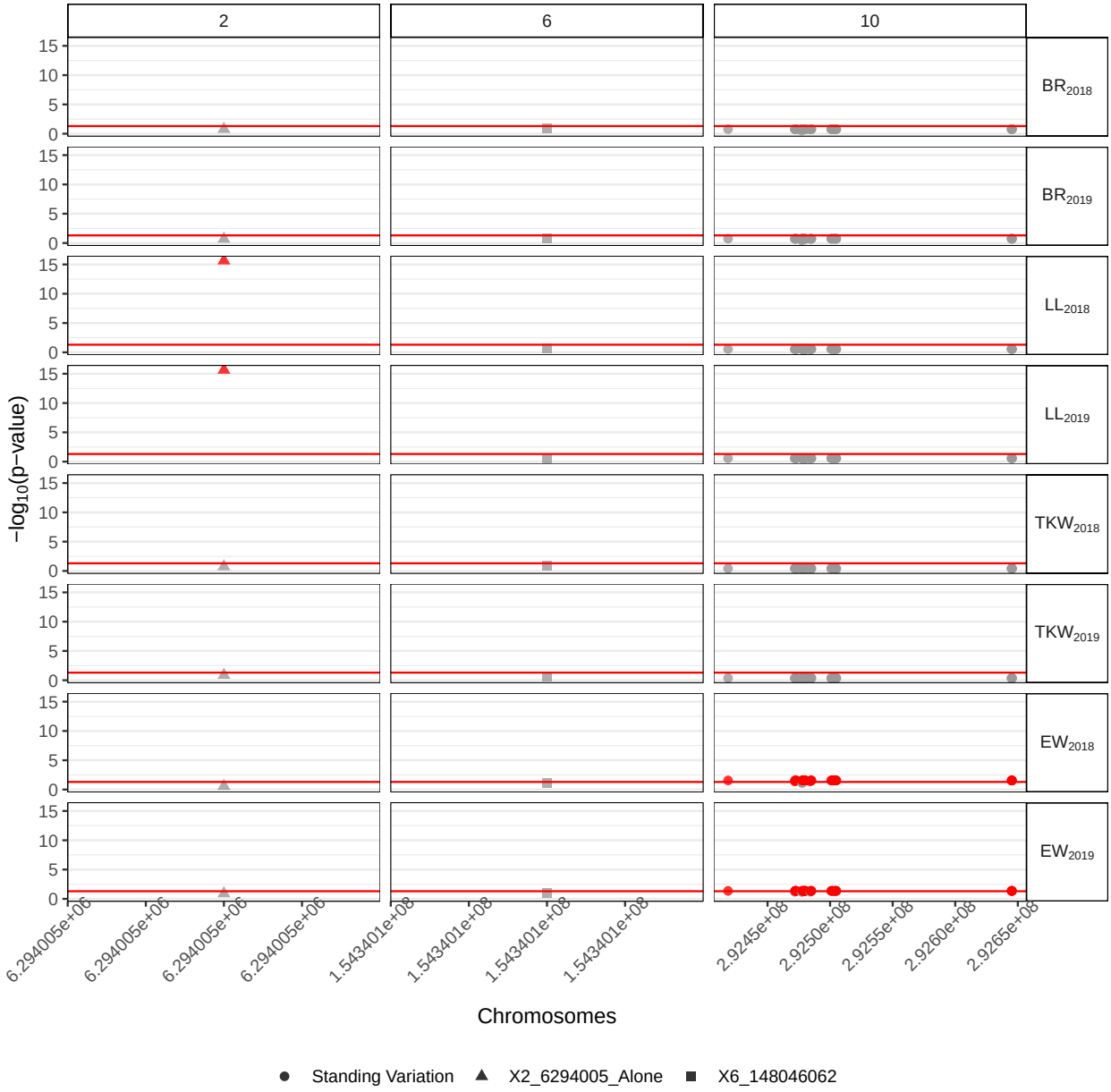

Figure S22 In MBS, Manhattan plot for each trait representing the significance of the association of each SNPs ($-log_{10}(p-value)$, $FDR < 5\%$). Each row of panels corresponds to one trait. Each column of panels corresponds to a chromosome. X-axis indicates the position of SNPs along the chromosomes in bp. Red point (resp. gray point) corresponds to significant (resp. non-significant) association to the trait for the corresponding SNP. Standing variation are represented by a dot, while the two detected mutations are represented respectively by a triangle or a square.

Table S7 Significant trait association (allele effect) in 2018, 2019 DSECG as well as DSEYM in MBS. The first columns provide information on the chromosome, position, gene id and knwon description.

Inbred	CHROM	POS	Gene id	Gene function	2018	2019	DSEYM
MBS	2	6,294,005	Zm00001d002125	nuclear RNA polymerase D2/E2	LL(1.06)	FT(0.73); LL(1.14)	FT(1.43)
MBS	6	148,046,062	Zm00001d038104	Mannosylglycoprotein endo-beta-mannosidase	.	HT(1.05)	.
MBS	10	138,078,378	Zm00001d026084	IQ-domain 23	EW(0.6)	EW(-0.65)	.
MBS	10	138,131,658	Zm00001d026088	Outer cell layer2	EW(0.62)	.	.
MBS	10	138,131,894	Zm00001d026088	Outer cell layer2	EW(0.6)	EW(-0.65)	.
MBS	10	138,132,103	Zm00001d026088	Outer cell layer2	EW(0.6)	EW(-0.65)	.
MBS	10	138,132,566	Zm00001d026088	Outer cell layer2	EW(0.6)	EW(-0.65)	.
MBS	10	138,132,599	Zm00001d026088	Outer cell layer2	EW(0.6)	EW(-0.66)	.
MBS	10	138,132,898	Zm00001d026088	Outer cell layer2	EW(0.6)	EW(-0.65)	.
MBS	10	138,137,201	Zm00001d026088	Outer cell layer2	EW(0.61)	.	.
MBS	10	138,137,451	Zm00001d026088	Outer cell layer2	EW(0.6)	EW(-0.66)	.
MBS	10	138,137,960	Zm00001d026088	Outer cell layer2	EW(0.59)	EW(-0.69)	.
MBS	10	138,138,044	Zm00001d026088	Outer cell layer2	EW(0.6)	EW(-0.65)	.
MBS	10	138,138,046	Zm00001d026088	Outer cell layer2	EW(0.6)	EW(-0.65)	.
MBS	10	138,139,518	Zm00001d026089	Replication factor C subunit 2	EW(0.6)	EW(-0.65)	.
MBS	10	138,139,571	Zm00001d026089	Replication factor C subunit 2	EW(0.6)	EW(-0.65)	.
MBS	10	138,139,579	Zm00001d026089	Replication factor C subunit 2	EW(0.6)	EW(-0.67)	.
MBS	10	138,139,659	Zm00001d026089	Replication factor C subunit 2	EW(0.6)	EW(-0.66)	.
MBS	10	138,140,091	Zm00001d026089	Replication factor C subunit 2	EW(0.6)	EW(-0.65)	.
MBS	10	138,140,299	Zm00001d026089	Replication factor C subunit 2	EW(0.58)	EW(-0.65)	.
MBS	10	138,144,078	Zm00001d026089	Replication factor C subunit 2	EW(0.62)	.	.
MBS	10	138,144,542	Zm00001d026089	Replication factor C subunit 2	EW(0.6)	EW(-0.65)	.
MBS	10	138,144,756	Zm00001d026089	Replication factor C subunit 2	EW(0.6)	EW(-0.65)	.
MBS	10	138,144,795	Zm00001d026089	Replication factor C subunit 2	EW(0.6)	EW(-0.65)	.
MBS	10	138,144,976	Zm00001d026089	Replication factor C subunit 2	EW(0.59)	EW(-0.65)	.
MBS	10	138,160,754	Zm00001d026091	E3 ubiquitin-protein ligase	EW(0.6)	EW(-0.65)	.
MBS	10	138,161,139	Zm00001d026091	E3 ubiquitin-protein ligase	EW(0.6)	EW(-0.65)	.
MBS	10	138,161,310	Zm00001d026091	E3 ubiquitin-protein ligase	EW(0.6)	EW(-0.66)	.
MBS	10	138,162,346	Zm00001d026091	E3 ubiquitin-protein ligase	EW(0.6)	EW(-0.65)	.
MBS	10	138,163,421	Zm00001d026091	E3 ubiquitin-protein ligase	EW(0.6)	EW(-0.65)	.
MBS	10	138,163,611	Zm00001d026091	E3 ubiquitin-protein ligase	EW(0.6)	EW(-0.65)	.
MBS	10	138,164,662	Zm00001d026091	E3 ubiquitin-protein ligase	EW(0.6)	EW(-0.65)	.
MBS	10	138,164,821	Zm00001d026091	E3 ubiquitin-protein ligase	EW(0.59)	EW(-0.67)	.
MBS	10	138,164,834	Zm00001d026091	E3 ubiquitin-protein ligase	EW(0.6)	EW(-0.65)	.
MBS	10	138,304,922	Zm00001d026094	Heat stress transcription factor B-2b	EW(0.6)	EW(-0.65)	.
MBS	10	138,304,960	Zm00001d026094	Heat stress transcription factor B-2b	EW(0.6)	EW(-0.65)	.
MBS	10	138,305,007	Zm00001d026094	Heat stress transcription factor B-2b	EW(0.6)	EW(-0.65)	.
MBS	10	138,305,241	Zm00001d026094	Heat stress transcription factor B-2b	EW(0.6)	EW(-0.65)	.
MBS	10	138,305,316	Zm00001d026094	Heat stress transcription factor B-2b	EW(0.6)	EW(-0.65)	.

Table S8 Significant trait association (allele effect) in 2018, 2019 DSECG as well as DSEYM in F252. The first columns provide information on the chromosome, position, gene id and knwon description.

Inbred	CHROM	POS	Gene id	Gene function	2018	2019	DSEYM
F252	1	32,294,950	Zm00001d028367	Purple acid phosphatase 3	UE(0.02); LE(0.02)	UE(0.02); LE(0.04); BR(0.01); TKW(4.34)	.
F252	1	253,175,925	Zm00001d033181	fructokinase-like 2	EW(3.9)	EW(2.71)	.
F252	1	253,392,728	.	.	EW(3.91)	EW(2.71)	.
F252	1	254,195,407	Zm00001d033210	Chaperone protein dnaJ 3	EW(3.9)	EW(2.71)	.
F252	1	254,395,449	.	.	EW(3.93)	EW(2.73)	.
F252	1	254,402,515	Zm00001d033214	CSL zinc finger domain-containing protein	EW(3.96)	EW(2.74)	.
F252	1	254,528,657	Zm00001d033217	Serine/threonine-protein phosphatase BSL3	.	EW(2.66)	.
F252	1	254,539,899	Zm00001d033217	Serine/threonine-protein phosphatase BSL3	EW(3.9)	EW(2.71)	.
F252	1	254,991,675	Zm00001d033221	Ubiquitin carboxyl-terminal hydrolase family protein	EW(3.97)	EW(2.74)	.
F252	1	255,022,503	Zm00001d033222	viviparous14	EW(3.9)	EW(2.71)	.
F252	1	255,219,970	Zm00001d033228	Ornithine aminotransferase mitochondrial	EW(3.87)	EW(2.69)	.
F252	1	255,234,707	.	.	.	EW(2.64)	.
F252	1	255,268,529	Zm00001d033231	Expansin-B4	EW(3.9)	EW(2.71)	.
F252	1	255,514,992	Zm00001d033240	BTB/POZ domain-containing protein	EW(3.88)	EW(2.7)	.
F252	1	255,568,976	Zm00001d033241	Cationic amino acid transporter 1	EW(3.88)	EW(2.69)	.
F252	1	255,749,053	Zm00001d033244	U3 snoRNP-associated protein-like EMB2271	EW(3.88)	EW(2.7)	.
F252	1	255,755,722	Zm00001d033244	U3 snoRNP-associated protein-like EMB2271	EW(3.99)	EW(2.75)	.
F252	1	257,010,785	Zm00001d033273	Organic cation/carnitine transporter 7	EW(4.36)	EW(2.87)	.
F252	1	257,134,179	Zm00001d033275	Protein kinase superfamily protein	EW(4.3)	EW(2.82)	.
F252	1	269,324,947	Zm00001d033633	Haloacid dehalogenase-like hydrolase (HAD) superfamily protein	EW(4.25)	EW(2.78)	.
F252	1	269,325,241	Zm00001d033633	Haloacid dehalogenase-like hydrolase (HAD) superfamily protein	EW(4.28)	EW(2.8)	.
F252	1	269,331,941	Zm00001d033635	Cytidine/deoxycytidylate deaminase family protein	EW(4.28)	EW(2.8)	.
F252	1	269,333,808	Zm00001d033635	Cytidine/deoxycytidylate deaminase family protein	EW(4.12)	EW(2.71)	.
F252	1	269,356,692	Zm00001d033641	.	EW(4.2)	EW(2.75)	.
F252	1	269,358,139	Zm00001d033641	.	EW(4.28)	EW(2.8)	.
F252	1	269,400,179	.	.	EW(4.26)	EW(2.79)	.
F252	1	269,681,916	Zm00001d033651	Beta-glucosidase	EW(4.12)	EW(2.71)	.
F252	1	269,775,685	Zm00001d033655	Mitogen-activated protein kinase kinase kinase 1	EW(4.3)	EW(2.82)	.
F252	1	269,982,649	Zm00001d033664	Gtk16 protein	EW(4.13)	EW(2.71)	.
F252	1	275,916,458	.	.	.	EW(2.59)	.
F252	1	276,052,258	Zm00001d033858	.	.	EW(2.59)	.
F252	3	141,724,144	.	.	FT(-1.18); HT(-3.51); BR(-0.04); LL(-0.47)	FT(-1.27); HT(-2.13); #L(-0.28); BR(-0.07); LL(-0.88)	FT(-1.57)
F252	3	174,863,727	Zm00001d042639	Mitotic spindle checkpoint protein MAD1	EW(4.41)	EW(2.94)	.
F252	3	175,045,836	Zm00001d042641	RNA-binding (RRM/RBD/RNP motifs) family protein	EW(4.02)	EW(2.72)	.
F252	3	175,814,858	Zm00001d042661	Serine hydroxymethyl-transferase 7	EW(4.49)	EW(2.99)	.
F252	3	175,820,497	Zm00001d042662	Putative 1-phosphatidylinositol-3-phosphate 5-kinase FAB1D	EW(4.38)	EW(2.93)	.
F252	3	175,965,273	Zm00001d042665	Transcription repressor MYB6	EW(4.43)	EW(2.92)	.
F252	3	176,037,840	Zm00001d042667	P-loop containing nucleoside triphosphate hydrolases superfamily protein	EW(4.38)	EW(2.93)	.

F252	3	176,205,080	Zm00001d042670	Erythroid differentiation-related factor 1-like protein; protein	EW(4.48)	EW(2.98)	.
F252	3	176,925,873	Zm00001d042686	Protein SENSITIVE TO PROTON RHIZOTOXICITY 1	EW(4.38)	EW(2.93)	.
F252	3	176,926,475	Zm00001d042686	Protein SENSITIVE TO PROTON RHIZOTOXICITY 1	EW(4.38)	EW(2.93)	.
F252	3	176,927,099	Zm00001d042686	Protein SENSITIVE TO PROTON RHIZOTOXICITY 1	EW(4.41)	EW(2.95)	.
F252	3	177,037,403	Zm00001d042690	Embryogenesis-associated protein EMB8	EW(4.52)	EW(3.01)	.
F252	3	177,704,615	Zm00001d042708	Tudor/PWWP/MBT superfamily protein	EW(4.61)	EW(3.06)	.
F252	3	177,927,310	Zm00001d042712	.	EW(4.41)	EW(2.95)	.
F252	3	178,062,988	Zm00001d042713	DNA polymerase alpha catalytic subunit	EW(4.43)	EW(2.96)	.
F252	3	178,126,657	Zm00001d042719	Integral membrane Yip1 family protein	EW(4.39)	EW(2.93)	.
F252	3	178,129,308	Zm00001d042720	Sterol 3-beta-glucosyltransferase	EW(4.52)	EW(3.01)	.
F252	3	185,000,335	Zm00001d042962	Ypt/Rab-GAP domain of gyp1p superfamily protein	FT(3.15)	FT(3.57)	.
F252	3	185,081,768	Zm00001d042965	Nucleic acid binding protein	FT(3.11)	FT(3.55)	.
F252	3	186,923,424	.	.	FT(3.1)	FT(3.52)	.
F252	3	187,342,903	Zm00001d043047	Expansin-A2	FT(3.12)	FT(3.55)	.
F252	3	187,652,529	Zm00001d043056	Protein kinase superfamily protein	FT(3.11)	FT(3.54)	.
F252	3	192,392,891	Zm00001d043225	Pentatricopeptide repeat-containing protein mitochondrial	EW(4.18)	EW(2.65)	.
F252	3	192,496,223	Zm00001d043228	Cardiolipin synthetase	HT(3.41); LL(0.46); TKW(-0.85); EW(-4.71)	HT(2.12); LL(0.9); EW(-3.08)	.
F252	3	192,551,402	Zm00001d043229	RNA-binding KH domain-containing protein	EW(4.35)	EW(2.75)	.
F252	3	226,715,134	Zm00001d044387	Transmembrane amino acid transporter family protein	TKW(-0.98)	HT(2.01)	.
F252	3	226,839,217	Zm00001d044390	Aspartyl protease family protein 2	TKW(-0.95)	HT(2.06)	.
F252	3	226,847,075	Zm00001d044391	Mitochondrial ATP synthase subunit G protein	#L(0.59); BR(0.07); LL(0.58)	#L(0.55); UE(0.65); BR(0.08); LL(1.19)	.
F252	3	227,051,869	Zm00001d044394	.	TKW(-1.05)	HT(2.04)	.
F252	5	172,814,511	Zm00001d016694	Poly [ADP-ribose] polymerase 3	EW(3.86)	EW(2.73)	.
F252	5	172,838,675	.	.	.	EW(2.67)	.
F252	5	172,839,491	Zm00001d016697	Germin-like protein subfamily 3 member 2	.	LL(0.91); EW(-2.63)	.
F252	5	195,387,533	Zm00001d017419	Protein kinase APK1A	HT(2.17); LL(0.66)	#L(-0.15); LL(0.91)	.
F252	5	195,604,770	.	.	HT(2.15); LL(0.64)	#L(-0.16); LL(0.89)	.
F252	5	196,425,957	Zm00001d017456	ypt homolog4	LL(-0.42); EW(3.98)	EW(2.67)	.
F252	6	25,572,514	Zm00001d035439	knotted related homeobox5	FT(-3.33); #L(-0.57); UE(-0.64); LE(-0.63); LL(-0.6)	FT(-3.38); UE(-0.63); LE(-0.74); LL(-1.01)	FT(-3.39)
F252	6	130,321,359	Zm00001d037579	binding	FT(0.05); HT(3.08); #L(-0.02); UE(0.05); BR(-0.08); LL(0.64); TKW(5.66)	FT(0.43); HT(2.34); #L(-0.02); UE(0.05); LE(0.1); BR(0.02); LL(1.02); TKW(8.26); EW(0.55)	FT(0.8)
F252	6	159,381,657	Zm00001d038533	centromeric histone H3	EW(3.95)	EW(2.65)	.
F252	6	159,541,021	Zm00001d038536	Endoplasmic reticulum vesicle transporter protein	EW(3.89)	EW(2.61)	.
F252	6	159,593,960	Zm00001d038538	Ulp1 protease family C-terminal catalytic domain containing protein expressed	EW(3.96)	EW(2.65)	.
F252	6	159,606,204	Zm00001d038541	Histone-lysine N-methyltransferase H3 lysine-9 specific SUVH3	EW(3.96)	EW(2.65)	.
F252	6	160,254,897	.	.	EW(3.86)	.	.
F252	6	160,350,155	Zm00001d038576	Calcium-transporting ATPase 4 plasma membrane-type	EW(3.87)	.	.
F252	6	161,895,996	Zm00001d038652	Thioredoxin H4	HT(-5.8)	HT(-4.05)	.

F252	8	137,530,668	.	.	UE(0.02); LE(0.02)	UE(0.01); LE(0.04); BR(0.01); TKW(4.21)	.
F252	8	145,382,041	Zm00001d011272	CASC3/Barentsz eIF4AIII binding	FT(3.16)	.	.
F252	8	145,509,644	.	.	FT(3.12)	.	.
F252	8	146,110,247	Zm00001d011298	C3HC zinc finger-like	FT(3.13)	.	.
F252	8	146,174,061	Zm00001d011301	Starch branching enzyme III	FT(3.11)	.	.
F252	8	146,420,014	Zm00001d011312	Putative leucine-rich repeat receptor-like protein kinase family protein	FT(3.11)	.	.
F252	8	146,490,142	Zm00001d011314	ATP synthase subunit epsilon 2C mitochondrial	FT(3.17)	.	.
F252	8	146,622,935	Zm00001d011321	V-type proton ATPase subunit c″2	FT(3.16)	.	.
F252	8	146,961,161	Zm00001d011330	Cytochrome c oxidase subunit 5b-2 mitochondrial	FT(3.15)	.	.
F252	8	147,890,778	Zm00001d011353	Vacuolar protein sorting-associated protein 32 homolog 1	FT(3.14)	.	.
F252	8	148,435,746	Zm00001d011360	CENPCB protein	FT(3.12)	.	.
F252	8	148,482,692	Zm00001d011362	PsbP domain-containing protein 5 chloroplastic	FT(3.14)	.	.
F252	8	148,916,150	Zm00001d011373	Extra-large G-protein-like; protein	FT(3.17)	FT(3.52)	.
F252	8	149,391,857	Zm00001d011392	Calcium-dependent protein kinase 2C isoform 2 3B Putative calcium-dependent protein kinase family protein isoform 1 3B Putative calcium-dependent protein kinase family protein isoform 2	FT(3.14)	.	.
F252	8	149,475,231	Zm00001d011396	GTPase activating protein 3B Putative calcium-dependent lipid-binding (CaLB domain) family protein	FT(3.12)	.	.
F252	8	149,502,716	Zm00001d011398	.	FT(3.11)	.	.
F252	8	155,019,240	Zm00001d011585	.	EW(4.03)	EW(2.78)	.
F252	9	8,481,835	Zm00001d044970	Probable tyrosine-protein phosphatase	HT(3.27); LL(0.43); EW(-4.29)	HT(2.11); LL(0.84); EW(-2.83)	.
F252	9	8,652,853	Zm00001d044971	Putative transcription elongation factor SPT5 homolog 1	EW(4.28)	EW(2.8)	.
F252	9	9,339,393	Zm00001d044985	Pantothenate kinase family protein	FT(3.23); #L(0.56); UE(0.65); LE(0.65)	FT(3.55); #L(0.5); UE(0.64)	.
F252	9	9,423,024	Zm00001d044988	.	EW(4.06)	EW(2.61)	.
F252	9	124,898,248	Zm00001d047269	Protein EARLY FLOWERING 4	FT(3.11)	.	.
F252	10	128,650,419	Zm00001d025762	.	HT(2.13); UE(0.02); LE(0.02)	LE(0.04); TKW(4.43)	.
F252	10	135,967,055	Zm00001d026012	OSJNBa0088A01.13 protein; protein	FT(3.1)	.	.